

THE RESONANT NATURE OF TIDAL STIRRING OF DISKY DWARF GALAXIES ORBITING THE MILKY WAY

EWA L. LOKAS¹, MARCIN SEMCZUK^{1,2}, GRZEGORZ GAJDA¹ AND ELENA D'ONGHIA^{3,4}

Accepted for publication in ApJ on August 4, 2015

ABSTRACT

Using *N*-body simulations we study the tidal evolution of initially disk-like dwarf galaxies orbiting a Milky Way-like host, a process known to lead to the formation of dwarf spheroidal galaxies. We focus on the effect of the orientation of the dwarf galaxy disk's angular momentum with respect to the orbital one and find very strong dependence of the evolution on this parameter. We consider four different orientations: the exactly prograde, the exactly retrograde and two intermediate ones. Tidal evolution is strongest for the exactly prograde and weakest for the exactly retrograde orbit. In the prograde case the stellar component forms a strong bar and remains prolate until the end of the simulation, while its rotation is very quickly replaced by random motions of the stars. In the retrograde case the dwarf remains oblate, does not form a bar and loses rotation very slowly. In the two cases of intermediate orientation of the disk, the evolution is between the two extremes, suggesting a monotonic dependence on the inclination. We interpret the results in terms of the resonance between the angular velocity of the stars in the dwarf and its orbital motion by comparing the measurements from simulations to semi-analytic predictions. We conclude that resonant effects are the most important mechanism underlying the tidal evolution of disk-like dwarf galaxies.

Subject headings: galaxies: dwarf — galaxies: fundamental parameters — galaxies: kinematics and dynamics — galaxies: structure — Local Group

1. INTRODUCTION

The formation of dwarf spheroidal (dSph) galaxies in the Local Group remains an open question but one of the most promising scenarios for their origin is via the tidal interaction of their disk-like progenitors with more massive hosts like the Milky Way. The scenario, proposed by Mayer et al. (2001) explains the morphology-density relation observed among the dwarfs of the Local Group and accounts for the non-sphericity of the dSph objects.

The efficiency of the mechanism and its observational predictions have been investigated in detail by Klimmtowski et al. (2009), Kazantzidis et al. (2011) and Lokas et al. (2011, 2012). These studies explored the dependence of the process on a large number of orbital and structural parameters of the dwarf. The general picture that emerged from these studies is that a disk-like dwarf progenitor, once accreted by a massive host, undergoes strong tidal stirring and mass stripping if the orbit is tight enough.

Typically, at the first pericenter passage, the disk transforms into a tidally induced bar (for a detailed description of the properties of such a bar see Lokas et al. 2014a). The bar becomes thicker and shorter in time leading in the end to the formation of a spheroidal stellar component. The morphological transformation is accompanied by strong changes in the kinematics as quantified by the amount of ordered to random motion. The latter starts to dominate at some point and at the end the

galaxy is pressure supported.

Among the parameters expected to have a strong impact on the evolution is the inclination between the angular momentum of the dwarf galaxy disk and its orbital angular momentum. However, in the studies mentioned above only a narrow range of inclinations was studied in detail, namely those with values $i = 0^\circ$, 45° and 90° . Because of this range, and the way the properties of the dwarf were measured, no clear evidence for the dependence on this parameter was found. On the other hand, the difference between the prograde and retrograde galaxy encounters has been recognized for a long time and known to lead to very different outcomes (e.g. Holmberg 1941; Hénon 1970; Kozlov et al. 1972; Toomre & Toomre 1972; Keenan & Innanen 1975). The issue has been recently addressed again by D'Onghia et al. (2009, 2010) using an improved version of the impulse approximation applied to rotating systems. Although this approximation is not directly applicable to our simulations, we attempt a comparison between these results and the numerical ones.

In this paper we aim at clarifying the issue of the dependence of the results of tidal encounters between dwarfs and their hosts on the inclination of the dwarf's disk. For this purpose we performed four simulations of tidal evolution of a dwarf galaxy orbiting a Milky Way-like host with disk inclinations $i = 0^\circ$, 90° , 180° and 270° . The angles of 0° and 180° correspond to exactly prograde and exactly retrograde orientations of the dwarf's disk. We also measured the properties of the dwarf galaxy in a different way that enables clear comparisons between different runs. Preliminary results of this study, using lower resolution simulations, were discussed in Lokas & Semczuk (2014).

The paper is organized as follows. In section 2 we

¹ Nicolaus Copernicus Astronomical Center, Bartycka 18, 00-716 Warsaw, Poland

² Warsaw University Observatory, Al. Ujazdowskie 4, 00-478 Warsaw, Poland

³ Department of Astronomy, University of Wisconsin-Madison, Madison, WI 53706, USA

⁴ Alfred P. Sloan Fellow

TABLE 1
INITIAL CONDITIONS FOR THE SIMULATIONS

Simulation	L_X	L_Y	L_Z	Inclination (deg)	Line color/type
I0	0.0	0.0	1.0	0	red/solid
I90	0.0	-1.0	0.0	90	blue/short-dashed
I180	0.0	0.0	-1.0	180	green/dotted
I270	0.0	1.0	0.0	270	cyan/long-dashed

present the simulations used in this study. In section 3 we discuss the properties of the dwarf galaxies as they evolve in time, focusing on their kinematics, morphology and density profiles. Section 4 compares the results of the simulations to the predictions of semi-analytic models. The conclusions follow in section 5.

2. THE SIMULATIONS

The simulations used in this study were similar to those described in detail in Lokas et al. (2014a). Here we therefore provide only a short summary. The initial conditions for the simulations consisted of N -body realizations of two galaxies: the Milky Way-like host and the dwarf galaxy, generated via procedures described in Widrow & Dubinski (2005) and Widrow et al. (2008). Both galaxies contained exponential disks embedded in NFW (Navarro et al. 1997) dark matter haloes, each made of 10^6 particles (4×10^6 total). We note that the results presented here differ only slightly (are less noisy) from those of lower resolution simulations in Lokas & Semczuk (2014) where a smaller number of particles was used (by a factor of five). We are therefore confident that our present resolution is sufficient to grasp all the essential features of the evolution.

The dwarf galaxy model had a dark halo of mass $M_h = 10^9 M_\odot$ and concentration $c = 20$. Its disk had a mass $M_d = 2 \times 10^7 M_\odot$, an exponential scale-length $R_d = 0.41$ kpc and thickness $z_d/R_d = 0.2$. The model is stable against formation of the bar in isolation for the time scales of interest here. The host galaxy was similar to the model MWb of Widrow & Dubinski (2005). It had a dark matter halo of mass $M_H = 7.7 \times 10^{11} M_\odot$ and concentration $c = 27$. The disk of the host had a mass $M_D = 3.4 \times 10^{10} M_\odot$, the scale-length $R_D = 2.82$ kpc and thickness $z_D = 0.44$ kpc. The disk was also stable against bar formation to avoid strong variations of the host potential in time. The disk of the Milky Way was coplanar with the orbit of the dwarf. Although this may seem contrary to observational constraints where most of satellite orbits are found to be polar (e.g. Pawlowski & Kroupa 2014), the choice was motivated by the necessity to avoid any additional variability which may be due to the passages through the plane of the Milky Way disk. However, we have performed an additional simulation to verify that for the orbits used here the evolution of the dwarf depends very weakly on the orientation of the orbit with respect to the Milky Way disk.

The dwarf galaxy was initially placed at an apocenter of a typical, eccentric orbit around the Milky Way with apo- to pericenter distance ratio of $r_{apo}/r_{peri} = 120/25$ kpc. The initial position was at the coordinates $(X, Y, Z) = (-120, 0, 0)$ kpc of the simulation box and

the velocity vector of the dwarf was toward the negative Y direction. We performed four simulations with different dwarf disk orientations with respect to the orbit: two coplanar with the orbit (prograde and retrograde) and two perpendicular to the orbit with angular momenta in the same and opposite direction to the dwarf's orbital velocity. The different initial conditions, in particular the components of the unit angular momentum vector, are listed in Table 1. We will refer to the simulations by names indicating the initial inclination of the disk, I0, I90, I180 and I270, where the inclination is measured as the rotation angle around the X axis of the simulation box.

The evolution of the system in each simulation was followed for 10 Gyr using the GADGET-2 N -body code (Springel et al. 2001; Springel 2005) with outputs saved every 0.05 Gyr. The adopted softening scales were $\epsilon_d = 0.02$ kpc and $\epsilon_h = 0.06$ kpc for the disk and halo of the dwarf while $\epsilon_D = 0.05$ kpc and $\epsilon_H = 2$ kpc for the disk and halo of the host, respectively.

3. EVOLUTION OF THE DWARFS

In this section we look at the inner properties of the dwarf galaxies as they are transformed by the tidal forces from the Milky Way. All measurements discussed below were made for stars (and dark matter particles) within the radius of 0.5 kpc from the center of the dwarf.

3.1. Mass content

We begin the analysis by measuring the mass inside this radius. Figure 1 compares the mass of stars (upper panel) and dark matter (lower panel) in the four simulations. As expected, the dark mass content decreases systematically, most significantly at pericenters that occur at $t = 1.2, 3.3, 5.5, 7.6, 9.7$ Gyr from the start of the simulation and there is no dependence on the inclination because the halos were spherical and isotropic in all cases.

On the other hand, for the stellar component (upper panel) there is a significant difference between dwarfs with varying initial inclination. However, the dependence may seem surprising because we expect the prograde disk to be more stripped, while the opposite is seen in the Figure: the stellar mass for the I0 simulation is even increased after the first pericenter passage, while it is decreased in the remaining cases. While the tidal stripping is indeed stronger in the outer parts, in the inner region we probe by this measurement, the stellar content increases as a result of the significant change in the structure of the stellar component due to the formation of a tidally induced bar.

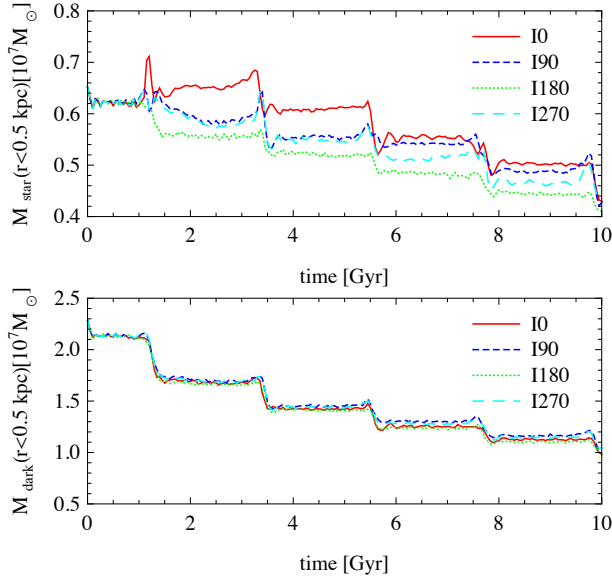


FIG. 1.— The evolution of the stellar (upper panel) and dark (lower panel) mass of the dwarf galaxy enclosed within the radius of 0.5 kpc. Different lines correspond to different initial inclination of the dwarf galaxy disk.

3.2. Kinematics

The main criteria usually applied in order to verify if a dwarf galaxy transformed from a disk object to a dSph are based on kinematics and shape of the stellar component. A dSph galaxy is supposed to be characterized by the dominance of random motions of the stars over the amount of rotation and its shape should be sufficiently close to spherical. In this and the following subsection we look in detail at the evolution of these quantities.

In order to measure these properties, for each simulation output we determine the directions of the principal axes of the stellar component from stars within the radius of 0.5 kpc using the inertia tensor and rotate these stars so that the new coordinate system is aligned with the principal axes (the x axis is along the longest, the y axis along the intermediate and the z axis along the shortest axis of the stellar component). We then introduce a standard spherical coordinate system such that ϕ measures the angle around the z axis and θ the angle from the z axis towards the xy plane.

The kinematic properties were estimated using these coordinates. In the top panel of Figure 2 we plot the rotation around the shortest axis $V = V_{\phi}$ as a function of time. We note that there is no other significant streaming motion along the other spherical coordinates or around the two other principal axes (see Łokas et al. 2014b for a brief discussion of this issue). Clearly, the rotation is decreasing most strongly for the exactly prograde inclination of the disk (I0), a significantly smaller decrease is seen for the perpendicular orientations (I90 and I270) and the effect is the weakest for the retrograde case (I180). Note that the decrease of rotation is not steadily monotonic even in the exactly prograde case (I0). This is due to the tidal torques acting on the bar at pericenter passages that can speed up or slow down the bar depending on its particular orientation at this

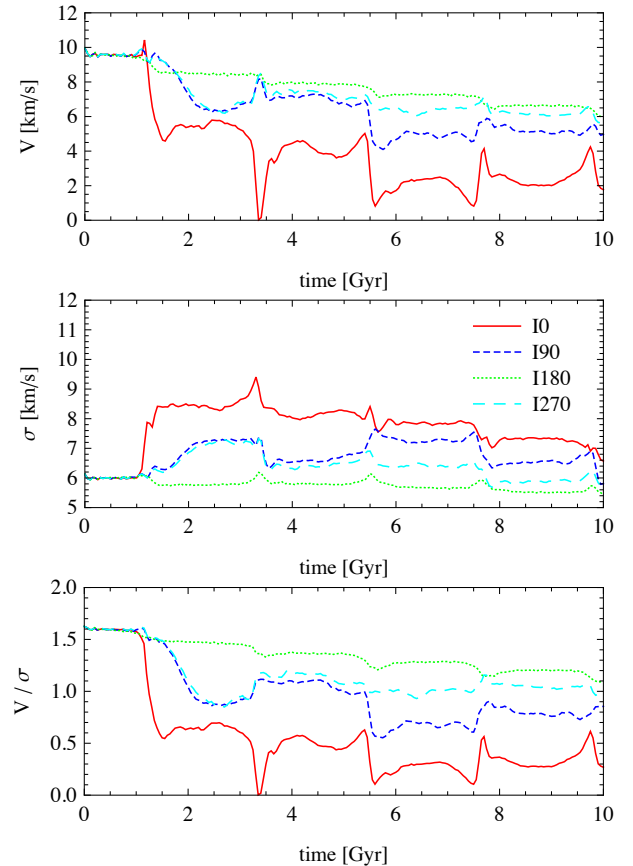


FIG. 2.— The evolution of the mean rotation velocity (upper panel), the velocity dispersion (middle panel) and the ratio of the two (lower panel) as a function of time.

moment (see Łokas et al. 2014a for details).

The behavior of the velocity dispersion is exactly the opposite. In the middle panel of Figure 2 we show the 1D velocity dispersion calculated as $\sigma = [(\sigma_r^2 + \sigma_{\theta}^2 + \sigma_{\phi}^2)/3]^{1/2}$. The increase of σ at the first pericenter passage is strongest for the I0 case, intermediate for I90 and I270 and for I180 σ remains constant in time or even slightly decreases due to mass loss. The ratio V/σ shown in the lower panel of Figure 2 decreases for all simulations, but reaches a value significantly below unity only for the prograde case. For the three remaining cases a substantial amount of rotation is retained, although the hierarchy of lower V/σ for more prograde cases is preserved.

In Figure 3 we show the evolution of the different velocity dispersions σ_r (upper panel), σ_{θ} (second panel) and σ_{ϕ} (third panel) as a function of time. In all cases the increase of a given dispersion at the first pericenter passage and its level at later times is highest for the I0 case, intermediate for I90 and I270 and non-existent for I180. In addition, this increase is the most abrupt for the prograde dwarf, while for the intermediate inclinations I90 and I270 the increase occurs much more slowly in time and takes about half the orbital period between the first and second pericenter passage. Interestingly, significant increase is seen in all dispersions in spite of the fact that, due to the formation of the bar, one could expect the radial σ_r to increase much more significantly.

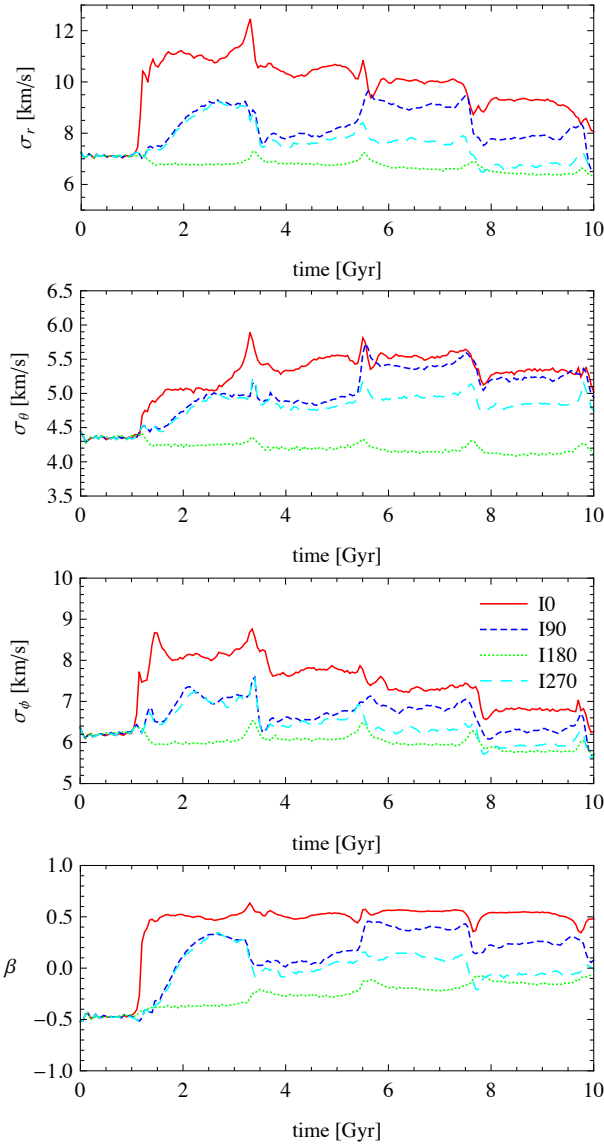


FIG. 3.— The evolution of the velocity dispersions of the stars in spherical coordinates σ_r (upper panel), σ_θ (second panel) and σ_ϕ (third panel). The lower panel shows the evolution of the anisotropy parameter β .

We end the analysis of the kinematics by plotting in the lower panel of Figure 3 the value of the anisotropy parameter $\beta = 1 - \sigma_t^2 / (2\sigma_r^2)$ where $\sigma_t^2 = \sigma_\theta^2 + \sigma_\phi^2 + V_\phi^2$ is the tangential second moment including rotation. A systematic dependence of this parameter on the inclination of the disk is also present: the stellar orbits are most radial for the I0 case with β almost constantly at the level of 0.5, corresponding to mildly radial orbits of the stars, characteristic of the bar. For the intermediate cases I90 and I270 the β values stay between 0 and 0.4, while for the retrograde case I180 β remains negative due to the dominant presence of rotation. Interestingly, at the end of the evolution all three non-prograde cases I90, I180 and I270 have almost isotropic orbits ($\beta = 0$) although they reach this special value via different evolutionary paths.

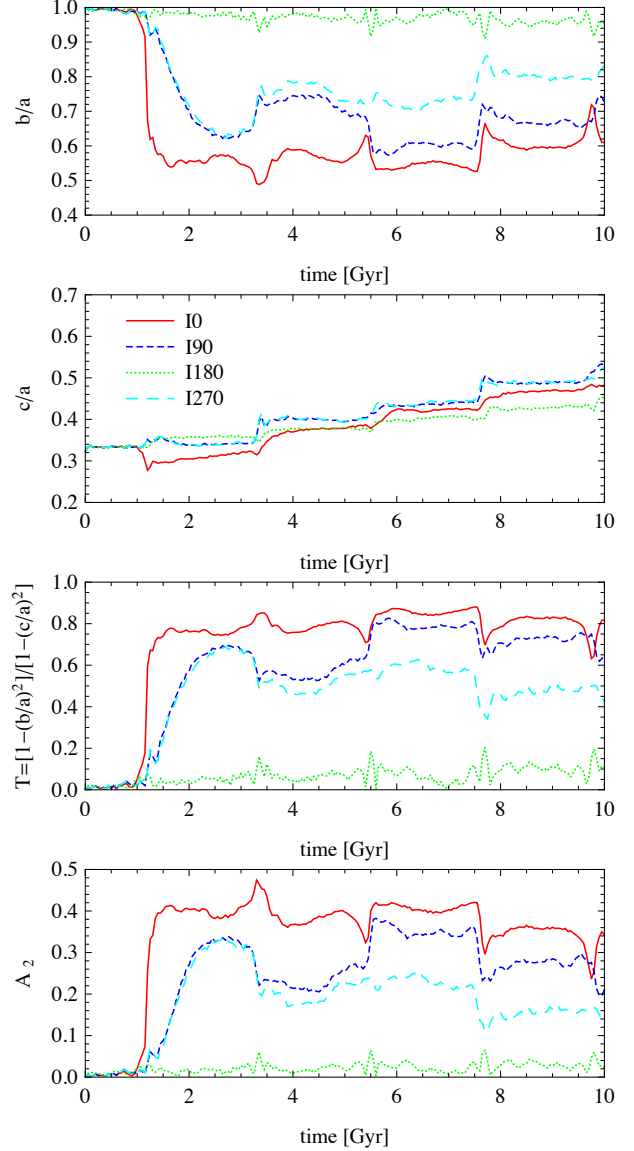


FIG. 4.— The evolution of the shape of the stellar component in time. The panels from top show the axis ratios b/a , c/a , the triaxiality parameter T and the bar mode A_2 .

3.3. Shapes

Figure 4 illustrates the evolution of the shape of the stellar component of the dwarfs in time. In the first and second panels from top we plot the axis ratios b/a (intermediate to longest) and c/a (shortest to longest). The thickening of the dwarf, as quantified by the increasing value of c/a is similar in all cases, although for the prograde case c/a decreases after the first pericenter due to the formation of the bar. Much more significant differences are seen in the evolution of b/a . This value decreases most strongly for the prograde I0 case signifying the prolate shape characteristic of the bar. The intermediate inclinations I90 and I270 lead to less prolate shapes, while I180 remains disk-like for the whole evolution, as indicated by b/a remaining constantly close to unity.

The shape can be also quantified in terms of the triaxiality parameter $T = [1 - (b/a)^2]/[1 - (c/a)^2]$ which is shown in the third panel of Figure 4. The values of

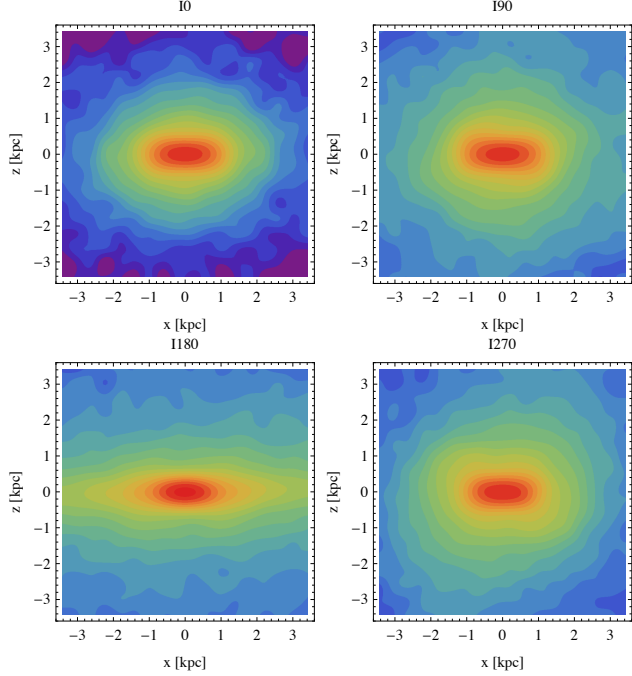


FIG. 5.— Surface density distributions of the stars in the dwarfs at the last apocenter ($t = 8.65$ Gyr) seen along the intermediate (y) axis of the stellar component. The surface density measurements were normalized to the maximum value $\Sigma_{\max} = 4.8 \times 10^5$ stars kpc^{-2} occurring for I180. Contours are equally spaced in $\log \Sigma$ with $\Delta \log \Sigma = 0.05$.

the parameter $T > 2/3$ at all times confirm the prolate shape due to the bar in the case of I0. For the intermediate cases I90 and I270 we get $1/3 < T < 2/3$ indicating a triaxial shape. For the retrograde case I180 the parameter remains low, $T < 0.2$, at all times as is characteristic of a disk.

The presence of a bar is usually detected by measuring the bar mode A_2 of the Fourier decomposition of the stars projected along the shortest axis of the stellar distribution (see a more detailed discussion in Łokas et al. 2014a). Usually, $A_2 > 0.3$ is considered as high enough to be interpreted as a bar. As we can see in the lower panel of Figure 4 this is always the case for simulation I0 after the first pericenter passage and also for some significant periods of time for the intermediate cases I90 and I270, which means that the bar also forms there, but it is much weaker. The exactly retrograde disk does not form a bar as its $A_2 < 0.06$ at all times. Slight temporary increases of this value are due to stretching of the dwarf at the pericenters.

These measurements are confirmed by the maps of the surface density distribution of the stars in the four dwarfs plotted in Figure 5. The distributions are shown in projection along the intermediate axis of the stellar component so in their most non-spherical appearance. The snapshots were selected for the time $t = 8.65$ Gyr after the start of the simulations, corresponding to the last apocenter passage. In all cases, except for the retrograde one I180, the remnant of the bar formed after the first pericenter passage is still visible in the inner parts. In addition, the distribution of the stars in the prograde case I0 is much less diffuse in the outer parts of the maps. In spite of the fact that this dwarf evolves most strongly,

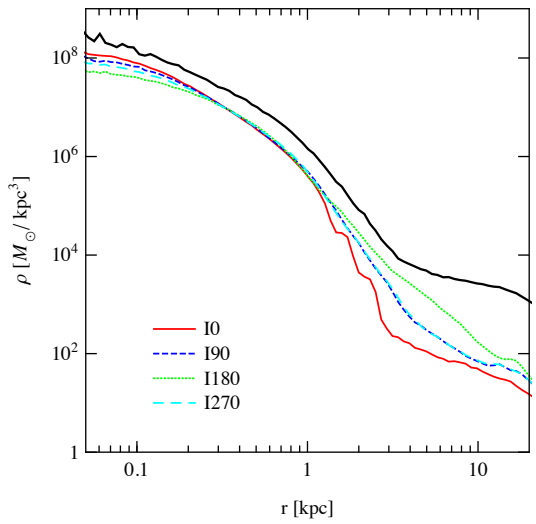


FIG. 6.— Comparison of stellar density profiles of the dwarfs at the fourth apocenter (6.6 Gyr after the start of the simulations, colored lines). For completeness we also show the dark matter profile (black line) which is similar for all simulations.

its neighborhood is not uniformly filled with stripped debris because the lost stars form well-defined, narrow tidal streams.

3.4. Density profiles

The dependence of the properties of the dwarfs on the initial inclination of the disk also manifests itself in the evolved density profiles. In Figure 6 we show examples of the stellar density profiles (different colors) and the dark matter density profile (black line) for different simulations considered here, measured at the fourth apocenter. The transition from the bound component to the tidal tails is visible as the break in the slope of the density profiles. This transition is however only well defined for the exactly prograde case I0 (and the dark matter profile). In this case the transition from the steeper to the shallower profile (where the slope is around r^{-4}) occurs at around 3 kpc. For other simulations no such clear break radius is seen.

As discussed in Łokas et al. (2013) using similar (but only mildly prograde) simulation setups, the break radii can be interpreted as the tidal radii. In this case, the dependence on the orbit of the star within the satellite is expected (Keenan & Innanen 1975; Read et al. 2006) and we will attempt a detailed comparison in a follow-up paper. Since the stellar density profiles of our simulated dwarfs do not show clear signatures of the break radius (except for the exactly prograde case) here we propose a comparison in terms of density. The stellar profiles shown in Figure 6 demonstrate clear hierarchy: at the outer radii (larger than 1 kpc) the stellar density profile of I180 (green line) is above all the other profiles, the one of I0 (red lines) is the lowest, and the ones of I90 and I270 fall exactly on top of each other and between the other two. This means that we can quantify the amount of tidal stripping in these different cases by measuring the density of the stars, rather than the break radius.

To do so, we calculated the mean density of stars in the shells of radii $2 \text{ kpc} < r < 4 \text{ kpc}$ as a function of time for different simulations. The results are shown in the upper

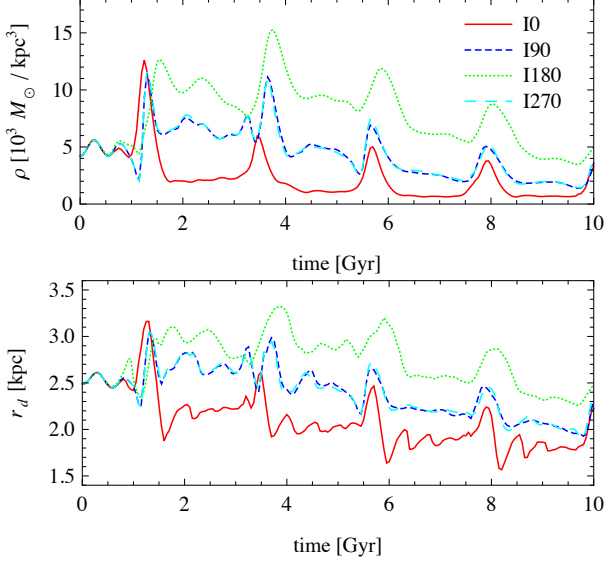


FIG. 7.— Upper panel: the density of stars in the shell of radii $2 \text{ kpc} < r < 4 \text{ kpc}$ as a function of time. Lower panel: the radius at which the density of stars drops below $10^4 M_\odot/\text{kpc}^3$ as a function of time.

panel of Figure 7. In the lower panel we plot the radius r_d at which the density of stars drops below $10^4 M_\odot/\text{kpc}^3$ as a function of time. In both plots there is a clear systematic difference between the measurements for different initial disk orientations: the stars are stripped more effectively on prograde orbits as demonstrated by the lower outer densities and smaller radii where the density drops to a fixed value. Although the values for the measurements were chosen in an arbitrary way, we expect the results to be similar if these parameters are slightly modified. They clearly confirm that the amount of tidal stripping depends very strongly on the initial inclination of the dwarf’s disk.

4. COMPARISON WITH SEMI-ANALYTIC PREDICTIONS

To describe the encounter between a disk galaxy and the Milky Way we use the impulse approximation as discussed in Binney & Tremaine (1987) and D’Onghia et al. (2010). According to this approximation the k th component of the acceleration of each dwarf’s star with respect to the center of mass is given by

$$\dot{v}_k = - \sum_j \frac{\partial^2 \psi}{\partial x_k \partial x_j} \Big|_{\mathbf{x}=0} x_j, \quad (1)$$

where ψ is the Milky Way’s (i.e. perturber’s) potential and x_i are Cartesian coordinates. We integrate equation (1) over a finite time period to obtain velocity increments that can be compared with increments measured from simulations

$$\Delta v_k = \int_0^{\Delta t} \dot{v}_k \, dt. \quad (2)$$

We work in a frame centered on the center of the dwarf’s mass, the dwarf’s disk lies in xy plane and position of the Milky Way at the pericenter is $(b_x, 0, b_z)$. In this frame the trajectory of each star originating from

the dwarf is

$$\mathbf{x} = [r \cos(\Omega t + \phi_0), r \sin(\Omega t + \phi_0), 0], \quad (3)$$

where r is the radius, Ω is the angular velocity and ϕ_0 is the initial azimuthal angle of the star. The trajectory of Milky Way is given by

$$\mathbf{X} = \mathbf{V}t + \mathbf{X}_0, \quad (4)$$

where \mathbf{V} and \mathbf{X}_0 are constant vectors, fitted to mimic the perturber’s trajectory from simulations as a straight line during a given time period. Note that \mathbf{V} and \mathbf{X}_0 are different for each of our simulations as they depend on the inclination i . This dependence can be found by rotating the trajectory for the prograde case with matrix \hat{A} defined by Euler angles, in order to obtain trajectories in other cases. One of the Euler angles is the inclination i and other two depend on the perturber’s orbit.

To approximate the gravitational potential of the Milky Way we sum the potential from its stars and the dark matter halo. The first part is represented as a point-mass potential, while the second is given by the NFW profile

$$\psi = - \frac{GM_D}{|\mathbf{x} - \mathbf{X}|} - g \frac{GM_H \ln(1 + c|\mathbf{x} - \mathbf{X}|/r_v)}{|\mathbf{x} - \mathbf{X}|}, \quad (5)$$

where M_D is the mass of the Milky Way disk, M_H is the virial mass of its halo, r_v is the virial radius, c is the concentration parameter and $g = [\ln(1 + c) - c/(1 + c)]^{-1}$ (see Lokas & Mamon 2001). Substituting equations (1), (3), (4) and (5) into (2) we obtain formulae which can be numerically integrated to get velocity increments.

In order to calculate the velocity increments described above we estimate the angular velocity in the dwarf as $\Omega = |\mathbf{v}|/r$. We calculate integrals of equation (2) over a small period of time, so that the assumptions concerning the trajectories are valid. In our simulations the outputs were saved every 0.05 Gyr and we choose to integrate over this time to compare our predictions with velocity increments occurring in the simulations when the tidal force is the strongest, i.e. between the output preceding the first pericenter and the one as close as possible to this pericenter. We check how the distribution of increments changes with the distance from the center of the dwarf. The results for all simulations are summarized in Figure 8.

The red points in Figure 8 represent the values predicted by the impulse approximation, while the blue points correspond to the values measured from the simulations. At radii smaller than 2 kpc the semi-analytical predictions do not reproduce the distribution of velocity increments because at these radii the velocity changes are dominated by the gravitational potential of the dwarf which was not included in the predictions. However, for radii greater than 2 kpc the agreement between the full simulations and semi-analytic predictions for this short time period is very good. In particular, in the upper left panel of Figure 8 for simulation I0 we find two very well-defined branches corresponding to stars on different sides of the dwarf. Branches from simulations are not exactly symmetric with respect to zero while the branches from theoretical predictions are. The difference is due to the fact that the analytic predictions only take into account the lowest order terms.

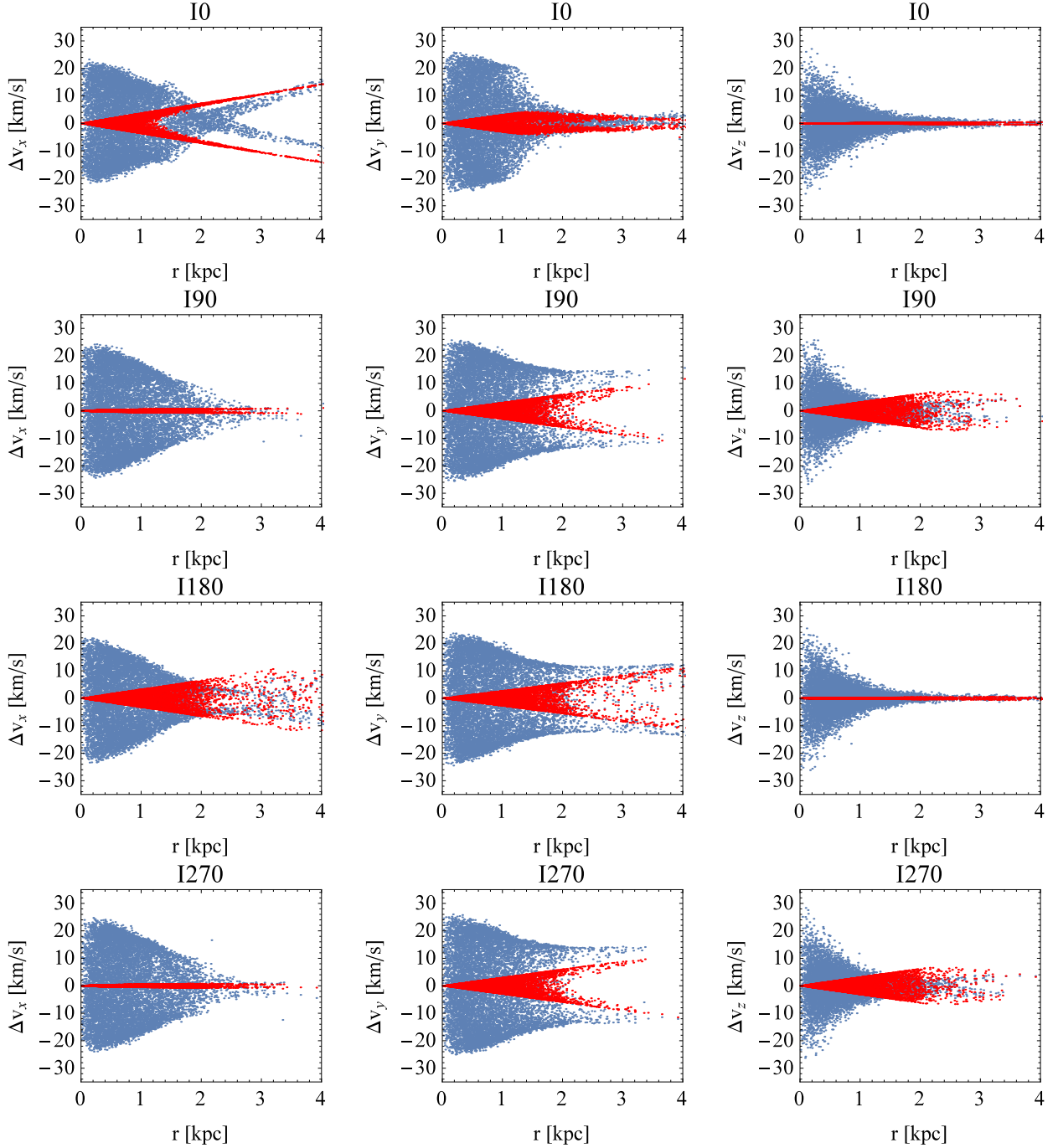


FIG. 8.— The components of velocity increments along the x , y and z axis for simulations with different initial inclination of the dwarf’s disk. The blue dots indicate the values measured for a subsample of stars in the simulation. Red dots show the corresponding semi-analytic predictions.

For simulations I270 the increments are almost identical as for I90, as expected due to symmetry of the two configurations with respect to the orbital plane. In some of the panels in Figure 8 the velocity increments for radii larger than 2 kpc are approximately zero. However, the negligible values are consistently obtained both from the simulations and the semi-analytic calculations.

We further illustrate these results in Figure 9 where we plot the surface density maps of the stellar component and the velocity vectors for a random sample of a hundred stars at radii larger than 2 kpc. The plots show the

dwarfs at the first pericenter passage, i.e. after they have been affected by a tidal impulse from the Milky Way for the first time. The coordinate system is as defined above, with xy coordinates in the plane of the dwarf’s disk.

The comparison of the upper left panel of Figure 9, corresponding to simulation I0, to the other three confirms that for the prograde encounter the effect of the tidal force in the strongest: the dwarf galaxy disk is already strongly distorted toward a bar-like shape and two tidal arms are formed. There are significant increments of velocity along the x axis. Small increments of veloc-

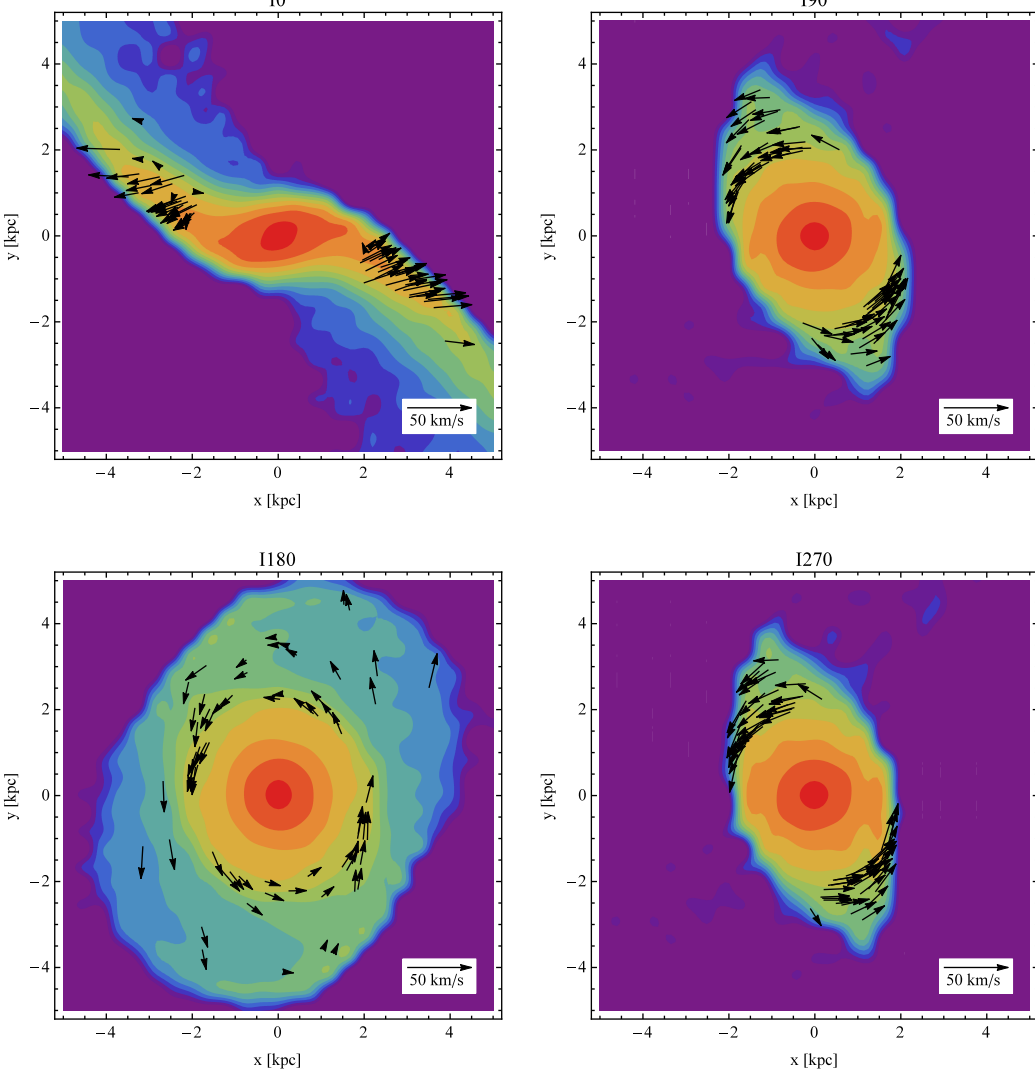


FIG. 9.— Surface density distributions of the stars in the dwarfs at the first pericenter ($t = 1.15$ Gyr) in projection onto the initial disk plane. Arrows indicate the velocities of the randomly selected subsample of 100 stars outside the radius of 2 kpc.

ties are also visible along the y axis in the right panels of Figure 9 corresponding to simulations I90 and I270. The effect of the tidal force is weakest for the retrograde case (lower left panel of Figure 9) where the dwarf's initial disk is affected very little.

As discussed by D'Onghia et al. (2010) strongest tidal interactions occur when the intrinsic angular velocities of stars in the dwarf's disk are comparable to the angular velocity of the satellite on its orbit. This condition can be written as

$$\Omega_{\text{disk}} \simeq \Omega_{\text{orb}} \quad (6)$$

and we can define the resonance parameter

$$\alpha = \frac{|\Omega|}{\Omega_{\text{orb}}}, \quad (7)$$

that should be of the order of unity for the strongest, resonant response.

To demonstrate the resonant nature of the tidal effects in our simulations we measured $\alpha(r)$ for each simulation output and found radii from the center of the dwarf at

which $\alpha = 1$. The time dependence of this radius for simulation I0 is shown in Figure 10. We can see that the variability of this radius reflects the varying orbital velocity Ω_{orb} of the dwarf resulting in rather large values at apocenters and much smaller ones at pericenters. The slow variation over time scales much larger than the orbital period is caused by the mass loss and decreasing Ω . Whenever the dwarf reaches the pericenter of its orbit around the Milky Way, this characteristic radius drops below 2 kpc, and even down to 1 kpc at the later pericenters. Note that these radii are of the order of 2–3 half-light radii of the stellar component which means that a significant fraction of stars is affected. Comparing with Figure 8 showing the velocities at the first pericenter we confirm that this radius (equal to 1.7 kpc at this time) is exactly where the tidal effects start to prevail over the dwarf's potential.

5. CONCLUSIONS

In this work we extended previous studies of the efficiency of the tidal stirring mechanism to include the de-

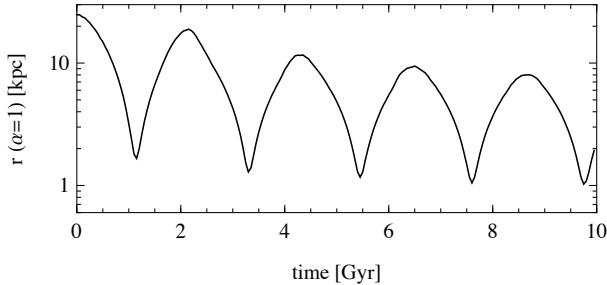


FIG. 10.— The evolution of the radius at which the resonance parameter $\alpha = 1$ in time. Only results for simulation I0 are shown because the measurements yield similar values for the remaining simulations.

pendence on the initial inclination of the dwarf galaxy disk with respect to its orbit around the Milky Way. Our simulation setups involved a dwarf galaxy placed on a typical, eccentric orbit around a Milky Way-like host and its evolution was followed for 10 Gyr. We considered four configurations, an exactly prograde, an exactly retrograde and two intermediate orientations of the disk. We found the efficiency of tidal stirring to be very strongly dependent on this inclination.

The effect of the tidal interaction turns out to be the strongest for the exactly prograde orientation of the dwarf's disk (I0). In this case the disk transforms into a strong bar ($A_2 = 0.4$) at the first pericenter passage and a remnant bar is retained until the end of the evolution. Although the bar becomes weaker with time, the shape of the stellar component is consistently prolate, but tending to a spherical toward the end of the evolution. This morphological transformation is mirrored in the kinematics by the gradual decrease of the dwarf's rotation velocity. Already at the first pericenter passage the rotation drops significantly and the velocity dispersion increases, mostly in the radial direction due to the formation of the bar. During subsequent pericenter passages the rotation is further decreased down to rather low values at the end of the simulation where $V/\sigma = 0.3$. Thus the streaming motions are almost completely replaced by random motions of the stars. Interestingly, the radial velocity dispersion dominates the whole time, which manifests itself in the anisotropy parameter close to $\beta = 0.5$ even at the end.

In the two cases of perpendicular orientations of the dwarf's disk with respect to the orbit (I90 and I270) the evolution is to some extent similar to the I0 case. In these configurations the bar also forms after the first pericenter passage, but more slowly (over a time scale of about 1 Gyr corresponding to half the orbital period) and is significantly weaker ($A_2 = 0.3$), also in the subsequent evolution. The overall shape of the stellar component can be characterized more as triaxial than decidedly prolate. The transition from the streaming to random motions of the stars also happens less efficiently with V/σ only slightly below unity at the final outputs. The anisotropy parameter is close to zero due to the contribution of the still significant rotation.

In the exactly retrograde case (I180) no strong evolution is present: the dwarf's stellar component does not form a bar and remains disky. The only signatures of tidal evolution in this case are the mass loss (similar as in other cases, mostly in dark matter), small decrease of the rotation velocity, slight evolution of the anisotropy parameter from negative toward isotropic and a non-negligible thickening of the disk. The difference between this and the other cases is also visible in the stellar density profiles which are less affected and do not show any clear transition from the bound component to the tidal tails.

We have interpreted these changes in the context of the resonant stripping mechanism recently discussed by D'Onghia et al. (2009, 2010). In particular, we calculated the velocity increments the dwarf's stars should experience at the first pericenter and compared them with the direct measurements from simulations. We find a very good agreement between the two, confirming the interpretation that the evolution we see in the full N -body treatment is indeed due to the orientation of the dwarf's disk. The resonant nature of the phenomenon is further confirmed by the behavior of the ratio between the angular velocity of the stars in the dwarf and the angular velocity of its orbital motion. This ratio turns out to be of the order of unity only near the pericenters and this is indeed when the tidal effects are the strongest.

The results presented here suggest that the most important mechanism underlying the tidal evolution of disky dwarfs orbiting a bigger galaxy is indeed of resonant nature. We propose to refer to the processes of morphological and dynamical evolution of the dwarfs we described as ‘resonant stirring’ in analogy to the ‘resonant stripping’ mechanism found by D'Onghia et al. (2009, 2010) to increase the mass loss in similar configurations. As discussed by D'Onghia et al. (2010), the resonance is broad, hence the name ‘quasi-resonant stirring’ would be more appropriate. In physical terms, this resonance can be traced to the fact that the stars with $\alpha \approx 1$ remain for an extended period of time on the line joining the dwarf galaxy and the perturber. For these stars the tidal force (which is strongest along this line) has the longest time to operate which results in the largest velocity increments and the largest stirring. In the context of the tidal radius calculations, the difference between the prograde and retrograde cases comes from the change of sign of the Coriolis force. The relation between the two approaches remains to be investigated and we plan to address this issue in our future work.

ACKNOWLEDGMENTS

This work was supported in part by PL-Grid Infrastructure, the Polish National Science Centre under grant 2013/10/A/ST9/00023, by US National Science Foundation Grant No. PHYS-1066293 and the hospitality of the Aspen Center for Physics. ED gratefully acknowledges the support of the Alfred P. Sloan Foundation and of the NSF Grant No. AST-1211258 and ATP-NASA Grant No. NNX14AP53G. MS benefited from the summer student program of the Copernicus Center. We thank L. Widrow for providing procedures to generate N -body models of galaxies for initial conditions.

REFERENCES

- Binney, J., & Tremaine, S. 1987, Galactic Dynamics (Princeton, NJ: Princeton Univ. Press)
- D'Onghia, E., Besla, G., Cox, T. J., & Hernquist, L. 2009, *Nature*, 460, 605
- D'Onghia, E., Vogelsberger, M., Faucher-Giguere, C. A., & Hernquist, L. 2010, *ApJ*, 725, 353
- Hénon, M. 1970, *A&A*, 9, 24
- Holmberg, E. 1941, *ApJ*, 94, 385
- Kazantzidis, S., Lokas, E. L., Callegari, S., Mayer, L., & Moustakas, L. A. 2011, *ApJ*, 726, 98
- Keenan, D. W., & Innanen, K. A. 1975, *AJ*, 80, 290
- Klimentowski, J., Lokas, E. L., Kazantzidis, S., Mayer, L., & Mamon, G. A. 2009, *MNRAS*, 397, 2015
- Kozlov, N. N., Syunyaev, R. A., & Éneev, T. M. 1972, *SPhD*, 17, 413
- Lokas, E. L., & Mamon, G. A. 2001, *MNRAS*, 321, 155
- Lokas, E. L., Kazantzidis, S., & Mayer, L. 2011, *ApJ*, 739, 46
- Lokas, E. L., Majewski, S. R., Kazantzidis, S., et al. 2012, *ApJ*, 751, 61
- Lokas, E. L., Gajda, G., & Kazantzidis, S. 2013, *MNRAS*, 433, 878
- Lokas, E. L., & Semczuk, M. 2014, in Proc. XXXVI Polish Astronomical Society Meeting, ed. A. Różańska, & M. Bejger (Warsaw, Poland: PAS), 53
- Lokas, E. L., Athanassoula, E., Debattista, V. P., et al. 2014a, *MNRAS*, 445, 1339
- Lokas, E. L., Ebrová, I., del Pino, A., & Semczuk, M. 2014b, *MNRAS*, 445, L6
- Mayer, L., Governato F., Colpi, M., et al. 2001, *ApJ*, 559, 754
- Navarro, J. F., Frenk, C. S., & White, S. D. M. 1997, *ApJ*, 490, 493 (NFW)
- Pawlowski, M. S., & Kroupa, P. 2014, *ApJ*, 790, 74
- Read, J. I., Wilkinson, M. I., Evans, N. W., Gilmore, G., & Kleyna J. T. 2006, *MNRAS*, 366, 429
- Springel, V. 2005, *MNRAS*, 364, 1105
- Springel, V., Yoshida, N., & White, S. D. M. 2001, *New Astronomy*, 6, 79
- Toomre, A., & Toomre, J. 1972, *ApJ*, 178, 623
- Widrow, L. M., & Dubinski, J. 2005, *ApJ*, 631, 838
- Widrow, L. M., Pym, B., & Dubinski, J. 2008, *ApJ*, 679, 1239



TIDALLY INDUCED OFFSET DISKS IN MAGELLANIC SPIRAL GALAXIES

STEPHEN A. PARDY¹, ELENA D'ONGHIA^{1,4}, E. ATHANASSOULA², ERIC M. WILCOTS¹, AND KARTIK SHETH³

¹Department of Astronomy, University of Wisconsin, 475 North Charter Street, Madison, WI 53706, USA; spardy@astro.wisc.edu

²Aix Marseille Université, CNRS, LAM (Laboratoire d'Astrophysique de Marseille) UMR 7326, F-13388, Marseille, France

³National Aeronautics and Space Administration (NASA) Headquarters, 300 E. Street SW, Washington, DC 20546

Received 2016 February 18; revised 2016 June 6; accepted 2016 June 20; published 2016 August 22

ABSTRACT

Magellanic spiral galaxies are a class of one-armed systems that often exhibit an offset stellar bar and are rarely found around massive spiral galaxies. Using a set of N -body and hydrodynamic simulations, we consider a dwarf–dwarf galaxy interaction as the driving mechanism for the formation of this peculiar class of systems. We investigate here the relation between the dynamical, stellar, and gaseous disk center and the bar. In all our simulations the bar center always coincides with the dynamical center, while the stellar disk becomes highly asymmetric during the encounter, causing the photometric center of the Magellanic galaxy disk to become mismatched with both the bar and the dynamical center. The disk asymmetries persist for almost 2 Gyr, the time that it takes for the disk to be recentered with the bar, and well after the companion has passed. This explains the nature of the offset bar found in many Magellanic-type galaxies, including the Large Magellanic Cloud (LMC) and NGC 3906. In particular, these results, once applied to the LMC, suggest that the dynamical center should reside in the bar center instead of the H I center as previously assumed, pointing to a variation in the current estimate of the north component of the LMC proper motion.

Key words: galaxies: dwarf – galaxies: interactions – galaxies: irregular – galaxies: kinematics and dynamics

1. INTRODUCTION

Bars are common features in today's universe. Over two-thirds of all nearby disk galaxies are barred (Sa-Sd) galaxies, including the Milky Way (e.g., de Vaucouleurs 1963; Eskridge et al. 2000; Marinova & Jogee 2007; Menendez-Delmestre et al. 2007; Sheth et al. 2008). The *Spitzer* Survey of Stellar Structure in Nearby Galaxies, S⁴G, a well-suited survey to identify bars, confirmed these results for the nearby spiral galaxies (Sheth et al. 2010; Muñoz-Mateos et al. 2013; Buta et al. 2015).

However, there is a class of low-mass stellar galaxies, named Magellanic spirals, that show evidence of relatively rare features. In particular, these galaxies are characterized by a bar whose center is displaced from that of the disk, one-armed spirals, and an otherwise normal and gas-rich disk (de Vaucouleurs & Freeman 1972). The Large Magellanic Cloud (LMC) is considered the prototype of this class of objects. However, despite a wealth of data, there is still a good deal of uncertainty concerning the nature of the LMC's bar (see D'Onghia & Fox 2015, for a review on the subject). Work by van der Marel (2001) found that the bar is offset from the dynamical center of the LMC and resides within a large stellar disk. Earlier work by Zhao & Evans (2000) described the bar as being an unvirialized structure that is offset from the rest of the disk as a result of the LMC's interaction with the Small Magellanic Cloud (SMC). Subramaniam & Subramanian (2009) used the OGLE III survey (Udalski et al. 2008) and contend that the LMC's bar resides in the plane of the disk. Lastly, there is no evidence of a bar in the H I maps of the LMC presented in Staveley-Smith et al. (2003).

The dynamics, structure, and star formation history of the LMC have long been interpreted in the context of its proximity to both the Milky Way and the SMC. The majority of the observed Magellanic spirals in the nearby universe share the

LMC's structure, in particular the evidence of an offset bar and a one-armed spiral structure, but are rarely found around massive spirals (Wilcots & Prescott 2004). A good example of these systems is offered by NGC 3906, which shows evidence of the bar offset from the photometric center of the galaxy by 1.2 kpc (see, e.g., Figure 1 of de Swardt et al. 2015), or NGC 4618 (Odewahn 1991). As more galaxies have been examined from S⁴G (Sheth et al. 2010), it has been found that these offset bars, though rare, represent as many as 5% of all barred spirals (Ross 2012; K. Sheth et al. 2016, in preparation).

The dynamics of Magellanic barred spirals is much more complex than that of standard galaxies with centered bars, as could be expected since the different components, disk and bar, have different centers. De Vaucouleurs & Freeman (1972) studied the orbital structure of such galaxies using an axisymmetric and a bar potential whose centers do not coincide. Colin & Athanassoula (1989) calculated the corresponding shifts of the Lagrangian points, as well as the response density and velocity fields in such potentials. They found that the center of the velocity field does not necessarily coincide either with the center of the bar or with that of the axisymmetric component, but may be at an intermediate position, its specific location depending on the geometry and size of the offset.

N -body simulations allowed for self-consistent modeling and the introduction of a perturbing companion. Athanassoula (1996) reproduced the one-armed morphology and noted the importance of the impact position with respect to the bar, while Bekki (2009) discussed whether the offset observed in the LMC could be due to a “dark” companion. Athanassoula et al. (1997) found that the displacements of the centers are accompanied by changes of the bar pattern speed and size. This work was extended by Berentzen et al. (2003), who introduced gas into the simulation and found that it is possible to destroy the bar while keeping the disk structure. More recently, numerical experiments suggest a dwarf–dwarf galaxy

⁴ Alfred P. Sloan Fellow.

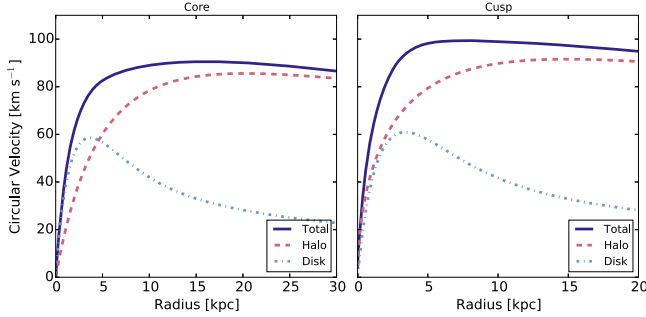


Figure 1. Rotational curves for the primary galaxy when a cored dark profile (left panel) or Hernquist profile (right panel) is adopted. Both galaxies have the same total mass. A thin exponential disk for both the stars and gas is assumed, with the combined profile shown (light-blue dot-dashed line).

Table 1
Structural Parameters of the Primary and Companion Galaxy

Parameters	Primary Galaxy		Companion
	Cored Halo	Hernquist Halo	
a (kpc) ^a	11.3	14.9	5.8
r_d (kpc) ^b	1.6	1.6	0.6
M_{DM} ($\times 10^{10} M_{\odot}$) ^c	12	12	1.1025
M_{disk} ($\times 10^{10} M_{\odot}$) ^d	2.52	2.52	0.055
M_{gas} ($\times 10^{10} M_{\odot}$) ^e	1.08	1.08	...
f_{gas} ^f	0.3	0.3	...
N_{halo} ^g	2×10^6	2×10^6	3.61×10^5
N_{disk} ^h	7×10^5	7×10^5	3×10^5
N_{gas} ⁱ	3×10^5	3×10^5	...

Notes.

- ^a Dark matter halo scale length.
- ^b Stellar and gaseous disk scale length.
- ^c Mass in dark matter.
- ^d Mass in stars.
- ^e Mass in gas.
- ^f Baryonic gas fraction.
- ^g Number of dark matter particles.
- ^h Number of stellar particles.
- ⁱ Number of gas particles.

Table 2
Orbital Parameters of Numerical Models

Model	x	y	z	Vx	Vy	Vz
		(kpc)			(km s ⁻¹)	
Cored, $\theta = 45^\circ$	29	36	29	-147	-147	-147
Cored, $\theta = 90^\circ$	0	6	50	0	0	-255
Cored, $\theta = 0^\circ$	50	7	0	-260	0	0
Cored, $\theta = 0^\circ$ Retrograde	50	7	0	-265	0	0
Hernquist, $\theta = 45^\circ$	29	35	29	-147	-147	-147
Hernquist, $\theta = 90^\circ$	0	3.75	50	0	0	-259
Hernquist, $\theta = 0^\circ$	50	3.5	0	-255	0	0
Hernquist, $\theta = 0^\circ$ Retrograde	50	3.5	0	-255	0	0

Note. The origin of the coordinate system is at the center of mass of the primary galaxy.

interaction origin for the offset bar and one-arm structure (Besla et al. 2012; Yozin & Bekki 2014). The tidal interactions between dwarf galaxies with different masses play a key role in the stellar and gas stripping in low-mass systems as a consequence of resonant interactions between spinning disks (D’Onghia et al. 2009, 2010; Gajda & Lokas 2015; Lokas et al.

2015) and explain the morphology and the origin of the Magellanic Stream (Besla et al. 2010, 2012).

In this study we aim to understand the structure and dynamics of Magellanic spirals with similar characteristics to the LMC. In particular, we explore whether direct dwarf–dwarf collisions with a mass ratio of 1:10 produce the asymmetric structures characteristic of Magellanic-type galaxies and can account for the internal morphology and kinematics of this general class of galaxies. While previous works showed that these systems can have offset bars originated by encounters with a less massive companion, here we show that the bar is never off-centered. Instead, the stellar disk is shifted from the dynamical center as a consequence of the impact with a companion galaxy.

The paper is organized as follows. In Section 2, we outline our methodology and describe numerical models involving the direct collision between a Magellanic galaxy and a companion. We then analyze the outcome of the numerical experiments in Section 3. A comparison of the models and the observations is also presented in Section 3.4. We then discuss the implications to the estimate of the LMC proper motion and conclude with a summary.

2. NUMERICAL METHODS

We carried out a set of simulations with GADGET3, a parallel TreePM smoothed particle hydrodynamics (SPH) code developed to compute the evolution of stars and dark matter, which are treated as collisionless fluids and gas. A detailed description of the code is available in the literature (Springel 2005). GADGET3 computes the short-range forces using a tree-based hierarchical multipole expansion. Pairwise particle interactions are softened with a spline kernel of scale length h_s , so that they are strictly Newtonian for particles separated by more than h_s . The resulting force is roughly equivalent to traditional Plummer softening with scale length $h \approx h_s/2.8$. For our applications the gravitational softening length is fixed to $h_s = 120$ pc throughout the evolution of the galaxy encounters.

The GADGET3 code incorporates a subresolution multiphase model of the interstellar medium (ISM) including radiative cooling (Springel & Hernquist 2003) and a fully conservative approach to integrating the equations of motion (Springel & Hernquist 2002). The simulations presented in this work include gas physics but are not aimed at describing properties of star formation or feedback.

2.1. Initial Conditions

The setup of each galaxy in our study consists of a dark matter halo and a rotationally supported disk of stars and gas. The parameters describing each component are independent, and models are chosen with orbital parameters as described below.

Each disk galaxy was generated using the GalIC code described in Yurin & Springel (2014), which uses an iterative approach for the realization of equilibrium N -body systems for given density distributions (Rodionov et al. 2009). This is achieved for arbitrary axisymmetric density structure and by taking the mutual influence of different mass components fully into account.

The initial conditions for the setup of a Magellanic-type galaxy and a companion galaxy used for all models are

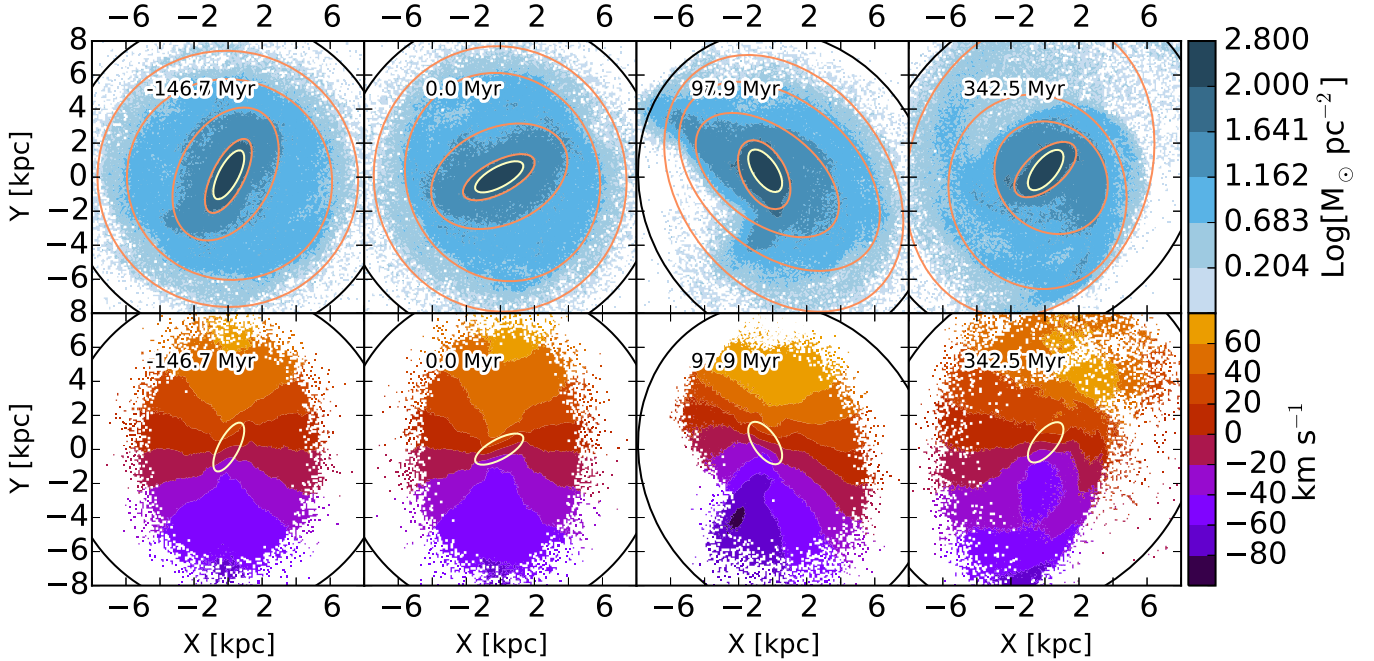


Figure 2. Time sequence of the stellar and gaseous disks of the primary galaxy. The leftmost panel corresponds to the time immediately before the companion is introduced. Time 0 ($t = 0$) is set at the time of the closest approach with the perturber. The primary galaxy is modeled here with a cored halo density model. Note that the stellar and gas distributions begin orderly but become disturbed during the encounter with the companion. The top row shows the face-on stellar disk surface density map. Isodensity ellipses (orange lines) are superimposed. The inner ellipse is used to identify the bar (yellow), while the outer ellipse outlines the disk (black). The encounter in this model is prograde with an inclination of 45° . The companion is not displayed in the image sequence. The bottom row displays the time evolution of the gas velocity fields of the same galaxy. The effect of the bar is apparent in the first panel as an asymmetry in the inner contours.

summarized in Table 1. The total mass for the Magellanic spiral is assumed to be an LMC analog, with parameters with values as in Besla et al. (2012). The companion galaxy is then chosen to be 10 times less massive than the primary galaxy.

The number of particles of each component (gas, stars, dark matter) is chosen such that the mass resolution per particle of a given type is roughly the same in both galaxies. The primary Magellanic-type galaxy is modeled with gas and stellar disks with the same scale length, with the values indicated in Table 1.

The disk component in each interacting galaxy has a thin exponential surface density profile of scale length r_d :

$$\Sigma_{\text{disk}} = \frac{M_{\text{disk}}}{2\pi r_d^2} \exp(-r/r_d), \quad (1)$$

so that the disk mass is $M_{\text{disk}} = m_d M_{\text{DM}}$, where m_d is dimensionless and M_{DM} is the total halo mass. The vertical mass distribution of the stars in the disk is specified by giving it the profile of an isothermal sheet with a radially constant scale height z_0 . The 3D stellar density of the stars and gas disk is hence given by

$$\rho_*(r, z) = \frac{M_{\text{disk}}}{4\pi z_0 r_d^2} \operatorname{sech}^2\left(\frac{z}{z_0}\right) \exp\left(-\frac{r}{r_d}\right). \quad (2)$$

The scale height of the stellar disk is adopted as 0.2 of the disk scale length. The gaseous disk height is initially set equal to the stellar disk height. The energy and pressure of the ISM are prescribed by the chosen effective equation of state (Springel et al. 2005).

The models for the primary Magellanic-type galaxy assume a dark halo with the following general form (Dehnen 1993):

$$\rho(r) = \frac{(3-\gamma)M_{\text{DM}}}{4\pi} \frac{a}{r^\gamma (r+a)^{4-\gamma}}, \quad (3)$$

where M_{DM} is the galaxy halo mass, a is the scale length of the halo, and γ is a parameter that determines the shape of the profile. For $\gamma = 1$ the halo has a central cusp and follows a Hernquist model (Hernquist 1990), while for $\gamma = 0$ the density profile belongs to the same family of density profiles but with a constant-density core. The isotropic distribution function for the energy is given in this case by (Dehnen 1993)

$$f(\epsilon) = \frac{(3-\gamma)M}{2(2\pi^2 G Ma)^{3/2}} \int_0^\epsilon \frac{(1-y)^2 [\gamma + 2y + (4-\gamma)y^2]}{y^{4-\gamma} \sqrt{\epsilon - \Psi}} d\Psi, \quad (4)$$

where $\epsilon = -E(GM/a)^{-1}$ is the dimensionless binding energy.

The total galaxy mass and disk mass fraction for the primary galaxy are fixed to be the same in both models. Additionally, the scale lengths for the cored and Hernquist halo models are set such that both galaxies have similar rotation velocity V_{tot} at the radius that enclosed the total mass of the galaxy.

Figure 1 displays the resulting rotation curves for the primary Magellanic-type galaxy when a cored density profile (left panel) or a Hernquist profile (right panel) is adopted. The initial total rotation curve of the primary galaxy peaks at $V_{\text{rot}} = 90 \text{ km s}^{-1}$ at two halo scale lengths from the center in the cored profile, whereas the peak is 100 km s^{-1} for the cusped Hernquist model at one halo scale length. This gives a total mass within 8 kpc for the cored (cusped) galaxy of

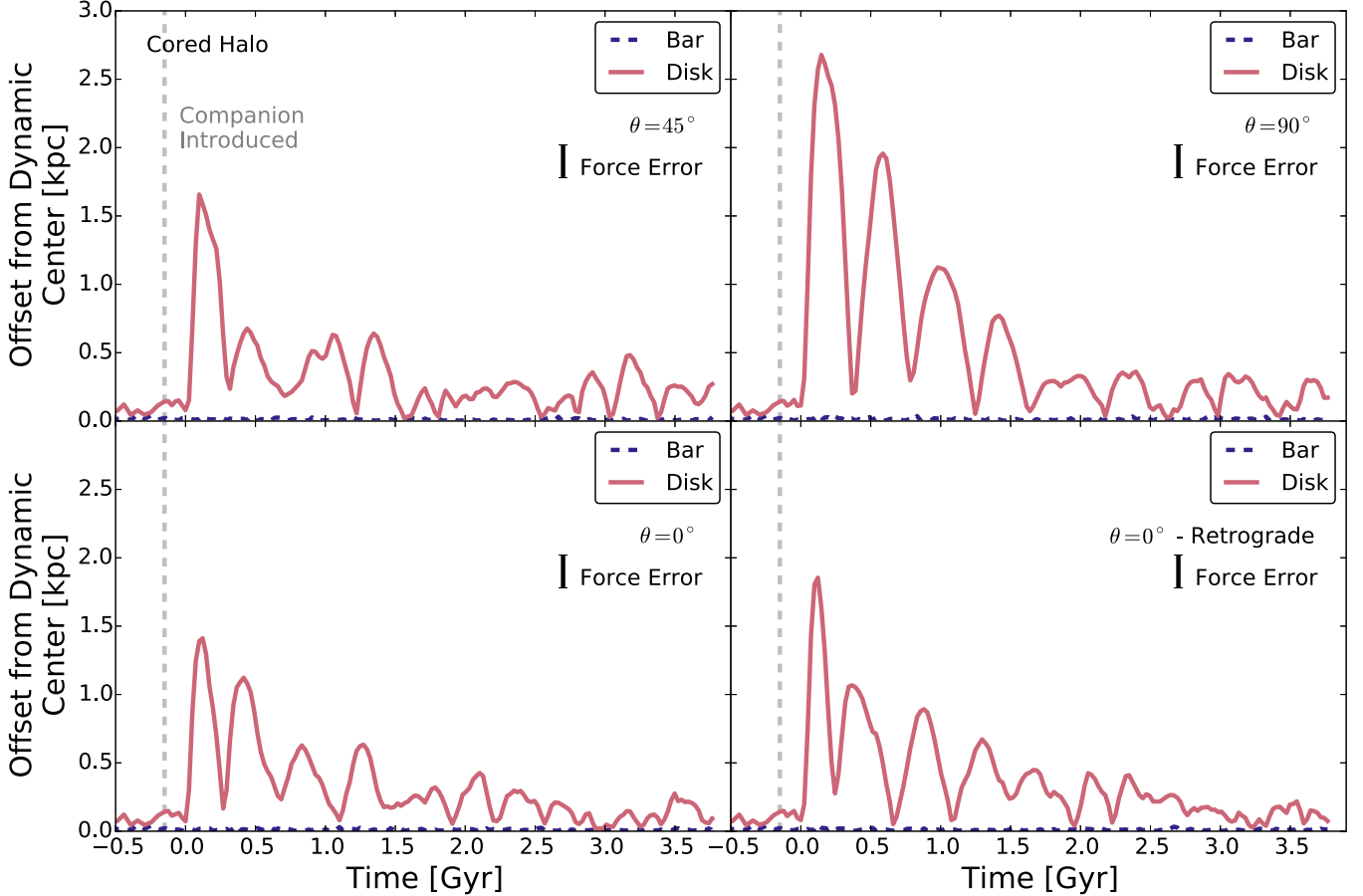


Figure 3. Time evolution of offsets between the photometric center of the disk (solid red line) and bar (dotted blue line) and the dynamical center in the cored halo model for different orbital inclination angles. The size of the error bar is twice the typical force softening length $h_s = 120$ pc. The time of closest approach is set at 0 Gyr, and we include 0.5 Gyr of evolution before the introduction of a companion. The gray vertical line indicates when the companion was introduced. Top left: $\theta = 45^\circ$. Top right: $\theta = 90^\circ$. Bottom left: $\theta = 0^\circ$. Bottom right: $\theta = 0^\circ$ (retrograde collision).

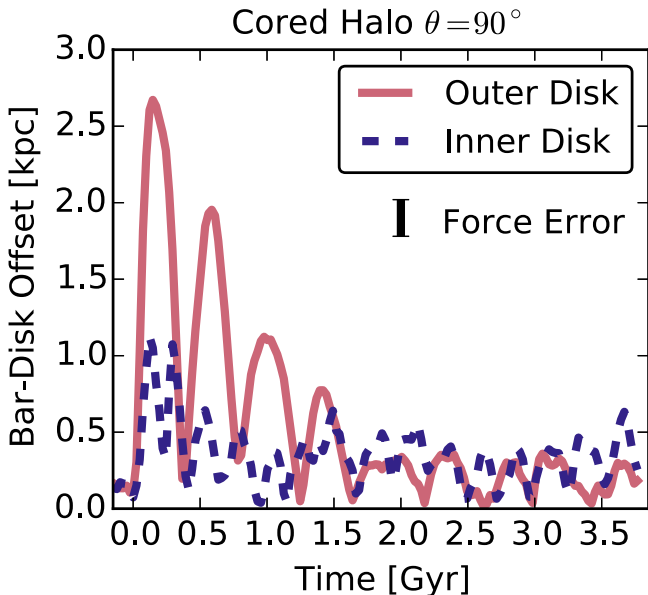


Figure 4. Time evolution of the displacement between the bar and disk centers shown for the $\theta = 90^\circ$ orbit in the cored halo. We show the effect of using a higher density cutoff, which probes the inner disk, with a typical radius of 5 kpc. The inner disk cutoff is $10.7 M_\odot \text{ pc}^{-2}$, while the outer disk cutoff is $0.5 M_\odot \text{ pc}^{-2}$. This example is the most extreme difference of any of our simulations but still shows a strong offset between the measured disk and bar centers directly after impact.

$1.35 (1.77) \times 10^{10} M_\odot$. Note that the disk fraction within $2r_d$ is higher in the cored galaxy with respect to the Hernquist galaxy.

This study focuses on the response of the disk of a Magellanic-type galaxy when perturbed by a close encounter with a lower-mass companion. The initial stellar disks of the Magellanic-type galaxies are chosen to be sufficiently bar unstable for the bar to grow fast in isolation (D’Onghia 2015); hence, the bar feature in all models has not been induced by external tidal perturbations induced by the companion (Łokas et al. 2014), but grew from the beginning of the simulation.

The perturber is modeled assuming an exponential stellar disk and a Hernquist dark matter density profile, with the choice of parameters listed in Table 1.

2.2. Orbital Configurations

Our set of simulations presents four orbital configurations for each halo model. In each set of simulations we let the primary galaxy evolve over a period of 4 Gyr in order to grow a stellar bar at the center and to settle to equilibrium before we introduced a companion. At the start of the simulation, the companion was placed at ~ 50 kpc on a fast single passage orbit. Visual inspection of the primary disk after the companion has been added shows no perturbations until the impact occurs. The initial position and velocities of the companion galaxy in the set of simulations are presented in Table 2. The values are assumed in the coordinate system at the center of mass of the

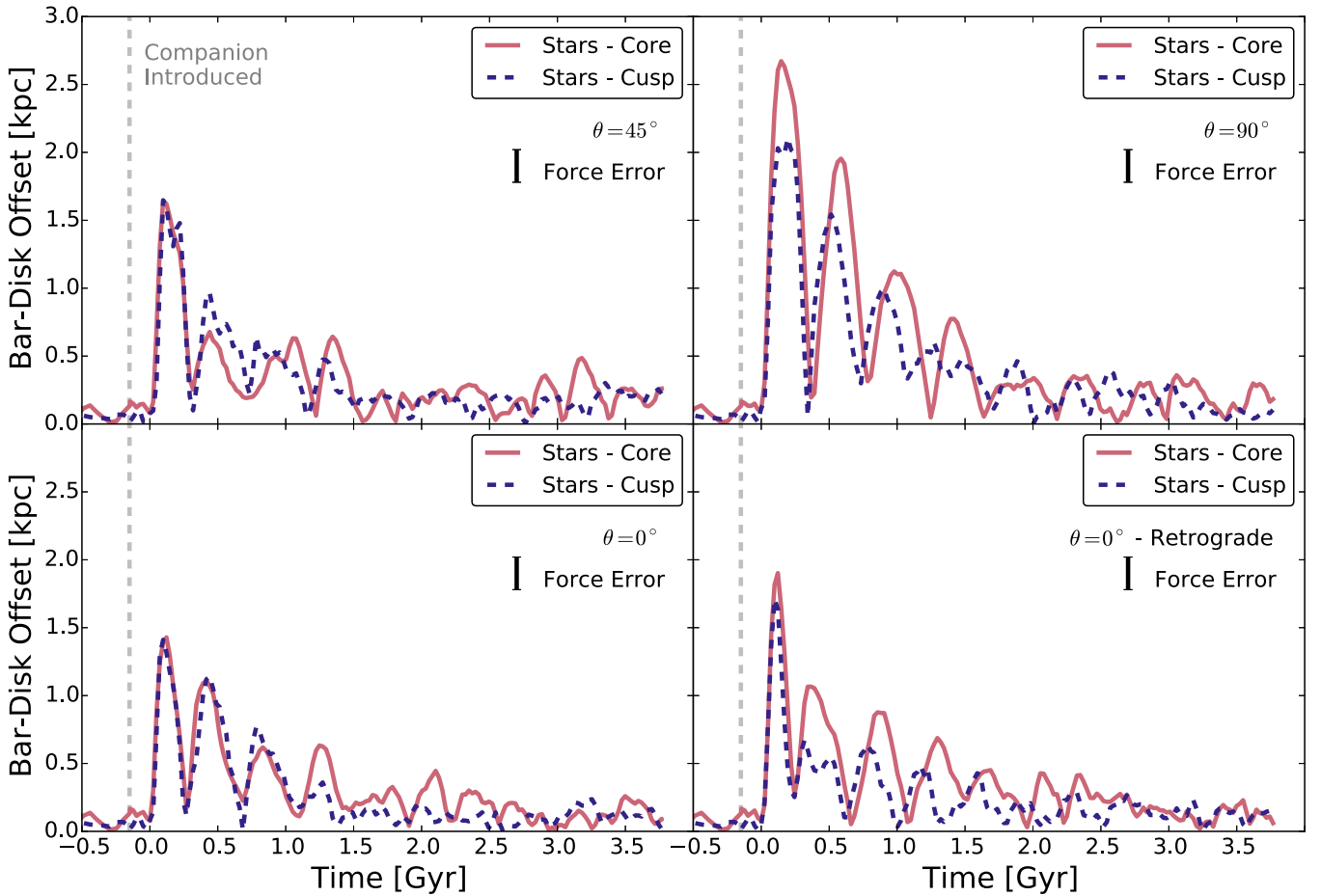


Figure 5. Time evolution of the displacement between the bar and disk centers shown for the same four orbital orientations as in Figure 3 and for both halo types. We compare models with a cored halo density profile (red lines) to models with a Hernquist inner-density profile for the dark halo (blue dashed lines). The time of closest approach is set at 0 Gyr, and we include 0.5 Gyr of evolution before the introduction of a companion.

primary galaxy. The initial orbital position and velocity of the interacting galaxies are set so that all encounters had an impact parameter of 4 ± 0.06 kpc and a relative velocity of 337 ± 4 km s $^{-1}$. This value is motivated by simulations of the LMC in which an offset bar is created by a direct impact by the SMC (Besla et al. 2012).

Two out of four orbital configurations are coplanar ($\theta = 0$). One is prograde, and the other is retrograde. The other two orbits are both prograde and inclined with respect to the plane of the primary galaxy by 45° and 90° , respectively. The encounter occurred at ~ 0.15 Gyr, and the primary galaxy was followed for 4 Gyr after the simulation started.

2.3. Quantifying Disk Off-centers and Lopsidedness

In order to quantify the bar displacement in the Magellanic-type galaxy in tidal interaction with a companion galaxy, we first need to identify the centers of the galaxy components: stellar and gas disks and the stellar bar. An observationally motivated approach has been used to define disk and bar centers as in the study of the Magellanic spiral NGC 3906 by de Swardt et al. (2015).

The stellar or gaseous disk of the primary galaxy is projected to a face-on density map with 256 square bins in each dimension. Each bin has a size of ~ 78 pc, corresponding to $\sim 1''$ resolution at the distance of the observed galaxy NGC 3906. We varied the bin size in the analysis and found the effect to be

minimal. The density map is then cut into logarithmically spaced intensity contours. Each contour is fit with ellipses. The outer ellipse serves the stellar disk, while the innermost ellipse with eccentricity greater than 0.5 outlines the bar (Yozin & Bekki 2014). Various methods have been used to identify the bar in our simulations; however, this approach produces the best fits to visual inspection and allows for comparisons with previous analyses. The bar center has also been measured adopting the brightest pixel following the suggestion of van der Marel & Kallivayalil (2014), and we found that the bar center estimated in this way agrees with the values obtained with the ellipse method, with the uncertainties estimated to be within the numerical resolution.

To find the disk and bar centers, we fit ellipses to the isodensity contours of our primary galaxy. The disk center is probed by our outermost ellipse fit, which we set at a density of $0.5 M_\odot \text{ pc}^{-2}$. The ellipse that fits this outer isodensity contour has a typical radius of 10 kpc. We tested the effect of measuring the offset from the dynamical center using a higher density cutoff of $10.7 M_\odot \text{ pc}^{-2}$. This density probes an inner disk with typical radii of 5 kpc. The inner disk shows similar qualitative results and a similar time evolution, but with reduced amplitude.

The galaxy dynamical center is defined as the location where the galaxy potential well is deepest. We measure it by taking the center of mass of the 100 particles with the most negative

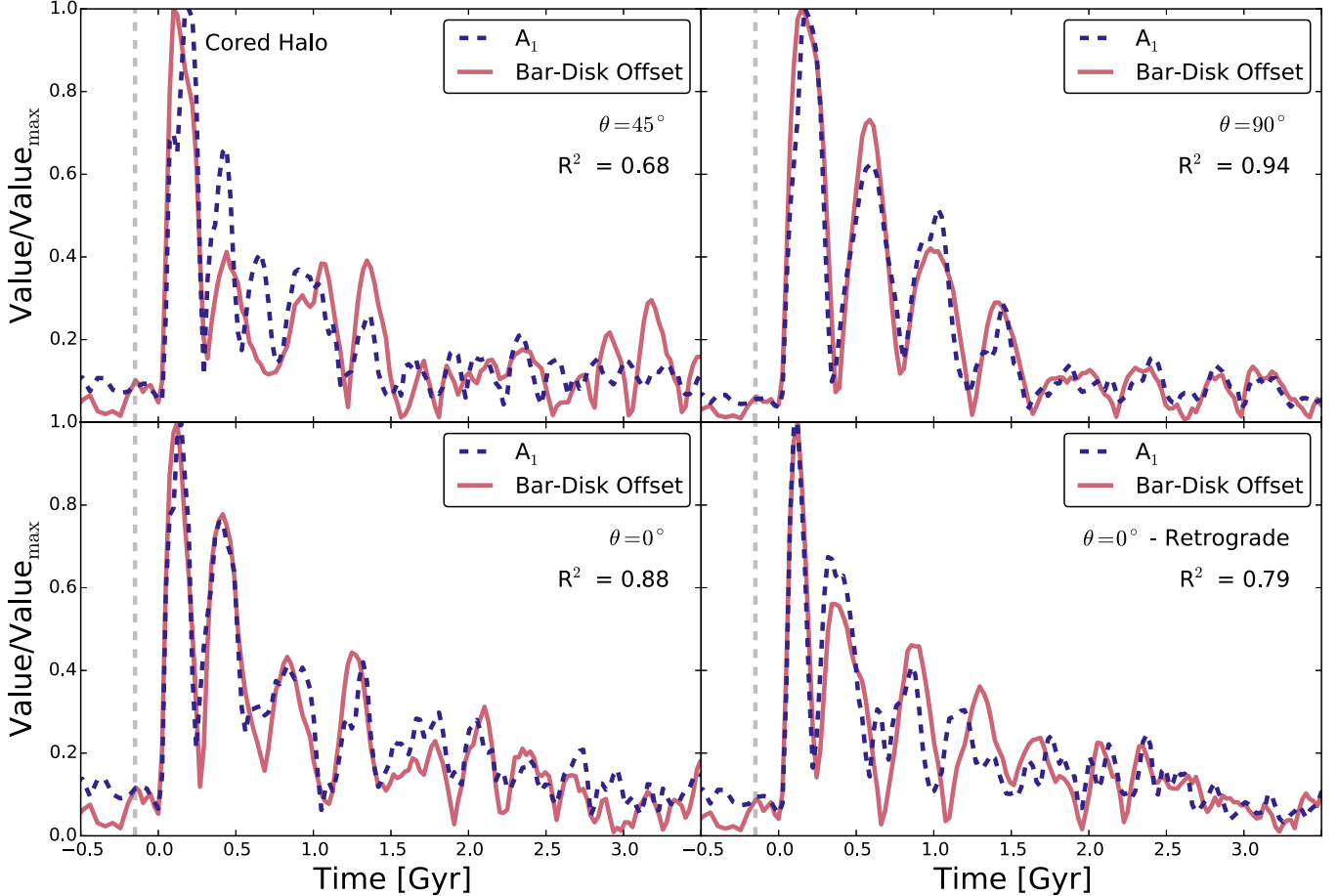


Figure 6. Time evolution of the asymmetry of the stellar disk in the cored halo compared with the bar–disk offset for the same four orbital orientations as in Figure 3. The two quantities have been normalized to their maximum value over the full time range. We show the R^2 value in each panel, quantifying the degree to which the two time series coincide.

potentials. We also measured the center of the dark matter alone by repeating the same procedure, but using only dark matter particles. Throughout the paper the bar and disk offsets refer to the displacement of that component with the galaxy dynamical center, but the implications of using the halo center instead are minimal and will be briefly discussed in Section 3.1. The in-plane separation between the disk and bar centers is used as a measure of the bar–disk offset (what is traditionally called the “offset bar”).

An example of the photometric fitting approach applied to the stellar primary galaxy during the gravitational encounter with a companion is illustrated in Figure 2 (top row), which shows the projected surface density and isodensity ellipses superimposed (orange lines). The inner ellipse (yellow line) identifies the stellar bar, and the outer ellipse (black line) fits the outer stellar disk. The panels are labeled by time, with the initial time of the simulation set to the time when the companion is first introduced and $t = 0$ as the time when the perturber hits the disk of the primary galaxy.

2.4. Quantifying the Disk Lopsidedness

In our simulations the asymmetries of the stellar disk and the lopsidedness are determined by projecting the disk face-on and measuring its stellar surface density, $\Sigma(r, \phi)$, with (r, ϕ) being polar coordinates in the disk plane. If the surface brightness distribution is invariant for a rotation of $2\pi/m$ rad, so that

$\Sigma(r, \phi + 2\pi/m) = \Sigma(r, \phi)$, then the galaxy has m -fold rotational symmetry and has m arms and a bar for $m = 2$.

If the surface brightness is expressed as a Fourier series, then the disk lopsidedness, the strength of the bar, and the amplitude of the spiral structure can be measured from its Fourier components, which are calculated as

$$\begin{aligned} \Sigma_{mc}(r) &= 2 \langle \Sigma(r, \phi) \cos m\phi \rangle \\ \Sigma_{ms}(r) &= 2 \langle \Sigma(r, \phi) \sin m\phi \rangle \\ \text{for } m &= 1, 2, \dots, \infty \\ \Sigma_0 &= 2 \langle \Sigma(r, \phi) \rangle. \end{aligned} \quad (5)$$

The amplitude of each Fourier component is calculated relative to Σ_0 and can take values between 0 and 1:

$$A_m = \frac{\sqrt{\Sigma_{mc}^2 + \Sigma_{ms}^2}}{\Sigma_0}. \quad (6)$$

The face-on disk is divided into concentric annuli, which are further divided into azimuthal bins. The mass from the star particles is then assigned to these bins, making it possible to compute the stellar surface density $\Sigma(r, \phi)$. Fourier components of the surface density are then calculated according to Equation (5).

Following Zaritsky & Rix (1997) and Zaritsky et al. (2013), we then measure the average of the Fourier components’

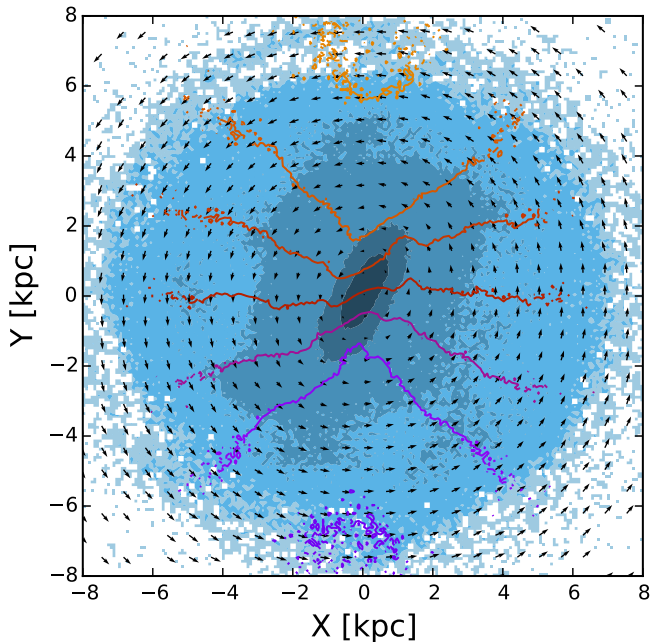


Figure 7. Velocity fields of the stellar and gas components overlaid on the stellar density distribution from the primary galaxy just before the encounter with the companion galaxy occurs. This model assumes a cored halo profile for the primary galaxy. The blue filled contours in the background display the stellar density distribution as in the first row of Figure 2. The colored contours show the gaseous velocity fields as in the bottom row of Figure 2. The arrows show the average stellar motion in the x - y plane in each pixel. Note that only 1/8 of the arrows are plotted here to improve clarity.

amplitudes $\langle A_m \rangle$ (for $m = 1$ and $m = 2$) between 1.5 and 2.5 scale lengths (2.2–3.7 kpc for the disk scale length of 1.4 kpc). We repeat this measurement during the time of the interaction between the primary galaxy and the companion to track the growth of asymmetries and the strength of the bar.

2.5. Gas Disk Velocity Fields

A weighted two-dimensional velocity map for the gas is inferred in our simulations projecting the galaxy as if it had been observed at a certain inclination and then taking the mass-weighted average of the radial velocity components of the gas particles. An example of two-dimensional velocity maps is illustrated in the bottom row of Figure 2, where the galaxy is observed with an inclination of 45° starting before the companion is introduced and following several gigayears of evolution.

3. RESULTS

3.1. Stellar Disk Dynamical Response

We investigate perturbations induced in the stellar disk of the primary galaxy by a recent encounter with a companion exploring four different orbital configurations: a coplanar (prograde and retrograde) and an inclined orbit of 45° and 90° , respectively.

Figure 2 shows the live disk displayed face-on during the 45° direct encounter with the companion. In this numerical experiment the disk galaxy is embedded in a cored dark matter halo. There are observed asymmetries in the mass distribution of the stellar disk noticeable in the outer parts, which appear shortly after the encounter.

Next, we measured the dynamical center, the bar, and the disk photometric center. Concentric ellipses are superimposed to the disk surface density as shown in Figure 2. The inner ellipse—marked in yellow—outlines the bar, and the ellipse colored in black matches the outer disk density. The time of closest approach happens roughly 0.15 Gyr from the beginning of the simulation. The companion galaxy passes through the primary galaxy quickly (~ 0.1 Gyr within 20 kpc of the primary galaxy) and is within the virial radius of the primary galaxy for < 0.5 Gyr.

We repeated the experiment with different sets of models varying the orbital inclination angle. We measure the displacements between the dynamical center, the stellar disk, and the bar. Figure 3 quantifies the displacement of the bar and the stellar disk from the dynamical center and displays it as a function of time for encounters run with different orbital inclinations. We also ran our experiments on the isolated disks to measure the intrinsic scatter. In general, this scatter is quite low and well behaved.

After the encounter with the companion (labeled as $t = 0$), the stellar disk responds to the gravitational perturbation by becoming asymmetric in its mass distribution (see the third panel in Figure 2). We note first that the measured bar center is always coincident with the dynamical center. Hence, there is no evidence of off-center bars for any orbital configuration. The stellar disk, however, is measured to be 1.5–2.5 kpc shifted from the dynamic center of each primary galaxy. This readjustment of the disk occurs over a period of approximately 2 Gyr, with small offsets of ~ 0.5 kpc persisting for another 2 Gyr. During this time, the disk center will be displaced with respect to the bar center up to 2.5 kpc for encounters with orbital inclination angles of 90° (the largest of the observed shifts).

The displacement of the primary galaxy's stellar disk is caused by the companion galaxy passing through the disk. This fly-by creates strong asymmetries by scattering stars to large radii on one side of the galaxy. This effect is more severe when the impact occurs in the 90° orbit, producing the strongest disk response and largest displacements from the dynamical center. In some cases, the asymmetric material appears as a single spiral arm.

The disk distortions and asymmetries persist for almost 2 Gyr, the time that it takes for the disk to be recentered, and well after the perturber has passed. The response of the stellar disk appears to oscillate with time as it reduces amplitude, as also noted in Yozin & Bekki (2014). The primary offset is the most prominent. The subsequent offsets have amplitudes that decrease strongly with the time since the interaction and soon reach values close to our spatial resolution limits and do not appear to be correlated with disk rotation or other disk properties.

We also tested the offset using the center of the dark matter halo instead of the dynamical center. The dark matter halo center is aligned with the dynamical center before the interaction but becomes offset from both the dynamical center and the bar during the passage of the companion. After the interaction ends, the halo and dynamical centers coincide again and align with the bar.

During testing of our orbital configurations, we made runs with various impact parameters. We took care to hold the impact parameter constant across all simulations with different

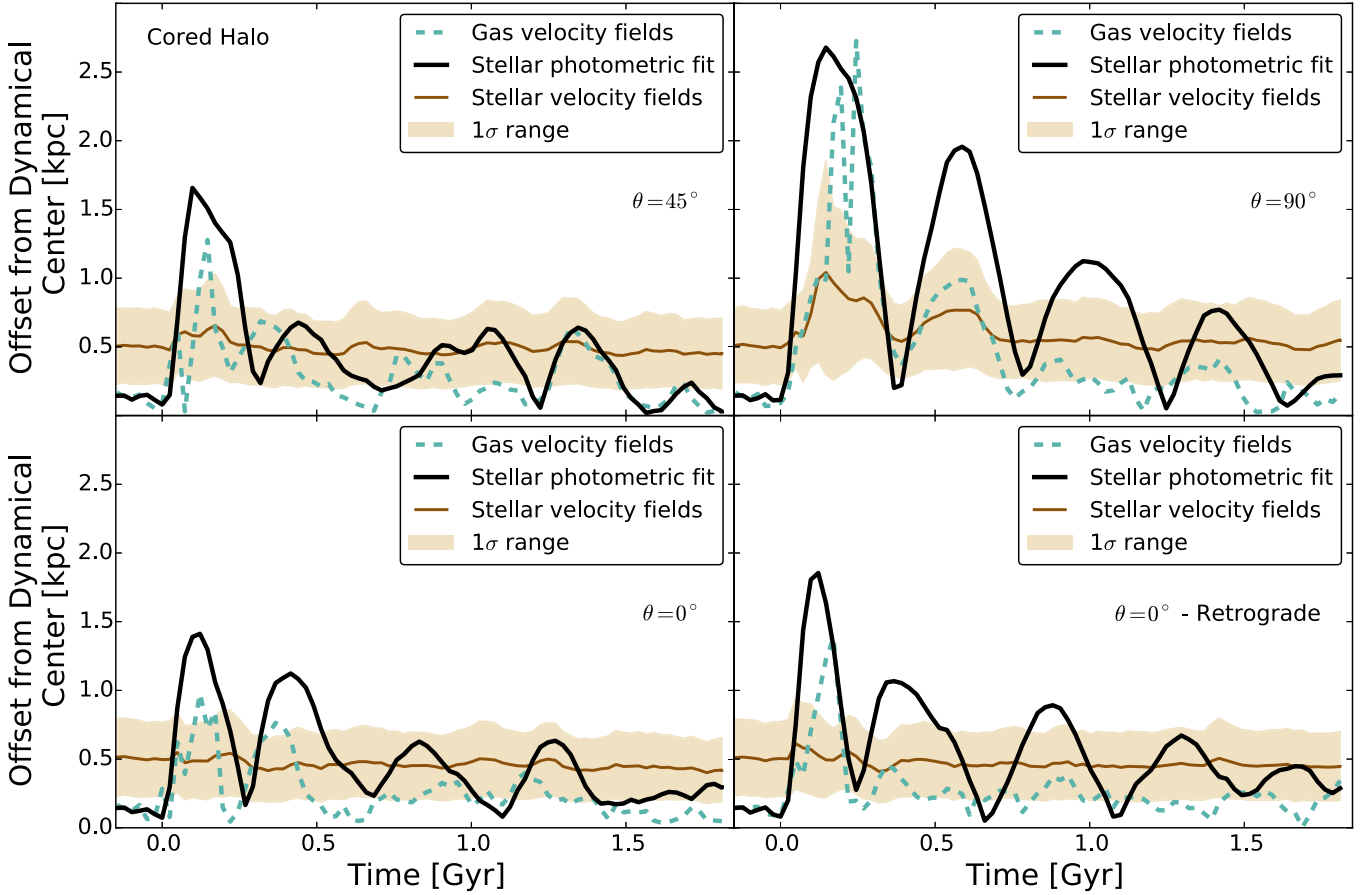


Figure 8. Time sequence of offset between gas and stellar disk and the dynamical center as measured by using different methods and for encounters with different orbital configurations. The primary galaxy has a cored halo profile. Centers of the disk measured from the photometric ellipse fitting are shown (thick black line). Centers of the gaseous disk measured using 2D tilted ring fitting of the gaseous velocity field by DiskFit are also displayed (dotted blue line) and compared to centers of the stellar disk as measured using the average in-plane velocity of the stars (thin brown line). The solid line shows the average of all 10,000 trials (see discussion in Section 3.5), and the filled region shows the standard deviation of all the trials.

configurations. Decreasing the impact parameter increased the observed bar–disk offset and measured asymmetries.

As a final test of these results, we experimented with fitting an ellipse to a higher-density region of the disk. This ellipse probes the inner disk of the primary galaxy (defined by a density cutoff of $10.7 M_{\odot} \text{ pc}^{-2}$), with a typical radius of 5 kpc (vs. our outer disk cutoff of $0.5 M_{\odot} \text{ pc}^{-2}$, which has a typical radius of 10 kpc). As an example in Figure 4, we show only the most different result between the inner and outer disk, which occurs for the $\theta = 90^\circ$ orbit in the cored halo. Although the qualitative results are the same, with an offset directly after the encounter followed by a gradual damping, the amplitude of the effect is strongly reduced when using the center of the inner disk.

3.2. Dependence on the Shape of Halo Density Profile

There is some evidence that dwarf disk galaxies do show slowly rising rotation curves that would be consistent with having underlying halos with shallow inner-density profiles (de Blok et al. 2001; McGaugh 2002; Oh et al. 2011; but see also Oman et al. 2015). Indeed, if Magellanic disk galaxies are embedded in halos with less concentrated mass distributions in the inner regions, then we may expect an enhancement in the

amplitude of the disk oscillations around the dynamical center. If off-centered bars are a real phenomenon, then it is plausible to posit that these oscillations would cause the bar to remain more offset, and for longer, than in a galaxy with a cosmological dark matter halo. To test whether this was driving the offsets seen in the previous section, we also set up models for the Magellanic disk galaxy with a cusped Hernquist dark matter density profile in the inner parts.

Figure 5 illustrates the outcome. Different panels display the time evolution of the disk and bar offset for encounters (the in-plane separation between the measured bar and disk centers) with different orbital configurations. The largest differences are seen in the 90° orbit, where the maximum (average) displacement is 0.6 (2.7) kpc for the cored profile, compared to 0.5 (2.1) kpc for the cusped profile. The separation measured for the coplanar retrograde 0° case consists of the maximum offset of 0.4 (1.9) kpc for the cored profile, as compared to the displacement of 0.3 (1.7) kpc measured for the cusped profile.

The 45° inclined orbit shows a slightly stronger offset for the model with the cusped halo, but this difference and the difference seen in the coplanar prograde ($\theta = 0^\circ$) orbit are both close to the spatial resolution of our models. These results support the conclusion that the bar–disk offsets are driven by asymmetries in the outer part of the disk.

3.3. Stellar Disk Lopsidedness

If offsets are the results of an asymmetric disk in the outer parts, then we expect this to appear in the Fourier component analysis. To test this, the Fourier components of the stellar disk of the primary galaxy have been measured as a function of time, during the interaction with the companion and long after the encounter ended. Our galaxies begin with strong A_2 amplitudes, indicating symmetric stellar features, and low A_1 amplitudes.

The outcome is displayed in Figure 6 for the primary galaxy with a cored halo. The results for the Hernquist halo are qualitatively similar. The four panels show the A_1 and bar-disk offset normalized to their maximum value in the four orbital configurations.

We find that A_1 becomes pronounced during the peaks of the observed bar-disk offset. These peaks line up remarkably well for ~ 2 Gyr after the encounter, at which point the offsets subside. We can quantify the degree to which the two time series coincide by measuring the R^2 coefficient:

$$R^2 = 1 - \frac{\sum_{t=0}^4 (o(t) - \bar{o}(t))^2}{\sum_{t=0}^4 (o(t) - f(t))^2}, \quad (7)$$

where, in this case, $o(t)$ is the measured bar-disk offset at time t normalized to its maximum value and $f(t)$ is the A_1 fourier amplitude at time t normalized to its maximum value. An R^2 value of 1 would indicate that the value of the A_1 mode can explain 100% of the bar-disk offsets, while an R^2 value of 0 would indicate that the A_1 mode cannot explain any of the bar-disk offsets. It is important to note, however, that this value merely describes the similarity of the two data sets and cannot prescribe any physical causation one way or the other. The lowest R^2 coefficient is found for the $\theta = 45^\circ$ configuration with $R^2 = 0.68$. The highest value is found for the $\theta = 90^\circ$ configuration with $R^2 = 0.94$.

In every orbital configuration modeled except when $\theta = 0^\circ$ in a retrograde orbit, A_1 becomes the dominant mode directly after encounter and remains elevated from its initial amplitude for the entire 4 Gyr. For the $\theta = 0^\circ$ retrograde orbit A_1 is dominant for a short period of time and settles within 3 Gyr. Using the criteria of Bournaud et al. (2005) and Mapelli et al. (2008) ($A_1 \geq 0.05$), the galaxies showing evidence for bar-disk offsets all appear asymmetric during these periods, a result also found in Athanassoula et al. (1997) and Berentzen et al. (2003). The average bar amplitude in our cored halo shows a modest decrease after the interaction.

Although qualitatively similar (both show higher A_2 amplitudes before the interaction with the companion and strong A_1 amplitudes during the tidal interaction), the results for the Hernquist halo have a number of notable differences. The Hernquist Fourier component is $A_2 < 0.2$ before interaction, even though the galaxy appears strongly barred according to our visual inspection. During the tidal interaction, both A_1 and A_2 dominate over the higher Fourier components.

Because of this, we can conclude that the shift of the disk center away from the dynamical center is due to the extended tidal material created after the interaction with the smaller companion. The method of measuring disk centers using fits to isodensity contours appears to be sensitive to larger asymmetric features on the edge of the disk. This conclusion is further supported by the fact that the typical radius measured by the outer isodensity contours increases during the encounter with the companion.

3.4. Gas Disk Dynamical Response

In the simulations described in the previous sections, we showed that the bar accurately reflects the dynamical center, while the stellar disk exhibits a prominent offset. Wilcots & Prescott (2004), however, find that the majority of the observed Magellanic galaxies have H I profiles no more or less asymmetric than other late-type spirals found in Matthews & Gallagher (2002). To test the effects of the gravitational encounter with a companion on the gas distribution of the primary galaxy, we measured the centers of the simulated gas velocity fields adopting a 2D nonaxisymmetric disk model as implemented the code DISKFIT (Spekkens & Sellwood 2007; Sellwood & Zánmar Sánchez 2010). This method uses a nonaxisymmetric model to fit the kinematic data of the gas particles within a radius of 14 kpc and compares with previous methods.

To further test how the asymmetries appear in the velocity distributions, we measure the average in-plane velocity of the disk stars in the each pixel of our surface density map. We demonstrate this method by superposing the velocity vectors on the surface density in Figure 7. This method is similar to the one applied to the LMC stellar disk using proper-motion rotation fields by van der Marel & Kallivayalil (2014).

The centers obtained with this method at each time are compared to the dynamical center as previously measured and displayed in Figure 8. The stellar photometric center obtained by fitting ellipses to the stellar disk and bar is shown (solid black line), as compared to the gas velocity field center measured by DiskFit (dotted blue line), and with the stellar velocity field center described above (solid brown line).

First, we notice that the velocity field center of the stellar disk is never coincident with the dynamical center, defined as the location of the deepest potential well, but it is always displaced on average 0.5 kpc, and with a maximum displacement of ~ 1 kpc when $\theta = 90^\circ$.

Our findings are in agreement with Magellanic spiral galaxies observed in the field. In these systems the dynamical center, usually assumed to be traced from H I rotation curves, is coincident with the center of the bar and offset with respect to the photometric center of the stellar disk, as shown in the Magellanic galaxy NGC 4027 (Phookun et al. 1992) and in NGC 3906 (Watson et al. 2011; de Swardt et al. 2015). Similar behavior was found by Matthews & Gallagher (2002) studying a sample of typical late-type spiral galaxies. In particular, the latter work showed that the global H I profiles were generally symmetric and traced the center of the galaxy's potential even when the optical image or kinematic data showed asymmetry.

We also observe that the center location found for the gas velocity field is different than the center location of the stellar disk as measured by the outer ellipse. Minor offsets between the gas and stars, like the one we find here, have been seen before in spiral arms created during encounters with lower-mass companions (Pettitt et al. 2016) and along the leading edges of strong central bars (Prendergast 1983; Athanassoula 1992; Sheth et al. 2002).

3.5. Determination of the LMC Dynamical Center

There have been some questions raised about whether the bar in the LMC is a real dynamical feature. Zaritsky (2004) argues that it might be a triaxial bulge viewed edge-on, but Subramaniam & Subramanian (2009) show that the bar is

clearly part of the disk and may be influencing the gas (Indu & Subramaniam 2015).

The bar is thought to be offset from the disk center (van der Marel 2001) and from the dynamical center as measured from H_I kinematic tracers (Luks & Rohlfs 1992; Kim et al. 1998; van der Marel 2001). Interestingly, the bar and outer disk are both consistent, within the estimated uncertainties, with the dynamical center as traced by the line-of-sight velocities of carbon stars (van der Marel et al. 2002).

Using stellar proper-motion fields, van der Marel & Kallivayalil (2014) determined a more accurate dynamic center that is coincident with the H_I center. According to our results, such an offset can occur very soon after the encounter with a companion, as was likely the case with the LMC ∼200 Myr ago (Besla et al. 2012) when it collided with the SMC.

Following van der Marel & Kallivayalil (2014) (their Figure 2), we mapped the center of our simulated two-dimensional stellar velocity map of the LMC analog primary galaxy after the collision with the SMC analog. In order to mock the observed stellar velocity map, we chose a sample of 22 fields (the number of fields used in the analysis of van der Marel & Kallivayalil 2014) within 5 kpc of the disk center of mass and fit the rotation curve:

$$V(r) = V_0 \times \min[r/R_0, 1], \quad (8)$$

with $r = \sqrt{(x - x_0)^2 + (y - y_0)^2}$. Here (x_0, y_0) are center coordinates, V_0 is the maximum velocity, and R_0 is the turnover radius. We repeat this sampling process 10,000 times at each time step, mocking the process of observing a random population of stars of the galaxy as in the observations. We measure in this way at each time a systematic offset from the true dynamical center, traced in our simulations by the location where the potential is deepest. The displacement is amplified during the collision as shown in Figure 8 (solid brown line).

Our results predict that the halo center of the LMC is coincident with the bar center and that the H_I centers will realign with this center over the next few hundred million years. If confirmed, this finding suggests that the bar center should be assumed as the dynamical center instead of the H_I center that has been previously used (Kallivayalil et al. 2013). This choice would increase the north component direction of the proper-motion measurements, μ_N , from the current value $\mu_N = 0.229 \pm 0.047$ to values close to the previous estimate of $\mu_N = 0.34$ (van der Marel et al. 2002). The north component of the proper motion of the LMC controls the location of the orbit when projected on the plane of the sky. This correction will increase the offset between the LMC’s orbit and the position of the Magellanic Stream, an issue still unsolved in the studies on the origin of the Magellanic Stream.

4. DISCUSSION AND CONCLUSIONS

We have investigated the perturbations induced in the stellar and gas disk and the bar of a Magellanic-type spiral galaxy by a fly-by with a companion. A set of numerical experiments have been studied varying the angle between the orbital plane and the equatorial plane of the primary galaxy. The dynamical response of the disk has also been analyzed for a cored or Hernquist dark halo profile for the Magellanic-type galaxy. The results can be summarized as follows:

1. The bar center is always coincident with the dynamical center, suggesting that, contrary to common belief, the

bar is never displaced in Magellanic spiral galaxies. Instead, the stellar disk is measured to be shifted from the dynamic center and the bar of the primary galaxy by, at most, 1.5–2.5 kpc, depending on the details of the encounter with the companion. Thus, the observed displacements should, on average, be well below this value, in good agreement with observations (e.g., Feitzinger 1980). The disk distortions and asymmetries persist for almost 2 Gyr, the time that it takes for the disk to be recentered, and well after the interaction with the companion ended. The disk sloshing around the dynamical center reduces in amplitude with time.

2. Disk asymmetries are slightly more pronounced in Magellanic galaxies with a cored halo profile as compared to models with a cuspy halo profile for the dark matter, but the differences are modest. The largest response of the disk of the primary galaxy tidally induced by the passage of the companion occurs for smaller impact parameters and depends on the orientation of the orbital plane with respect to the primary galaxy’s equatorial plane.
3. The gas disk also sloshes similarly to the stellar disk during the gravitational interaction with the companion, but with a modest amplitude, and it tends to recenter after a short time due to the dissipative nature of the gas.
4. These results, when applied to the LMC—the prototype of the Magellanic spiral galaxies—suggest that the dynamical center should reside in the bar center instead of the H_I center usually assumed in previous works. This choice would imply a change in the north component of the LMC proper-motion estimates, perhaps pointing to interesting implications for the offset between the LMC’s orbit and the position of the Magellanic Stream. However, the little observational evidence of a bar in the H_I gas distribution (Staveley-Smith et al. 2003) remains a challenge for theoretical models.

Our results might be of interest for interpreting the recent discoveries of bulgeless galaxies with off-center “nuclear” clusters (J. S. Gallagher 2016, private communication). This is a larger class of objects with stellar disks showing mismatched photometric centers. According to our results, their dynamical centers are likely to reside in the nuclear clusters, while the irregularities and asymmetries of the stellar disks should be interpreted as the outcome of tidally induced distortions.

Support for this research was provided by the University of Wisconsin–Madison Office of the Vice Chancellor for Research and Graduate Education with funding from the Wisconsin Alumni Research Foundation. This research is also funded by NSF Grant No AST-1211258 and ATP NASA Grant No NNX144AP53G. E.D. gratefully acknowledges the support of the Alfred P. Sloan Foundation. E.A. acknowledges financial support from the EU Programme FP7/2007-2013/, under REA grant PITN-GA-2011-289313, and from CNES (Centre National d’Etudes Spatiales, France). We express our appreciation to the Aspen Center for Physics for their hospitality, funded by the NSF under Grant No. PHYS-1066293. Simulations have been run on the High Performance Computing cluster provided by the Advanced Computing Infrastructure (ACI) and Center for High Throughput Computing (CHTC) at

the University of Wisconsin. This research made use of Astropy,⁵ a community-developed core Python package for Astronomy (Astropy Collaboration, 2013). This research made use of the Pathos⁶ multiprocessing library (McKerns et al. 2012). This research has made use of the NASA/IPAC Extragalactic Database (NED), which is operated by the Jet Propulsion Laboratory, California Institute of Technology, under contract with the National Aeronautics and Space Administration, and NASA’s Astrophysics Data System.

REFERENCES

- Athanassoula, E. 1992, *MNRAS*, **259**, 345
- Athanassoula, E. 1996, in ASP Conf. Ser. 91, Barred Galaxies, ed. R. Buta, D. A. Crocker, & B. G. Elmegreen, (San Francisco, CA: ASP), 309
- Athanassoula, E., Puerari, I., & Bosma, A. 1997, *MNRAS*, **286**, 284
- Bekki, K. 2009, *MNRAS Letters*, **393**, L60
- Berentzen, I., Athanassoula, E., Heller, C. H., & Fricke, K. J. 2003, *MNRAS*, **341**, 343
- Besla, G., Kallivayalil, N., Hernquist, L., et al. 2010, *ApJL*, **721**, L97
- Besla, G., Kallivayalil, N., Hernquist, L., et al. 2012, *MNRAS*, **421**, 2109
- Bournaud, F., Combes, F., Jog, C. J., & Puerari, I. 2005, *A&A*, **438**, 507
- Buta, R. J., Sheth, K., Athanassoula, E., et al. 2015, *ApJS*, **217**, 32
- Colin, J., & Athanassoula, E. 1989, *A&A*, **214**, 99
- de Blok, W. J. G., McGaugh, S. S., Bosma, A., & Rubin, V. C. 2001, *ApJL*, **552**, L23
- de Swardt, B., Sheth, K., Kim, T., et al. 2015, *ApJ*, **808**, 90
- de Vaucouleurs, G. 1963, *ApJS*, **8**, 31
- de Vaucouleurs, G., & Freeman, K. C. 1972, *VA*, **14**, 163
- Dehnen, W. 1993, *MNRAS*, **265**, 250
- D’Onghia, E. 2015, *ApJL*, **808**, L8
- D’Onghia, E., Besla, G., Cox, T. J., & Hernquist, L. 2009, *Natur*, **460**, 605
- D’Onghia, E., & Fox, A. J. 2015, arXiv:1511.05853
- D’Onghia, E., Vogelsberger, M., Faucher-Giguere, C.-A., & Hernquist, L. 2010, *ApJ*, **725**, 353
- Eskridge, P. B., Frogel, J. A., Pogge, R. W., et al. 2000, *AJ*, **119**, 536
- Feitzinger, J. V. 1980, *SSRv*, **27**, 35
- Gajda, G., & Lokas, E. L. 2015, arXiv:1508.03149
- Hernquist, L. 1990, *ApJ*, **356**, 359
- Indu, G., & Subramaniam, A. 2015, *A&A*, **573**, A136
- Kallivayalil, N., van der Marel, R. P., Besla, G., Anderson, J., & Alcock, C. 2013, *ApJ*, **764**, 161
- Kim, S., Staveley-Smith, L., Dopita, M. A., et al. 1998, *ApJ*, **503**, 674
- Lokas, E. L., Athanassoula, E., Debattista, V. P., et al. 2014, *MNRAS*, **445**, 1339
- Lokas, E. L., Semczuk, M., Gajda, G., & D’Onghia, E. 2015, *ApJ*, **810**, 100
- Luks, T., & Rohlfs, K. 1992, *A&A*, **263**, 41
- Mapelli, M., Moore, B., & Bland-Hawthorn, J. 2008, *MNRAS*, **388**, 697
- Marinova, I., & Joge, S. 2007, *ApJ*, **659**, 1176
- Matthews, L. D., & Gallagher, J. S. I. 2002, *ApJS*, **141**, 429
- McGaugh, S. S. 2002, in *The Shapes of Galaxies and Their Dark Halos*, Proc. of the Yale Cosmology Workshop (Singapore: World Scientific), 186 (<http://www.worldscientific.com/worldscibooks/10.1142/4886>)
- McKerns, M. M., Strand, L., Sullivan, T., Fang, A., & Avazis, M. A. G. 2012, arXiv:1202.1056
- Menendez-Delmestre, K., Sheth, K., Schinnerer, E., Jarrett, T. H., & Scoville, N. Z. 2007, *ApJ*, **657**, 790
- Muñoz-Mateos, J. C., Sheth, K., Gil de Paz, A., et al. 2013, *ApJ*, **771**, 59
- Odewahn, S. C. 1991, *AJ*, **101**, 829
- Oh, S.-H., Brook, C., Governato, F., et al. 2011, *AJ*, **142**, 24
- Oman, K. A., Navarro, J. F., Fattahi, A., et al. 2015, *MNRAS*, **452**, 3650
- Pettitt, A. R., Tasker, E. J., & Wadsley, J. W. 2016, *MNRAS*, **458**, 3990
- Phookun, B., Mundy, L. G., Teuben, P. J., & Wainscoat, R. J. 1992, *ApJ*, **400**, 516
- Prendergast, K. H. 1983, in IAU Symp. 100, Internal Kinematics and Dynamics of Galaxies, 215
- Rodionov, S. A., Athanassoula, E., & Sotnikova, N. Y. 2009, *MNRAS*, **392**, 904
- Ross, A. 2012, *BAAS*, **219**, 417.06
- Sellwood, J. A., & Zánmar Sánchez, R. Z. 2010, *MNRAS*, **404**, 1733
- Sheth, K., Elmegreen, D. M., Elmegreen, B. G., et al. 2008, *ApJ*, **675**, 1141
- Sheth, K., Regan, M., Hinz, J. L., et al. 2010, *PASP*, **122**, 1397
- Sheth, K., Vogel, S. N., Regan, M. W., et al. 2002, *AJ*, **124**, 2581
- Spekkens, K., & Sellwood, J. A. 2007, *ApJ*, **664**, 204
- Springel, V. 2005, *MNRAS*, **364**, 1105
- Springel, V., Di Matteo, T., & Hernquist, L. 2005, *MNRAS*, **361**, 776
- Springel, V., & Hernquist, L. 2002, *MNRAS*, **333**, 649
- Springel, V., & Hernquist, L. 2003, *MNRAS*, **339**, 289
- Staveley-Smith, L., Kim, S., Calabretta, M. R., Haynes, R. F., & Kesteven, M. J. 2003, *MNRAS*, **339**, 87
- Subramaniam, A., & Subramanian, S. 2009, *ApJL*, **703**, L37
- Udalski, A., Szymanski, M. K., Soszynski, I., & Poleski, R. 2008, *AcA*, **58**, 69
- van der Marel, R. P. 2001, *AJ*, **122**, 1827
- van der Marel, R. P., Alves, D. R., Hardy, E., & Suntzeff, N. B. 2002, *AJ*, **124**, 2639
- van der Marel, R. P., & Kallivayalil, N. 2014, *ApJ*, **781**, 121
- Watson, L. C., Schinnerer, E., Martini, P., Böker, T., & Lisenfeld, U. 2011, *ApJS*, **194**, 36
- Wilcots, E. M., & Prescott, M. K. M. 2004, *AJ*, **127**, 1900
- Yozin, C., & Bekki, K. 2014, *MNRAS*, **439**, 1948
- Yurin, D., & Springel, V. 2014, *MNRAS*, **444**, 62
- Zaritsky, D. 2004, *ApJL*, **614**, L37
- Zaritsky, D., & Rix, H.-W. 1997, *ApJ*, **477**, 118
- Zaritsky, D., Salo, H., Laurikainen, E., et al. 2013, *ApJ*, **772**, 135
- Zhao, H., & Evans, N. W. 2000, *ApJL*, **545**, L35

⁵ www.astropy.org/

⁶ <http://trac.mystic.cacr.caltech.edu/project/pathos>



Tidally Induced Morphology of M33 in Hydrodynamical Simulations of Its Recent Interaction with M31

Marcin Semczuk¹ Ewa L. Łokas¹ , Jean-Baptiste Salomon^{1,2}, E. Athanassoula³ , and Elena D’Onghia^{4,5,6}

¹ Nicolaus Copernicus Astronomical Center, Polish Academy of Sciences, Bartłomieja 18, 00-716 Warsaw, Poland

² Institut UTINAM, CNRS UMR6213, Université Bourgogne Franche-Comté, OSU THETA, Observatoire de Besançon, BP 1615, F-25010 Besançon Cedex, France

³ Aix-Marseille Université, CNRS, LAM, Laboratoire d’Astrophysique de Marseille, F-13388 Marseille, France

⁴ Department of Astronomy, University of Wisconsin, 2535 Sterling Hall, 475 N. Charter Street, Madison, WI 53076, USA

⁵ Center for Computational Astrophysics, Flatiron Institute, 162 Fifth Avenue, New York, NY 10010, USA

Received 2018 April 12; revised 2018 June 26; accepted 2018 July 17; published 2018 August 29

Abstract

We present a hydrodynamical model of M33 and its recent interaction with M31. This scenario was previously proposed in the literature in order to explain the distorted gaseous and stellar disks of M33, as well as the increased star formation rate in both objects around 2 Gyr ago. We used an orbit integration scheme to find which estimate of the transverse velocity of M31 favors the interaction scenario more and then tried to reproduce it in our simulations. M33 was modeled as a stellar and gaseous disk embedded in a live dark matter halo, while M31 was approximated only with a live dark halo. In the simulations, the two galaxies passed each other with a pericenter distance of 37 kpc. Tides excited a two-armed spiral structure in the M33 disk, which is found to be the predominant spiral signal in the observed galaxy and has long been known as a feature easily induced by tidal interactions. We found that the gaseous warp produced by the interaction did not resemble enough the observed one, and we performed an additional simulation including the hot gas halo of M31 to show that this feature can be properly reproduced by tidal forces and ram pressure stripping acting simultaneously on the gaseous disk. In addition to the spiral arms, tidal forces produced a stellar stream similar to the one observed and triggered a star formation burst at radii similar to where it is observed.

Key words: galaxies: evolution – galaxies: individual (M33) – galaxies: interactions – galaxies: kinematics and dynamics – galaxies: structure – Local Group

1. Introduction

The Triangulum Galaxy (M33) is a late-type spiral and the third-largest galaxy in the Local Group (LG), behind the two more massive members of the LG, the Milky Way (MW) and the Andromeda Galaxy (M31). M31 and M33 form a pair that is rather separated from the MW, with their relative distance ~ 4 times smaller than their respective distances to the MW. Aside from their spatial proximity, which results in proximity on the sky, there are several other observational hints pointing toward the possibility that the galaxies are gravitationally bound and have interacted in the past.

1.1. Observational Evidence for the M33–M31 Interaction

The first morphological feature of M33 that might have been induced by the interaction is its gaseous warp. It was first found by Rogstad et al. (1976) and later, several works (Corbelli & Schneider 1997; Putman et al. 2009, hereafter P09; Corbelli et al. 2014, hereafter C14; Kam et al. 2017) confirmed that the HI disk of M33 extends farther than its stellar component and is strongly warped in the outer parts. This warp results in the continuous twist of the position angle (C14; Kam et al. 2017) and has a symmetric geometry, characteristic of tidally induced structures. However, the geometry of the warp of M33 is a little peculiar, because it is in the shape of the letter S, while the spiral arms, both in the stellar and the gaseous disk, have the reverse chirality, i.e., a Z-like shape. Initially, Rogstad et al. (1976) proposed that the origin of the warp could have been a primordial distortion of the disk, which has survived to

the present because the tilted rings would precess at different rates at different radii (Kahn & Woltjer 1959; Hunter & Toomre 1969). This scenario appeared more attractive than the interaction with M31, due to the angular separation between the galaxies, which was believed to be too large to produce sufficient tidal forces. However, a more recent study by P09 found that the gaseous features were very probably induced tidally by M31 in the past 1–3 Gyr. This finding was based on the orbit analysis that was constrained by the measurements of the radial velocities of M33 and M31 as well as the proper motion of M33 derived by Brunthaler et al. (2005).

While the vertical distortion of the gaseous disk of M33 has been known since the 1970s, the stellar disk was until very recently believed to be unperturbed in this dimension. McConnachie et al. (2009) reported finding a stellar structure extending northwest and south from the disk of M33. This feature stretches up to three times farther than the size of the disk and has an orientation similar to the HI warp. McConnachie et al. (2010) and Lewis et al. (2013) confirmed the alignment of the orientations; however, Lewis et al. (2013) also pointed out an offset between the two structures. The lack of a precise overlap of both features has been suggested to be due to the fact that the stellar component is only affected by tidal forces while the gas could also have experienced shocking and ram pressure stripping (RPS).

Both the gaseous warp and the stellar-stream-like distortion are features that strongly suggest some sort of past tidal interaction. Although they are not commonly found in spiral galaxies, M33 possesses another, more common morphological trait that may have been induced by tides, namely the dominant grand-design spiral structure. It is generally believed that M33

⁶ Vilas Associate Professor.

is a multi-armed spiral with a clear two-armed structure in the inner stellar disk (e.g., Humphreys & Sandage 1980; Newton 1980; Consider & Athanassoula 1988; Puerari 1993). It has been known for a long time that a grand-design spiral structure may be induced by tidal interactions. This view is supported by plenty of observational evidence on galaxies like M51, where one of its two spiral arms is pointing toward the companion flying by (Guntherdt et al. 2006). The scenario of triggering the two-armed spiral structure was also confirmed in several numerical simulations. It was shown that spiral arms in a disk galaxy may be induced either by a smaller companion passing by (e.g., Dobbs et al. 2010; Oh et al. 2015; D’Onghia et al. 2016; Pettitt et al. 2016) or during the orbital motion around a bigger perturber, even of the size of a galaxy cluster (Byrd & Valtonen 1990; Semczuk et al. 2017). In these simulations, the arms are triggered during the pericenter passages, and later, they dissolve and wind up over about 1–2 Gyr.

Besides two-fold spiral arms, the stellar disk of M33 is also known to host a small bar (Corbelli & Walterbos 2007; Hernández-López et al. 2009). While bars can be easily generated by global instabilities in cold disks (for a review on bar dynamics, see, e.g., Athanassoula 2013), it was shown that tidal interactions can also induce bar structures, e.g., in smaller companions perturbed by more massive hosts (Łokas et al. 2014, 2016; Gajda et al. 2017).

In addition to the morphological features present in both the gaseous and the stellar disk of M33, a gaseous bridge-like structure connecting M33 and M31 has been observed by several authors. First, Braun & Thilker (2004) reported finding an H I stream that seems to join M31 to M33. The presence of this structure was later confirmed by Lockman et al. (2012). Wolfe et al. (2013) found that about 50% of this structure is made of distinct clouds, while the rest is a diffuse component. While some authors, like Bekki (2008), argued that the H I bridge may have originated from an interaction between M33 and M31, Wolfe et al. (2013) objected, stating that the collapse timescale of these clouds (~ 400 Myr) is much shorter than the time since the hypothetical interaction (~ 1 –3 Gyr). More recently, observations of Wolfe et al. (2016) have cast even more doubt on the presence of the bridge by confirming that the majority of H I material in that region takes the form of discrete clouds.

The last argument supporting the interaction scenario arises from the analysis of the star formation histories (SFHs) of both galaxies. Bernard et al. (2012) obtained the SFH of M31 in the outer disk and reprocessed the fields studied by Barker et al. (2011) in M33. They found that a rapid increase in star formation rates (SFRs) took place in both M33 and M31 about 2 Gyr ago. Bernard et al. (2012) concluded that these bursts could be triggered by a close passage of the galaxies and that a similar increase is consistent with state-of-the-art simulations of galaxy interactions and mergers.

1.2. Previous Works

Despite recent progress in high-resolution hydrodynamical and N -body simulations of galaxies, not many authors have attempted to reproduce particular observed interacting systems. Among the most popular objects are M51 (e.g., Salo & Laurikainen 2000; Theis & Spinneker 2003; Dobbs et al. 2010), the Antennae galaxies (e.g., Teyssier et al. 2010; Renaud et al. 2015), the Cartwheel galaxy (e.g., Horellou &

Combes 2001; Renaud et al. 2018), and the Magellanic Clouds (Besla et al. 2012; D’Onghia & Fox 2016; Pardy et al. 2018). Interestingly, M33 was not a popular target, in spite of (or perhaps due to) its proximity and the wealth of observational data.

Inspired by the discovery of Braun & Thilker (2004), Bekki (2008) carried out simple test-particle simulations to verify whether the discovered bridge-like structure could possibly have originated from the interaction between M33 and M31. The outcome of this numerical experiment was in favor of this scenario, and he proposed that the interaction might have happened 4–8 Gyr ago. He also suggested that the H I warp of M33 might be fossil evidence of such a past interaction; however, the resolution of his simulation was not sufficient to study the detailed structure of the M33 disk.

The second attempt at modeling the M33–M31 interaction was motivated by the discovery of the extended stellar stream by McConnachie et al. (2009). In the very same paper, McConnachie et al. (2009) presented results of high-resolution N -body simulations of M33 passing near M31. Both galaxies were modeled as exponential disks with bulges, embedded in dark matter halos. The relative orbit had a pericenter of 53 kpc and tidal forces excited a warp in the M33 disk that wound up and in projection closely resembled the observed distortion.

The simulations of Bekki (2008) and McConnachie et al. (2009) were only constrained by the 3D velocity vector of M33, since the radial and transverse velocities were known only for this galaxy. Brunthaler et al. (2005) obtained proper motions of M33 by water maser observations. For M31, van der Marel & Guhathakurta (2008) estimated the global transverse velocity by analyzing the line-of-sight (LOS) kinematics of its satellites. This estimate, however, was not used by McConnachie et al. (2009) to constrain the mutual orbit. Later, Sohn et al. (2012) used long-time *Hubble Space Telescope* (HST) observations of three fields in M31 to obtain its proper motions. Their measurements were corrected by van der Marel et al. (2012b) for the internal kinematics of M31. The obtained transverse velocity of M31 was found to be 17 ± 17 km s $^{-1}$ and implied that M31 will merge with the MW in the future. This measurement also had implications for the possible past orbit between M31 and M33. Shaya & Tully (2013) used numerical action methods and integration backward in time to find the orbital history of the galaxies in the LG. They found that the results consistent with the measurements of the proper motions of M33 and M31 suggest that M33 is now at its closest approach to M31.

Recently, Patel et al. (2017b) used backward orbit integration and showed that assuming the transverse velocity of van der Marel et al. (2012b) yields orbits with an unlikely recent (~ 2 Gyr ago) and close (< 100 kpc) pericenter passage. However, the robustness of the measurements by van der Marel et al. (2012b); and specifically the corrections for the internal motions of M31 was recently questioned by Salomon et al. (2016). Since the astrophysical implications of the measurements of van der Marel et al. (2012b) were enormous, Salomon et al. (2016) separately estimated the velocity vector of M31 by modeling the galaxy and its satellites as a system with cosmologically motivated velocity dispersion and density profiles. The resulting radial velocity was consistent with the observed one, while the tangential component was surprisingly high, ~ 149 km s $^{-1}$. This conflicting result created the problem of which transverse

velocity to adopt for M31 if one wanted to model the orbital history of galaxies in the LG.

1.3. This Study

In this paper, we aim to show that the observationally constrained structural parameters of M33 and M31 combined with a relative orbit that is consistent with measurements of the observed velocities (one or the other in the case of M31) can reproduce the following traits of the interaction found in M33: the gaseous warp, stellar stream, two-armed spiral structure, and an increase in SFH. In order to reach this goal, we used high-resolution N -body/hydrodynamical simulations. The model presented here does not attempt to reproduce exactly the history of the interaction between both galaxies; rather, our aim was to show that combining observables with numerical methods can result in structures similar to the observed ones, which in the past were often assigned to the interaction scenario.

This paper is organized as follows. In Section 2, we present the orbit integration method that helped us to answer which of the measurements of the transverse velocity of M31 favors more the interaction scenario. In Section 3, we give the details of the simulations (initial conditions, numerical methods, and the adopted orbit) that were carried out in order to reproduce the observed M33. Section 4 describes the properties of the simulated galaxy and its similarities to the observed M33. Section 5 provides the discussion of our results, and Section 6 summarizes them.

2. Orbit Integration

To construct a model of the interaction between M33 and M31, one requires mass models of both galaxies and their mutual orbit. The orbit is constrained by the final relative position and velocity of the galaxies that can be derived from the observed sky coordinates, distances, LOS velocities, and proper motions. The positions on the sky of both galaxies are known very precisely. Measurements of distances and LOS velocities have been carried out by different authors (e.g., van der Marel & Guhathakurta 2008; Gieren et al. 2013 and references therein), and while errors can be smaller or bigger, they converge to similar values. The proper motions of M33 were only measured once by Brunthaler et al. (2005). The proper motions of M31 were derived by several authors, and some of the results are in conflict, which creates problems for attempts to model the relative orbit of the M31–M33 system.

The two most recent and conflicting results for the proper motions of M31 were obtained by van der Marel et al. (2012b) and Salomon et al. (2016). In order to verify which of the measurements better favors the scenario with a recent pericenter passage, we performed a semi-analytic orbit integration similar to the one presented, e.g., in Patel et al. (2017b). The adopted values of the relative 3D positions and velocities between the two galaxies are described in Appendix A. Computational details of the orbit integration and parameters we used are briefly outlined in Appendix B.

Our approach to finding which one of the two transverse velocity estimates favors more the interaction scenario consisted of three steps. In the first step, we integrated the relative orbit of the M33–M31 system backward in time for 5 Gyr, starting from the central values of the two sets of phase-space coordinates given by Equations (2) and (3) (hereafter

called the vdM12 set) and then those given by Equations (2) and (4) (hereafter called the S16 set). The orbit for the vdM12 set had no pericenter in this time period, and the current position was the closest approach. The orbit for the S16 set had a pericenter passage about 2 Gyr ago, with a pericentric distance >100 kpc. Neither of these orbits was satisfying, i.e., neither had the pericenter <100 kpc to presumably reproduce the observed morphology of M33, so we performed additional orbit shooting.

In the second step, we integrated multiple orbits forward in time, starting from the modified values obtained in the first step for the vdM12 and S16 sets. The modification was made by varying the magnitude and the direction of the initial velocity vector. By changing these parameters (the magnification factor and the rotation angle), we obtained a grid of possible orbits. From the calculated sample of orbits, we selected those that had a pericenter passage closer than 100 kpc and checked how close they lie to the sets vdM12 and S16 after the pericenter passage. The proximity was defined in terms of the χ^2 statistics, and lower values were found for the S16 set. We used the orbit found in this way in the following simulations; however, it turned out to be slightly divergent from the one obtained by the orbit integration. The differences appeared after including hydrodynamics and increasing the resolution of our simulations. The final orbit used in our fiducial model is then a result of many iterative corrections and is discussed in greater detail in Section 3.2.

One may argue that the method of selecting the orbit that favors the interaction scenario used in the second step is incomplete since there is no guarantee that the range of initial magnitudes and directions of the velocity vector can reproduce all possible values of the observed positions and velocities allowed by the observational errors. Because of that, in the third step, we tested our calculations with a simpler and more straightforward method and discussed its results instead of the statistics of χ^2 obtained in the second step. The method is similar to the one presented in P09, and it consists of integrating orbits backward in time starting from values randomly selected from the range allowed by the vdM12 and S16 sets. We randomly selected 15,000 positions and velocity vectors for both vdM12 and S16 from the range enclosed by the 1σ error bars and integrated orbits backward in time for 5 Gyr.

Figure 1 shows the distributions of the pericenter distances and lookback times when the pericenters took place for both initial sets of values. What we call the pericentric distances here are in fact just distances at the closest approach. We did not integrate those orbits forward in time, or further backward, to really tell if it is a true pericenter or if the pericenter is about to take place (or took place more than 5 Gyr ago). The analysis of Figure 1 and especially of the horizontal histograms confirms our first findings that the S16 set favors the interaction scenario more strongly than vdM12. Around 20% of the orbits starting from vdM12 values are now at the closest approach, while the majority of the rest had their closest approach more than 2 Gyr ago with only one point having a pericenter recently (<2 Gyr ago) and closer than 100 kpc. Only around 0.5% of the orbits starting from S16 are now at the closest approach, while 82% have had a recent pericenter, i.e., less than 2 Gyr ago but not at the present time. Of all pericentric distances for S16, 65% are smaller than 100 kpc. Therefore, we conclude that the measurements of proper motions of M31 made by

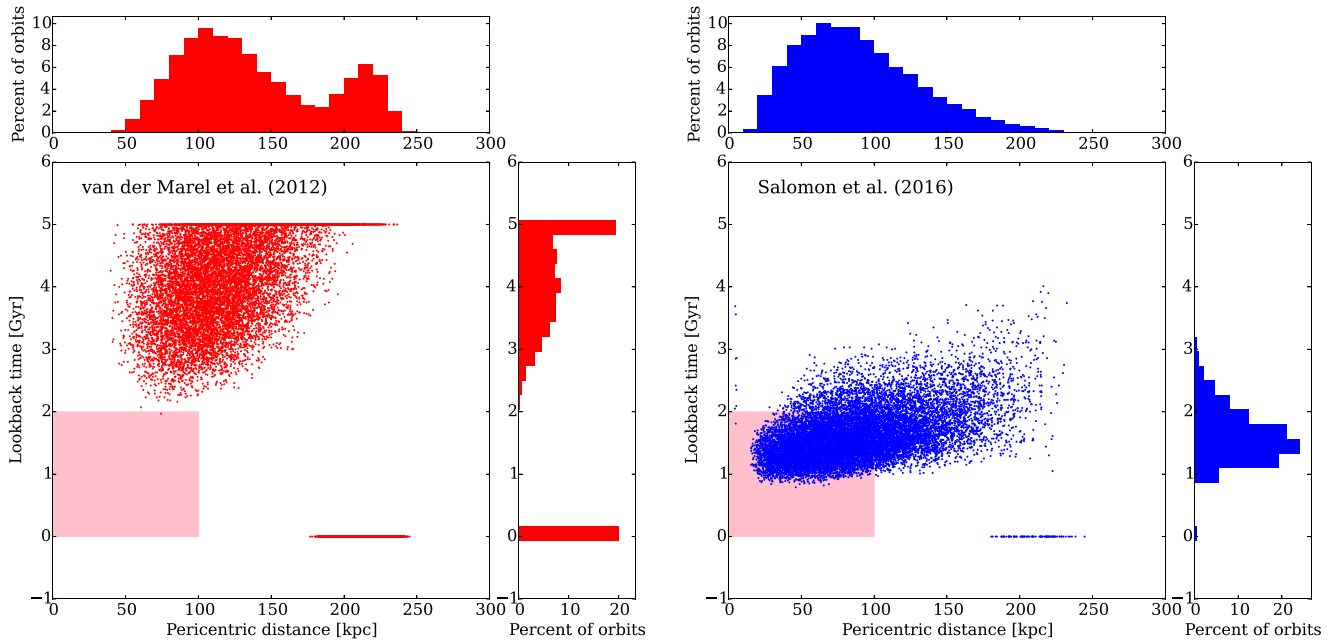


Figure 1. Distributions of pericenter distances and lookback times for orbits obtained via semi-analytic orbit integration backward in time. The left panel shows the distribution for 15,000 orbits that started from randomly selected values from within the error bars of the relative position and velocity calculated by adopting the velocity of M31 derived by van der Marel et al. (2012b; Equations (1) and (2)). The right panel shows the same results but after adopting values for M31 derived by Salomon et al. (2016; Equations (1) and (3)). The pink square in both plots indicates the area of values ($r_{\text{peri}} < 100$ kpc and $t_{\text{peri}} < 2$ Gyr), suggested by Putman et al. (2009) and McConnachie et al. (2009), that would reproduce the observed morphological features of M33.

Salomon et al. (2016) favor the interaction scenario more than do the results of van der Marel et al. (2012b). In the rest of this paper, we will aim to reproduce in simulations the S16 set of the relative position and velocity between M33 and M31.

This finding is not very surprising, since the error estimates derived by Salomon et al. (2016) are about twice as large as those of van der Marel et al. (2012b) and naturally allow for more orbital configurations. Our findings are also partially in agreement with the results of Patel et al. (2017a, 2017b), where one of the conclusions was that the interaction scenario is not very plausible once one adopts the orbital values obtained by van der Marel et al. (2012b).

3. The Simulations

3.1. Initial Conditions for the Two Individual Galaxies

Our aim when creating models of both galaxies is to reproduce their observationally derived rotation curves (C14 and Corbelli et al. 2010). This task is not straightforward since the interaction between the two galaxies changes their structural parameters. This paper is devoted to the investigation of the changes that M33 might have undergone due to such a hypothetical scenario, and because of that, we approximate M31 only as a Navarro–Frenk–White (NFW) dark matter halo with the virial mass $M_{\text{M31}} = 2 \times 10^{12} M_{\odot}$ and concentration $c_{\text{M31}} = 28$. These parameters were chosen to reproduce the rotation curve derived by Corbelli et al. (2010) only with the dark matter component (see the upper panel of Figure 2). The baryonic content of M31 contributes more to the rotation curve than the dark matter in the inner 10–15 kpc (see Figure 14 in Corbelli et al. 2010), and therefore our adopted parameters exceed the values of the parameters of the halo obtained by Corbelli et al. (2010), where the disk and the bulge were included in the modeling of the mass distribution. Our model of M31 consisted of 2×10^5 particles.

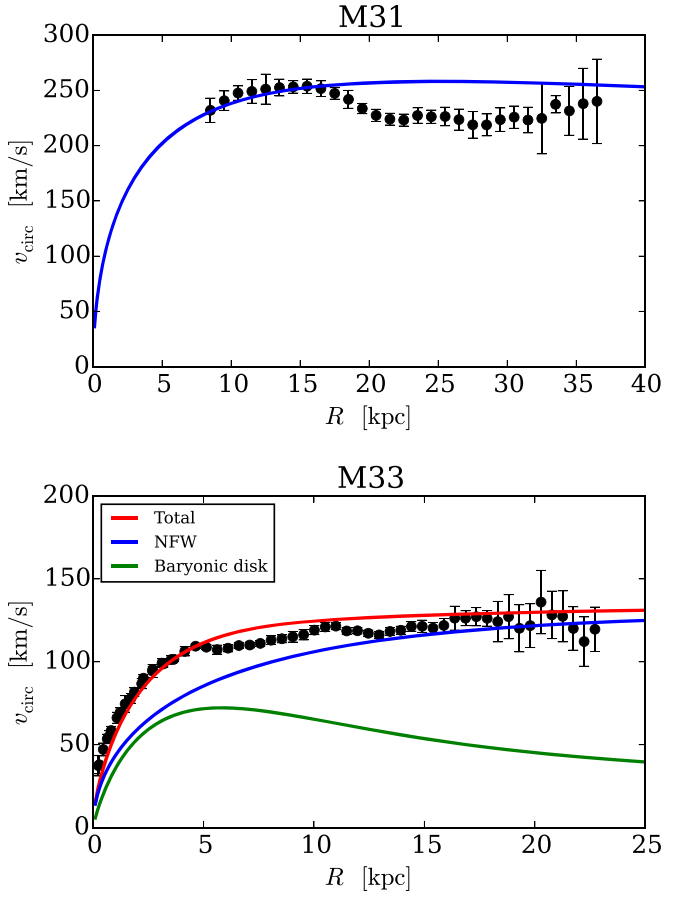


Figure 2. Upper panel: the rotation curve of the initial model of M31. The observed rotation curve (Corbelli et al. 2010) is represented by black dots. Lower panel: the rotation curve of the initial model of M33, after evolution in isolation for 10 Gyr without star formation, feedback, and cooling. The observed rotation curve (Corbelli et al. 2014) is represented by black dots.

Including the disk of M31 in the simulation would be an interesting possibility given the plethora of substructure surrounding this galaxy (e.g., Lewis et al. 2013). However, it would also make it more difficult to match the inclinations of the two galaxies at the same time. The physical implication of not including the disk of M31 is the spherical symmetry of its potential. The axisymmetric disk component would slightly bend the relative orbit between M33 and M31 out of the initial plane, and this effect would have to be taken into account during iterative corrections of the orbit.

Our model of M33 is more detailed and consists of three components: a dark matter halo and stellar and gaseous disks. The initial dark matter halo had an NFW profile with $M_{\text{M33}} = 5.2 \times 10^{11} M_{\odot}$ and a concentration $c_{\text{M33}} = 11$. We increased the value of the halo mass with respect to what was estimated by C14 to take into account the mass loss that will occur during the tidal stripping in the simulations.

The best estimate of the stellar mass of M33 provided by C14 is $4.8 \times 10^9 M_{\odot}$. The combined gas mass of H I, H₂, and helium is estimated to be $2.43 \times 10^9 M_{\odot}$ (C14). These values summed up give a total baryonic mass of $7.23 \times 10^9 M_{\odot}$, with the stars contributing 66% and the gas 34%. The surface density profiles of stars and baryons in total provided by C14 have a break at ~ 10 kpc. Because of this break, fitting one exponential stellar disk combined with the halo parameters and the gaseous disk will not reproduce the given rotation curve to a satisfactory degree. One must divide the stellar disk into two components with different slopes in order to have enough rotation in both the central and outer parts. In our simulations, however, we decided to start with the simplest model and keep the number of parameters of the problem as small as possible. In order to preserve this simplicity and still reproduce the rotation curve in the inner parts (and both inner and outer ones at the end of simulation, after tidal stripping of the halo), we adopt the initial baryonic disk mass to be $M_B = 8.49 \times 10^9 M_{\odot}$ with a scale length $R_B = 2.5$ kpc and scale height $z_B = R_B/5 = 0.5$ kpc.

The initial conditions for the described disk, which consisted of 10^6 particles, were generated using the procedures provided by Widrow & Dubinski (2005) and Widrow et al. (2008). This method of generating initial conditions is suited for stellar disks but not gaseous ones. We therefore divided this initial baryonic disk into stellar (35%) and gaseous (65%) particles and evolved it in isolation so that the gaseous disk stabilized (similarly to Fouquet et al. 2017). The simulation in isolation was carried out with the GADGET-2 N -body/smoothed particle hydrodynamics (SPH) code (Springel et al. 2001; Springel 2005). The galaxy was evolved for 10 Gyr with the initial temperature set to 5000 K. The subgrid processes were turned off, because the purpose of this run was to avoid gas instabilities and produce initial conditions for the fiducial simulations, rather than to study the evolution of the galaxy in isolation. During these 10 Gyr, the gaseous disk thickened and stabilized. It became pressure-supported instead of being supported by velocity dispersion, as the stellar one is. The initial stellar and gas fractions (35% and 65%) that were kept constant in this run were adjusted to reach the values inferred from C14 (66% and 34%) after the evolution with star formation during the fiducial simulation. This tuning was done via a trial-and-error method by running simulations with subgrid physics and iteratively checking which initial values lead to the final values close to the desired ones.

Table 1
Parameters of Initial Conditions for Simulated Galaxies

Components	Properties	Values
M33 dark matter halo	Virial mass	$5.2 \times 10^{11} M_{\odot}$
	Concentration	11
	Number of particles	10^6
M33 baryonic disk	Mass	$8.49 \times 10^9 M_{\odot}$
	Scale length	2.5 kpc
	Scale height	0.5 kpc
M33 gaseous disk	Number of particles	6.5×10^5
M33 stellar disk	Number of particles	3.5×10^5
M31 dark matter halo	Virial mass	$2.0 \times 10^{12} M_{\odot}$
	Concentration	28
	Number of particles	2×10^5

The initial surface density profile of the gas follows an exponential distribution, with the same slope as the stellar disk. In general, the observed gas disk profiles are flatter in the center and do not follow an exponential law, which is also the case for M33 (C14). This discrepancy is an artifact of the simple method of generating the initial conditions that we used; nevertheless, it has little influence on the model, since as shown in Section 4.1 the gas profile in the center will be significantly lowered and will mimic the observed one well, due to the conversion of some of the gas into stars.

The initial rotation curve plotted in the lower panel of Figure 2 seems to match the data in the inner parts, while in the outer parts it overproduces the rotation. Note, however, that these values will be lowered as a result of tidal stripping of the dark matter halo. All of the parameters of the initial conditions for both galaxies are summarized in Table 1.

3.2. The Orbit

The orbits derived by the orbit integration scheme described in Section 2 happen to diverge from the orbits in the N -body simulations with the same initial parameters and mass profiles. This divergence is due to the fact that the orbit integration does not include tidal stripping and the resulting mass loss. In addition, the orbits found in N -body simulations diverge from the orbits in SPH simulations, and those differ among each other for runs with different particle numbers. All of these differences are of the order of a few tens of kiloparsecs (up to ~ 30 kpc), which makes it more difficult to accurately fit the adopted observed relative position and velocity (S16). It also changes the pericentric distance (by ~ 10 kpc), which can affect the tidally induced morphological features. Because of these numerical uncertainties, the orbit used in our fiducial simulation is not exactly the same as the one derived in Section 2, but instead it is a result of multiple iterative corrections that were made to best fit the morphological features (mostly the gaseous warp) and to end up as close as possible to the S16 set.

We applied a similar strategy to find the initial rotational angular momentum (spin) of our model of M33. The direction of this vector is the same as the vector normal to the disk's plane, which can be derived from the observed inclination and the position angle of M33. The first runs of our simulations were performed with the observationally derived values; we found, however, that this vector was changing during the orbital evolution. Therefore, we iteratively corrected it, so that at the present time it reproduces reasonably well the observed

Table 2
Initial Orbital Parameters and Inclination of M33

Vector	X	Y	Z	Unit
Position	-278.1	326.7	44.5	kpc
Velocity	56.5	-6.5	32.8	km s^{-1}
Normalized spin	0.048	0.998	-0.038	...

position angle and inclination as well as the observed morphology (we focused mostly on the gaseous warp).

The initial orientation of the disk of M33 with respect to its orbit around M31 can be parametrized by two angles: α , the angle between the spin of the disk and the orbital angular momentum, and β , the angle between the spin and the direction of the velocity of M33 on its orbit. We started with β derived from the normal vector from observations and varied it by $\pm 45^\circ$ to see whether both directions in the parameter space made the gaseous warp flatter. Hence, we assumed that for this parameter we are approximately in the best place. For α , we tried eight different values from the range between $\sim 15^\circ$ and $\sim 80^\circ$. Values close to the prograde case, $\alpha = 0^\circ$, keep the tidal disturbance within the two dimensions of the plane of the disk, and the warp-like distortions are not present. Crossing $\alpha = 90^\circ$ and approaching the retrograde case, $\alpha = 180^\circ$, decrease the effect of the tidal perturbation of the disk and make it hard to generate spiral arms (D’Onghia et al. 2009, 2010; Łokas et al. 2015). The final value of α turned out to lie only a few degrees away from what was derived from the observations, and we found that as long as it is not too close to 0° , it has very little influence on the 3D appearance of the galaxy. We also found that rather than changing the inclination, other parameters were much more influential in shaping the warp, namely the magnitude of the tidal perturbation (parametrized either by the pericenter distance or by the mass profile of M31) and the inclusion of the hot gas halo of M31, which is discussed later.

The values of the initial position, velocity, and spin that we used in our fiducial simulation are summarized in Table 2. M31 was placed at the center of the coordinate system, and its initial velocity was $(0, 0, 0) \text{ km s}^{-1}$. The upper panel of Figure 3 shows how the relative distance and velocity between M33 and M31 was changing in time for the adopted orbit. The orbit has a pericenter of 37 kpc 2.7 Gyr after the beginning of the simulation. The pericenter distance is larger than the sum of the sizes of the disks of both galaxies, hence the approximation of the M31 potential as a pure dark matter halo does not imply that we ignore additional effects resulting from the crossing of the disks. We note that dynamical friction decreased the apocenter of the orbit by a factor of roughly 2.8, from 432 to 151 kpc after the pericenter passage.

The lower panel of Figure 3 shows the shape of the relative orbit in its plane. It is worth noting that the position of M31 was changing significantly due to the attraction from M33 (~ 100 kpc), which is not so surprising given that the adopted masses result in a mass ratio of M33 to M31 as large as $\sim 26\%$. The orbit presented here was centered on M31 at each time step to make the image more clear.

3.3. The Code and the Fiducial Run

The fiducial simulation presented in this paper was carried out with a modified version of the GADGET-2 N -body/SPH code

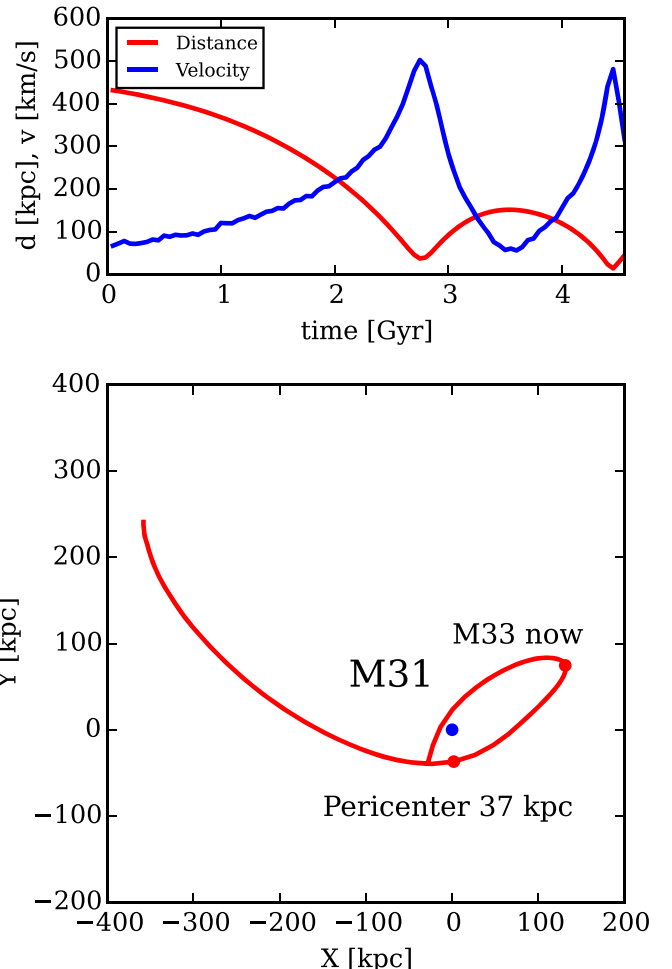


Figure 3. Upper panel: the time dependence of the relative distance d and velocity v between M33 and M31 for the adopted orbit. Lower panel: the shape of the relative orbit between M33 and M31 in the orbital plane. At each time step, it was centered on M31.

(Springel et al. 2001; Springel 2005) that includes star formation and feedback and cooling processes added as described in Hammer et al. (2010) and Wang et al. (2012). The subgrid physics was implemented according to the recipes given by Cox et al. (2006). We chose to adopt the values of the parameters as advised by Cox et al. (2006), namely a star formation efficiency of 0.03, a feedback index of 2, a density threshold for star formation of $0.0171 M_\odot \text{ pc}^{-3}$, and a timescale of feedback thermalization of 8.3 Myr. Instead of tuning the subgrid parameters listed above, we were changing the initial gas fraction to match the observed one at the present time. If one intended to reproduce the simulations presented here with a code using a different subgrid model, this value would have to be tuned again to conform with the different subgrid model, as it is generally believed that subgrid schemes can change the outcome of simulations very significantly (e.g., Arthur et al. 2017).

The implementation of the subgrid physics using the prescriptions of Cox et al. (2006) includes cooling processes described by the procedures given by Katz et al. (1996). These procedures result in assigning every gas particle the neutral hydrogen mass fraction. We stress here that throughout this paper, we will use the name “gas” for gas particles in general while the term “neutral hydrogen” or H I + H₂ will be used for

masses of gas particles reduced by this fraction given by the cooling procedures in order to match better the observations that mostly probe the H I content of M33.

We followed the evolution of the system for 4.5 Gyr with outputs saved every 0.05 Gyr. We adopted the softening lengths of 0.09 kpc for the stellar and gaseous particles, 0.63 kpc for the dark matter of M33, and 10 kpc for the dark matter of M31.

3.4. The RPS Experiment

As described below, we managed to reproduce several features of M33 in the fiducial simulations. We found however that one of these features, namely the gaseous warp, cannot be reproduced to a satisfying degree of similarity (especially at larger radii) by tidal effects alone. In order to argue that the RPS originating from the hot gas halo of M31 would significantly improve the resemblance, we performed simulations with lower resolution that included the hot gas halo of M31. The existence of the circumgalactic medium around M31 was demonstrated by Lehner et al. (2015); however, there are no strong observational constraints on the mass of the hot gas. Other galaxies are believed to have hot gas halo masses roughly 100 times smaller than their dark matter masses (Miller & Bregman 2015). We started the modeling of the hot gas halo with the mass value close to this estimate; however, the final adopted mass was smaller than this, as a result of tuning the effect of RPS to obtain the most similar gaseous warp.

In the simulation including the RPS, M31 was modeled as a Hernquist (Hernquist 1990) dark matter and hot gas halo. Parameters of the dark matter component were fitted to reproduce the NFW profile discussed in Section 3.1 and took the values of $2 \times 10^{12} M_{\odot}$ for the mass and 41 kpc for the scale radius. The hot gas halo had the same scale radius and the mass of $3 \times 10^9 M_{\odot}$. The dark matter halo consisted of 2×10^5 particles with the softening length of 10 kpc, and the gas halo was made of 70,630 particles with the softening of 0.2 kpc. Initial conditions for M31 for this simulation were generated using the CLUSTEP code⁷ (Ruggiero & Lima Neto 2017). Initial conditions for M33 were generated in the same manner as described in Section 3.1 with very similar parameters, except for the particle numbers and softening lengths. Particle numbers were 2×10^5 for dark matter, 126,000 for the gas, and 74,000 for stars, while softenings were 1.4 kpc, 0.2 kpc, and 0.2 kpc, respectively.

4. Properties of the Simulated Galaxy

The initial model of the M33 galaxy was transformed during the simulated time by both the subgrid physics (star formation, cooling, and feedback) and tidal interactions with the M31-like dark matter halo. The most important morphological features have been induced by the tidal interaction with M31 during the pericenter passage. To verify this, we carried out simulations with the same initial conditions for M33 but in isolation for 4.5 Gyr. A short discussion of this case is included in the appendix.

4.1. General Properties

Star formation converts $2.61 \times 10^9 M_{\odot}$ of gas mass into stars (hereafter called young stars, i.e., those stars that were

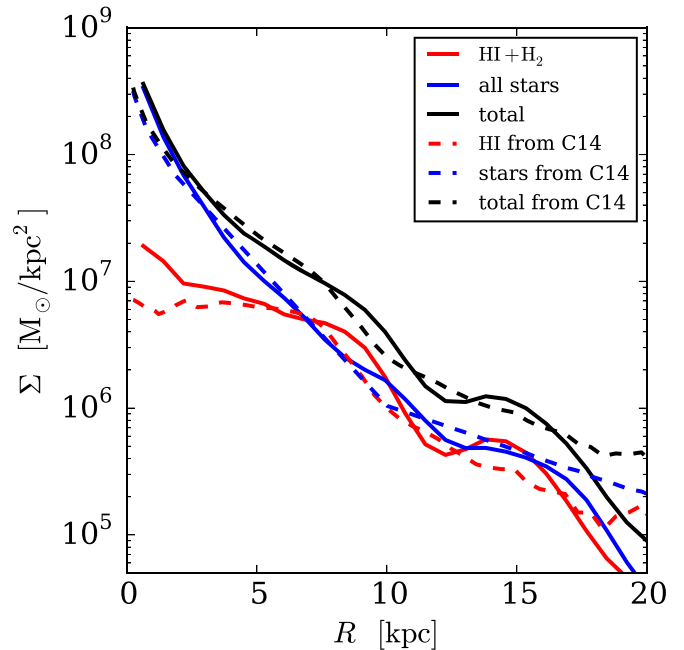


Figure 4. Surface density profiles for stars, neutral hydrogen, and baryons in total in our model of M33 at the time of the best match, compared with density profiles for stars, H I, and baryons from C14.

born after the beginning of the simulation, unlike the old stars, which were present in the initial conditions), which resulted in a total stellar mass of $M_* = 5.59 \times 10^9 M_{\odot}$ (at the time of the best match; the selection of this time is explained in Section 4.2). This mass contributes 66% of the baryonic mass, which is the ratio we were aiming to obtain, consistent with the findings of C14.

The star formation created a central plateau in the surface density profile of the gas, which is also seen in observations (C14). It is clearly visible in Figure 4, where we compare the obtained surface density profiles for stars, hydrogen, and baryons in total with the observationally measured profiles given by C14. We find that the simulated profiles are in reasonably good agreement with the observed ones. We reproduced the previously mentioned gaseous “core” and also approximated the slopes of the stellar and total baryonic distributions.

Tidal stripping does not strongly affect the baryonic mass of M33; however, a significant fraction of the dark matter mass was stripped. We fitted the NFW profile to the dark matter density distribution at the time of the best match and obtained a mass of $M_{\text{vir}} = 4 \times 10^{11} M_{\odot}$ and concentration $c = 10.5$. These values are within 1σ from the best-fit model of C14, and the mass is $\sim 77\%$ of the initial halo mass.

The rotation curve of M33 at the time of the best match is presented in Figure 5. This curve was calculated directly from the sum of forces from the particles in simulations. We note that the initial curve presented in Figure 2 was calculated using analytical formulae and was plotted only to show what we aim to reproduce. The obtained final rotation curve exceeds the observed data by tens of km s^{-1} in the inner ~ 3 kpc. This is due to the bar formation in this region, which affects the potential of the galaxy. In the outer parts, the simulated curve falls slightly under the observed one, which is a result of the tidal stripping of dark matter. However, despite these discrepancies on both ends, we find that in general the

⁷ <https://github.com/ruggiero/clustep>

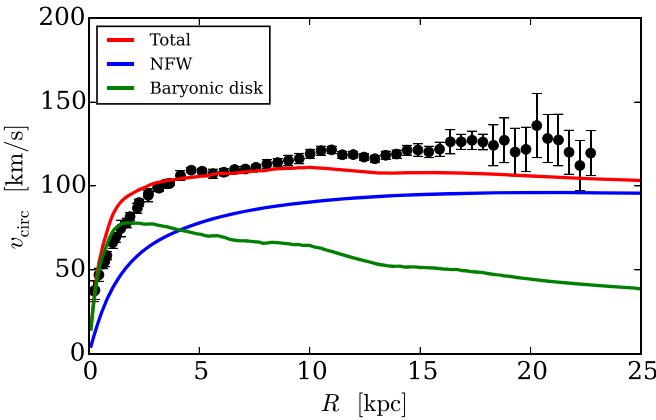


Figure 5. Rotation curve of our model of M33 at the time of the best match compared with the observed rotation curve provided by C14 (black dots).

simulated curve is a reasonable approximation of M33, being flat at around 100 km s^{-1} throughout the majority of radii. The resemblance of the curve to the observed one is better when the bar is excluded from the analysis and the disk component is calculated via the thin disk approximation from the fit to the surface density profile that excludes the steep inner part originating from the bar.

The tidal interaction during the pericenter passage induced spiral arms and a warp in both the gaseous and the stellar disk. These features survived for 0.75 Gyr after the pericenter and are present at the time of the best match (see Figure 6). The two-armed, grand-design spiral structure characteristic of tidal encounters is present in the gas, as well as the old and young stars. The off-planar tidal distortion (the warp) is mostly visible in the gaseous disk and the old stellar disk. This is due to the fact that the new stars are born in the inner region of the galaxy and the disk that they create is too small to exhibit a similar disturbance. The young stellar disk forms a small bar, which is also present in the observed M33 (e.g., Corbelli & Walterbos 2007; Hernández-López et al. 2009). However, as discussed in Section 4.5, the bar is not a tidal feature, and it also forms in isolation. Rather, the origin of the bar is related to the fact that the young stellar disk formed from the gas by star formation is not stable against bar formation. As shown in Athanassoula et al. (2013), this process can be weakened by increasing the gas fraction of the galaxy; however, in our case, the gas fraction is constrained by observations and subgrid physics.

4.2. The Warped Gaseous Disk

Figure 6 clearly demonstrates that both the gaseous and stellar disk have been warped by the tidal interaction. McConnachie et al. (2009) showed using N -body simulations that exciting such a distortion with similar parameters of M33 and M31 is possible. Their model, however, was not constrained by the proper motions of M31 and did not include gas physics. In this subsection, we briefly describe how we found the best orbital epoch and the viewing position that would result in the geometry of the warped disk similar to the observed one, and we compare our simulated images with those obtained by radio observations.

In order to find the projection and the orbital epoch that will result in a neutral hydrogen map resembling best the observed one, we visually inspected images of the rotated gas disk of

M33. The rotations were constrained by the demand for the relative 3D position and velocity of M31 with respect to M33 to be consistent within 2σ with the values of adopted Equations (2) and (4) (reversed, because Equations (2) and (4) are the relative coordinates of M33 with respect to M31 and here we look at the system from the perspective of M33). Using this procedure, we found the time of the best match to be 0.75 Gyr after the pericenter, which is 3.45 Gyr since the beginning of the simulation and just 0.05 Gyr before the apocenter. The relative position and velocity of M31 in the reference frame corresponding to the best-match projection at this time are $X_{\text{rel},M31} = (56.1, 91.5, 106.2) \text{ kpc}$ and $V_{\text{rel},M31} = (7.1, -38.8, 41.1) \text{ km s}^{-1}$. One out of six of these coordinates is 1.75σ away from the adopted values. Another one lies within 1.25σ and the remaining four are within 1σ .

The neutral hydrogen density map for the best-matching time and projection from the fiducial simulation is presented in the middle panel of Figure 7 (coordinates (ξ, η) are distances in R.A. and decl. from the center of M33). The upper panel of the same figure shows the H I map published by P09. By comparing both images, we find that tidal interactions managed to only reproduce the inner warp of the gas disk, i.e., features marked 1 and 2 in red in both maps. At larger radii in the simulated image, strong spiral/tidal extensions are the most eye-catching feature, while in observations this is not the case. We identify several substructures in the image of P09 that slightly resemble the spiral features in the simulated image (marked 3–6); however, in observations they are merely composed of one or two differently shaped contours, while in the image from simulations they are the dominating signal at these radii. Another discrepancy is that in the image from the fiducial simulation, the gas structure is more or less symmetric, while in the P09 image there seems to be more gas northwest from the galaxy. Also, the northern part of the warp, marked 1, is longer than its southern counterpart, 2. This asymmetry in the observed gas is pointing toward M31 on the sky, and this coincidence motivated us to investigate whether RPS from the hot gas halo of M31 may improve the simulated image.

The best-matching map from the simulations with RPS (found in the same way as for the fiducial simulation) is presented in the lower panel of Figure 7. Strong spiral/tidal extensions present in the fiducial model (3 and 6) were adequately weakened by RPS, and the dominating signal is coming from the S-oriented warp. The resemblance to the observations is still far from perfect (i.e., the galaxy is too elongated in simulations in comparison with the more flattened distribution in observations), but qualitatively, the S-shaped structure is similar to the observed one, with the inner spiral arms having the reversed Z-chirality. In the RPS image, there is also too much gas at the lowest density, located southeast from the disk. We suspect that this material (and maybe other discrepancies) may arise due to the limitations of the SPH scheme used in the code to mimic the hydrodynamics of the gas. It is well known that SPH codes fail the blob test (Agertz et al. 2007; Hopkins 2015) and thus underestimate the RPS of the cold gas and its mixing with the hot component. Because of these numerical problems, we decided not to explore the RPS experiment in greater detail, since the physics of this process would not be properly modeled anyway, while the other M33 features can be reproduced simply with simulations of tidal evolution. The asymmetry of the neutral hydrogen in the RPS image at first sight seems to be reversed

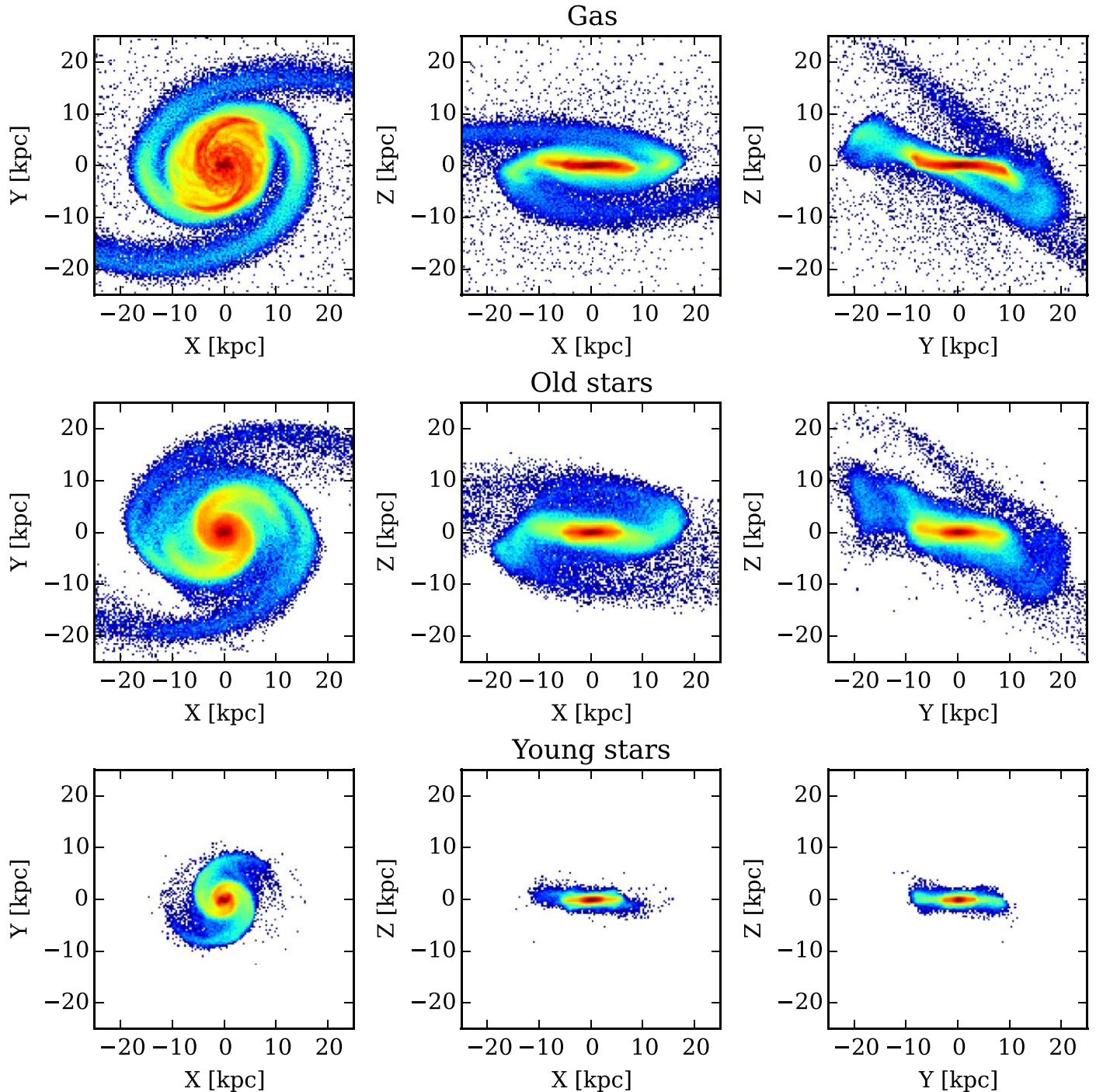


Figure 6. Surface density distributions seen from three different directions for the gas and—the old and young stellar particles for the simulated M33 at the time of the best match.

with respect to the observed asymmetry that motivated us to perform that experiment; however, it is the case only for the lowest density material. If we focus on the higher density, e.g., the fourth or fifth contour, where the gas physics is better resolved, then the asymmetry is reproduced and the gas stretches up to 1° north, while in the south it only reaches $\sim 0^\circ.6$ – $0^\circ.7$.

Corbelli & Schneider (1997), C14, and Kam et al. (2017) all reported that the gaseous warp quantitatively manifests itself in the continuous change of the position angle of the disk with increasing radius. The upper panel of Figure 8 presents the

radial dependence of the position angle obtained from images based on simulations and the comparison with the results from C14. The lines from the simulations were obtained by ellipse-fitting to column density distributions. The curves from both simulations exhibit a drop in values, of the order of 30° , with the one from the fiducial simulations being more important and resembling more the observed curve. The drop from the RPS case is not as big, about 20° , and corresponds well with the impression given by the map in Figure 7, i.e., that the overall shape of M33 is more elongated and the shift is milder than in the observations.

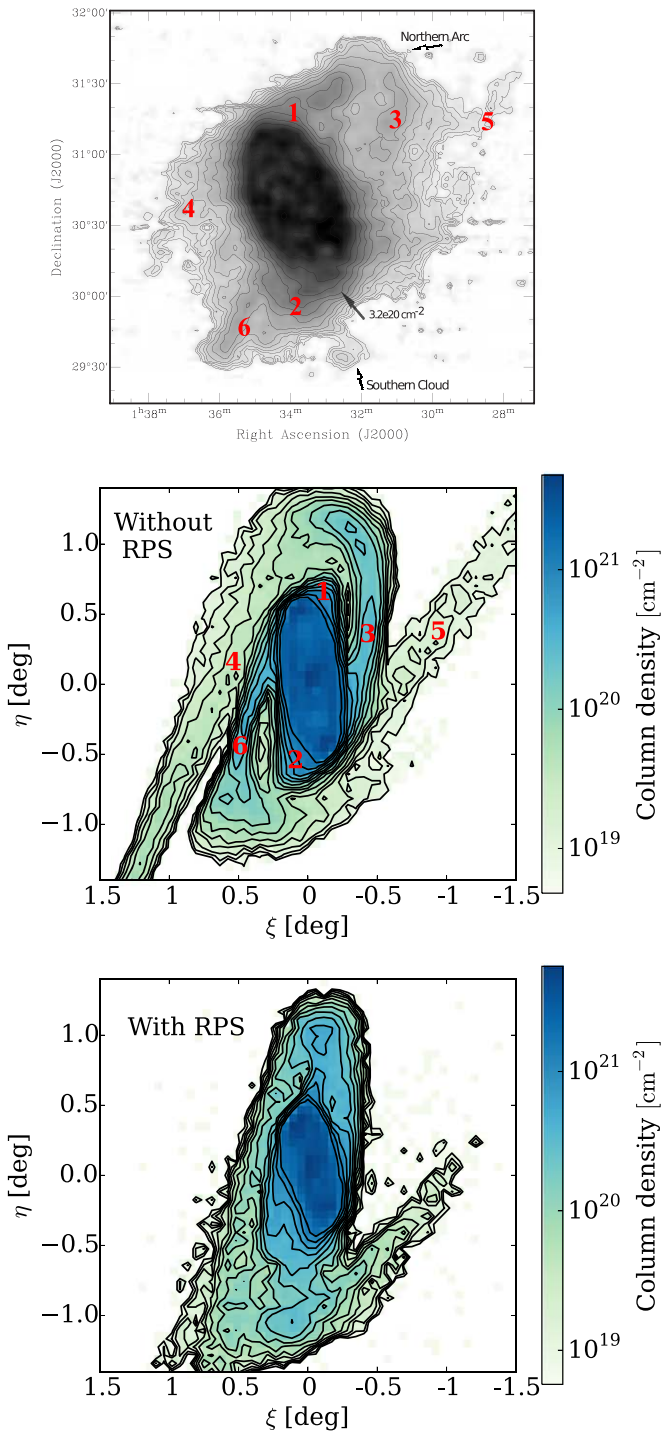


Figure 7. Upper panel: the H I column density map of M33 published by P09 (© AAS. Reproduced with permission). Middle panel: best-matching neutral hydrogen column density map from our fiducial simulations. The isodensity contours were plotted at the same levels as in P09. The red numbers mark the tidally induced features that resemble the corresponding features found in the image of P09. Lower panel: best-matching neutral hydrogen column density map from simulations that included RPS from the hot gas halo of M31. The inclusion of RPS seems to be necessary to weaken the strong tidal arms (3–6) that are almost invisible in the observed galaxy.

Supplementary quantitative information about the warp is given by the radial dependence of the inclination presented in the lower panel of Figure 8. The curves from the simulations show more structure than the ones obtained by C14. This is due to the fact that the extended gaseous features are less regular in

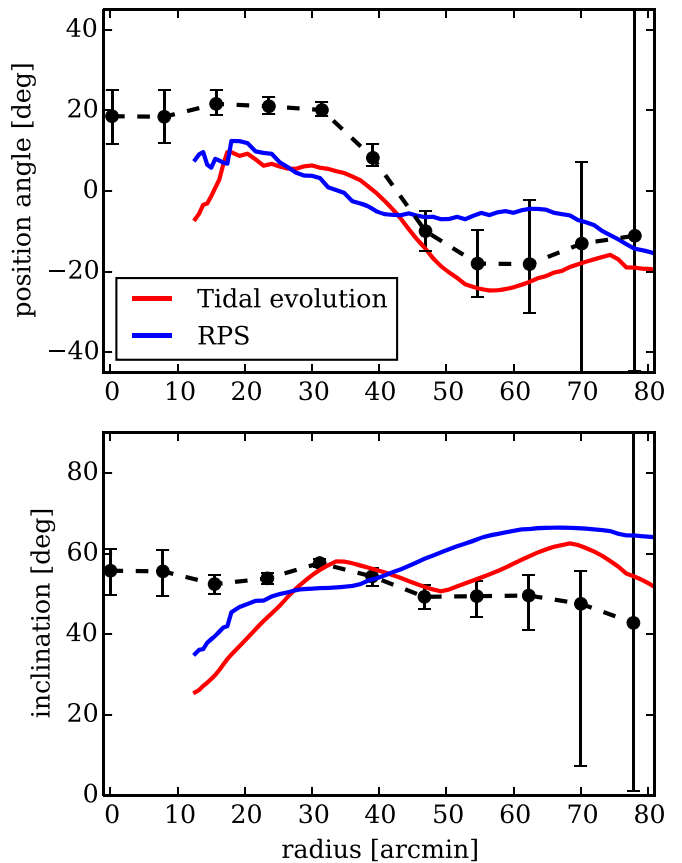


Figure 8. Upper panel: the radial dependence of the position angle obtained for the best-matching neutral hydrogen density map from the fiducial simulation (red line) and the RPS experiment (blue line) in comparison with the measurements from C14 (black points with error bars). Lower panel: the radial dependence of the inclination for the same cases as in the upper panel.

the simulations than in observations. Contrary to the visual impression, values from the simulations lie relatively close to the observed ones. This coincidence is probably just the result of a very simple method of deriving the inclination that we applied, and a bigger discrepancy would be seen if we have fitted a tilted ring model as in C14. Our models, however, are not very precise and do not require such sophisticated tools to analyze them; with the ellipse-fitting, we just wanted to show that both the inclination and the position angle have approximately similar values and radial dependence.

The warp of the M33 gaseous disk manifests itself also in the kinematics of the gas. Figure 9 presents the comparison between the kinematic map published by C14 and the one obtained from our fiducial simulation at the time and the projection of the best match. The simulated image reproduces reasonably well the observed one, and we find that the distortion of the disk is clearly visible in the twist of the zero-velocity line, as was also found by other authors (e.g., Kam et al. 2017). The image from fiducial simulations has a much thinner outline than the observed one, which is the result of the previously mentioned offset between the observed inclination and the one in the best-match projection. The best resemblance between the images is seen when one follows the lines that separate cyan from blue and red from yellow. These clearly show where the disk ends and tidal features start to be visible. For example, the tidal arm marked as 3 in Figure 7 is seen in the simulated kinematic map as a red arc southwest of the main

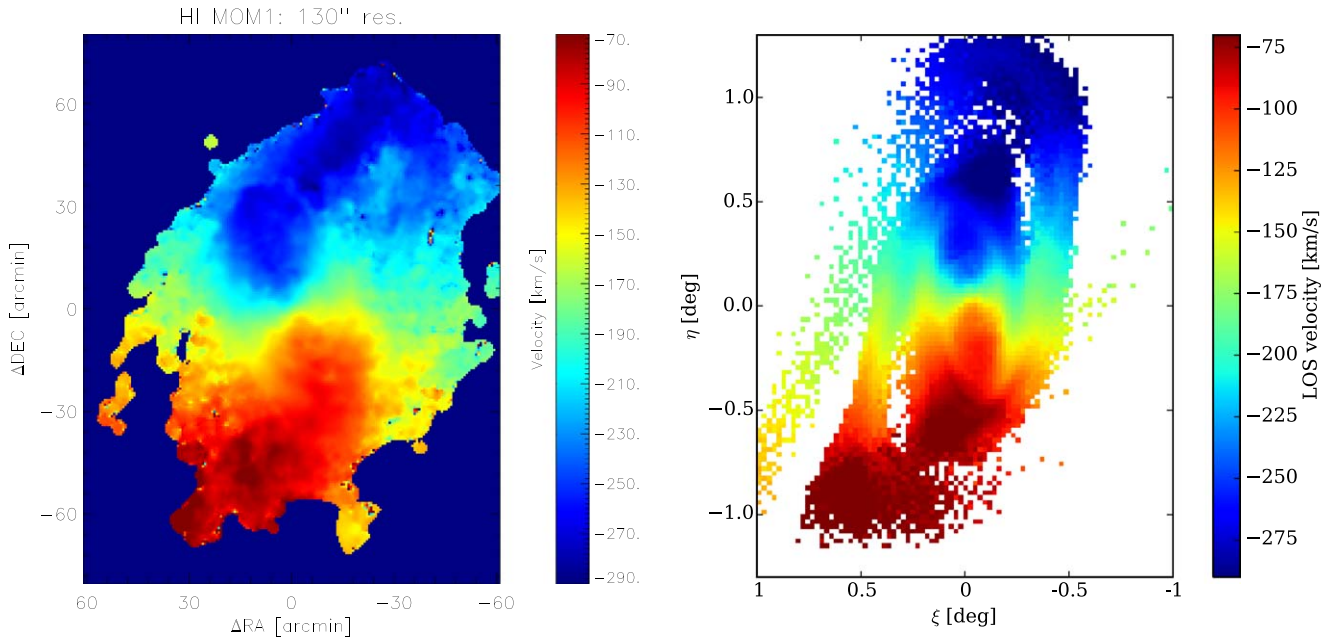


Figure 9. Left: H I velocity map of M33 from C14 (reproduced with permission © ESO). Right: gas velocity map of M33 for the best-matching projection and time from our simulation. The simulated image has a similar resolution to the one from C14. While constructing our map, we took only those bins that contained more than five particles in order to cut off the extended tidal tails and better mimic the image of C14.

disk. The corresponding arc is also present in the image from C14. The extended tidal arm is not clearly visible in the H I map; however, this red arc may be a hint that perhaps some sort of tidal arm is present there. We note that the image obtained from the RPS experiment possesses features similar to those of Figure 9.

4.3. The Stellar Stream

Unlike the gaseous warp, which has been known since the 1970s (Rogstad et al. 1976), its stellar counterpart was discovered only recently by McConnachie et al. (2009). Because this structure has been known for a much shorter time, it has been examined to a lesser extent than the warp. In Section 4.2, we selected the time and the best viewing position to match the warp. In this subsection, we briefly discuss the fact that for the same projection, the stellar stream is also present. In general, we could have repeated the whole procedure to find a stream that resembles the observed one more; however, its shape is not as well investigated as that of the warp, and it changes its orientation from C-like to S-like when stars with different metallicities are selected (McConnachie et al. 2010; Lewis et al. 2013).

Figure 10 presents the surface density distribution of all stars from our simulation. We decided to show the simplest possible image that can be obtained from the simulations and not translate it into surface brightness or apply complex processing to mimic images like Figure 13 of McConnachie et al. (2010), since performing such procedures on the simulation data would not be straightforward and require many assumptions and model-dependent methods. In this paper, we only want to quickly and qualitatively compare the resulting structure to observations.

We find that in general the simulated stream resembles the observed one. The two most evident features are in both cases the northwestern and southeastern extensions. The simulated streams span $\sim 2^\circ$, which is similar to the observations. The

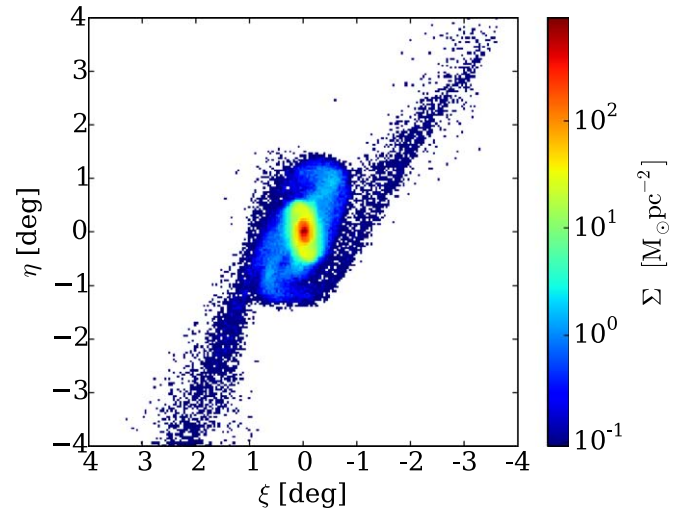


Figure 10. Surface density distribution for all stars from the simulated M33 at the time of the best match and seen from the best viewing position.

structure discussed in McConnachie et al. (2010) seems a bit more vertically elongated; however, this could also be accomplished in the simulations by choosing a different viewing position. The image from the simulation obviously has a better resolution, and some substructures that are visible here (for example, a small gap in the southeastern extension) would probably be smoothed out and not visible in observations. The surface density of the edge of the simulated disk is about 10 times bigger than the density of the stream. This agrees with the contours given by McConnachie et al. (2010), where the ratio of the surface brightness between the first and the last contour is 5.75. Apart from resembling the observed stellar structure, our simulated stream is also very similar to the simulated one presented by McConnachie et al. (2009), where the stream is made of wound up and projected tidal tails.

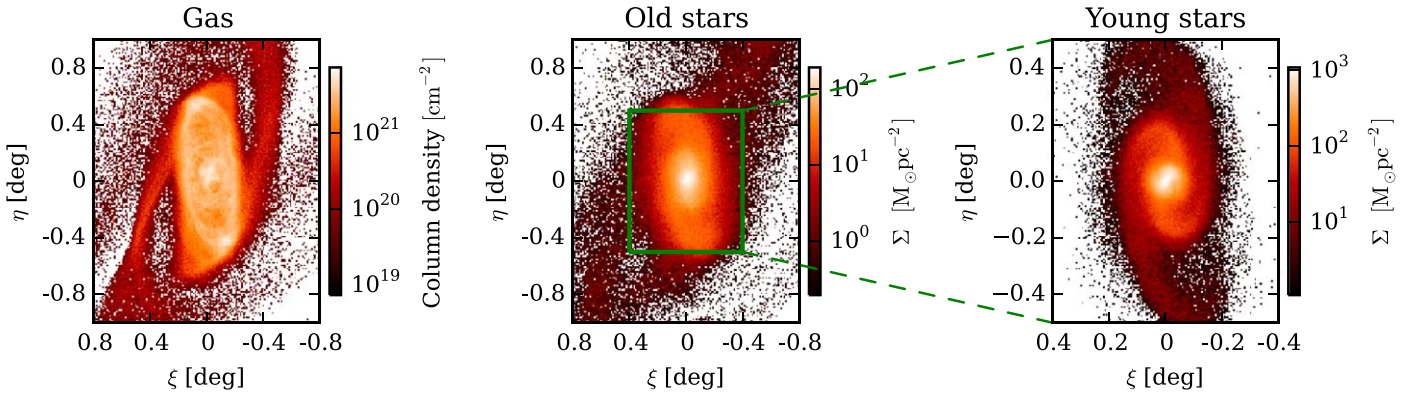


Figure 11. Surface density maps of the neutral hydrogen (left), old stars (middle), and young stars (right) of the simulated M33 at the best-match time and projection.

4.4. The Spiral Arms

As seen in Figure 6, both the gaseous and the stellar disks possess a grand-design spiral structure at the time of the best match. The two-armed spiral signal is characteristic of tidally induced spirals and is also present in the observed M33. Figure 11 shows how the spiral arms of our simulated galaxy appear in projection on the sky, seen from the best-match point of view. For the neutral hydrogen map, the similarity with the H I image of C14 is very good. The projection and the fragmented nature of the gaseous disk makes the arms look more flocculent, which is also the case for the C14 image where it is hard to identify the number of arms.

In the stellar images, the spiral arms are clearly more visible in young stars. This closely agrees with observations, since generally young stars are a better tracer of spiral structure. The spiral arms reach deeper into the young stellar disk than the old disk, a result of the fact that the young stellar disk was formed out of gas and is about twice as small as the old disk (see Figure 6). The spiral structure penetrates the young disk down to $\sim 3\text{--}6$ arcmin and is stopped there by the presence of a bar. The size of these spiral arms is similar to that seen in the $B\text{--}V\text{--}I$ image of C14 made from the Massey et al. (2006) survey. The connection between the arms and the bar is a bit different in our simulated image compared to the one presented by C14. However, this results from the way the bar is formed in our simulations (which is not by tidal interaction; see Section 4.5), and it would be very difficult to match its position angle with the observed one.

Besides the qualitative inspection of the spiral structure, several quantitative properties may be measured for spiral arms, namely their number (i.e., multiplicity), strength, pitch angle, and pattern speed. First, we measured different Fourier modes $|A_m|$ (similarly to, e.g., Pettitt et al. 2016) for the three different components to see what their dominant spiral signal is. Their time evolution is presented in Figure 12. A grand-design ($m = 2$) signal is clearly being tidally induced shortly after the pericenter passage and is stronger than other modes in all three components. Unfortunately, we do not reproduce higher modes, which are present in the observed M33 (and also in other tracers, e.g., in $H\alpha$; see Kam et al. 2015). Reproducing the multi-armed structure in M33, which is not a dominant one, would require better tuning of the initial model of M33, since the number of arms is mostly a function of a disk-to-halo mass ratio (Athanioula et al. 1987; D’Onghia 2015). In our work, we focused mainly on tidally induced morphological features in

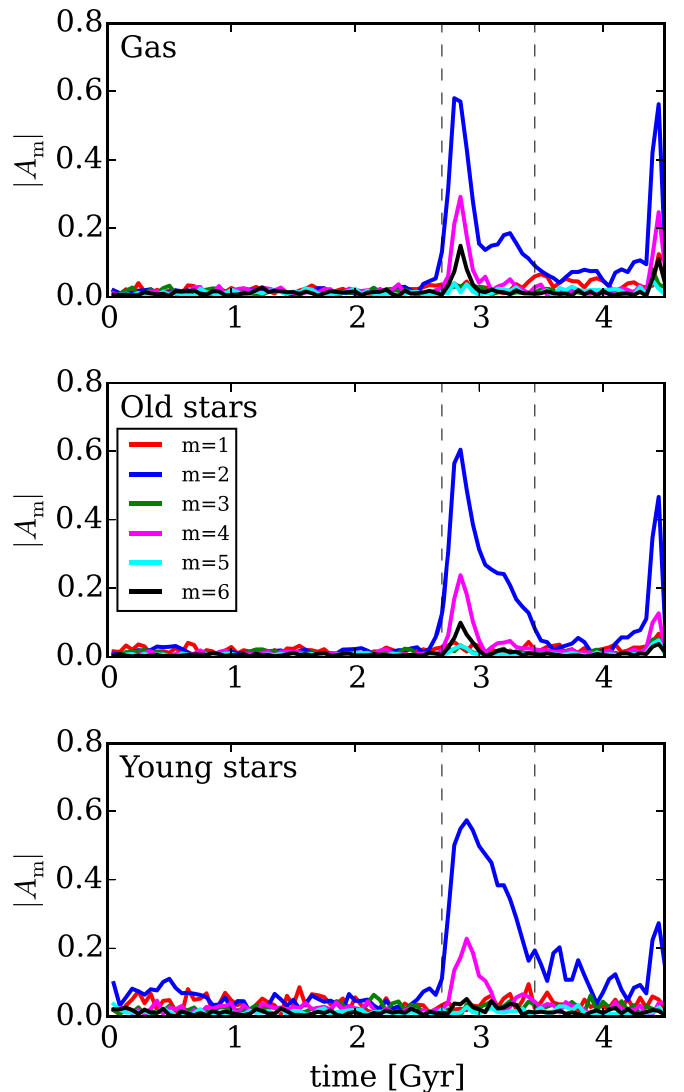


Figure 12. Time dependence of the $|A_m|$ Fourier coefficients measured in rings of $4 \text{ kpc} < R < 11 \text{ kpc}$ for the gas (upper panel) and old stars (middle panel) and $3 \text{ kpc} < R < 6 \text{ kpc}$ for young stars (lower panel). The first vertical dashed line indicates the time of the pericenter passage and the second one marks the time of the best match.

M33, and we did not modify the model too much after we found the one that fits the rotation curve.

In order to measure the pitch angle and the strength of spiral arms, we expanded the surface distribution of gas and stellar

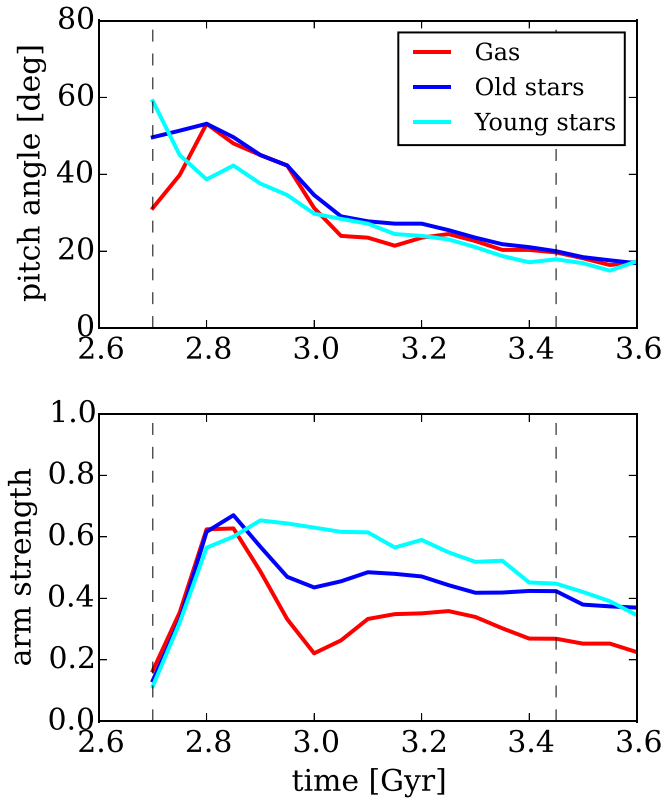


Figure 13. Upper panel: the time dependence of the pitch angle for the gas and old and young stars measured in the same rings as in Figure 12. Lower panel: the time dependence of the arm strength for the same components measured in the same rings. The first vertical dashed line indicates the time of the pericenter passage and the second one marks the time of the best match.

particles in logarithmic spirals as discussed in, e.g., Sellwood & Athanassoula (1986). A more detailed description of the method we used can be found in Section 3.2 of Semczuk et al. (2017). The time evolution of these parameters after the pericenter passage is presented in Figure 13. The pitch angle starts from high values during the pericenter, $\sim 40^\circ$ – 60° for all components. Later, it exponentially decreases, reaching 19° . 6 for the gas, 21° . 8 for old stars, and 17° . 9 for young stars, at the time of the best match. The value for the best tracer of the spiral structure, i.e., young stars, agrees very well with the pitch angle for the $m = 2$ structure, 16° . 5 obtained by Considere & Athanassoula (1988) and 17° . 1 found by Puerari (1993). The values for the other components also lie close to these measurements. This finding argues for the possibility that the grand-design component of the spiral structure of M33 was indeed induced tidally, and the pitch angle had enough time after the encounter to wind up to the observed value. We note that higher values for the pitch angle of the $m > 2$ structure may be found in the literature (e.g., Sandage & Humphreys 1980) and also measurements may reach $\sim 40^\circ$ for $m = 2$ (references in Considere & Athanassoula 1988). However, as described by Considere & Athanassoula (1988), these values originate from measurements in the outer, looser spiral structure of M33, and the best fit for the brightest inner two-armed structure is indeed $\sim 16^\circ$. We conclude that the degree of winding up of the brightest component of the spiral structure in our simulations agrees very well with the brightest component in observations.

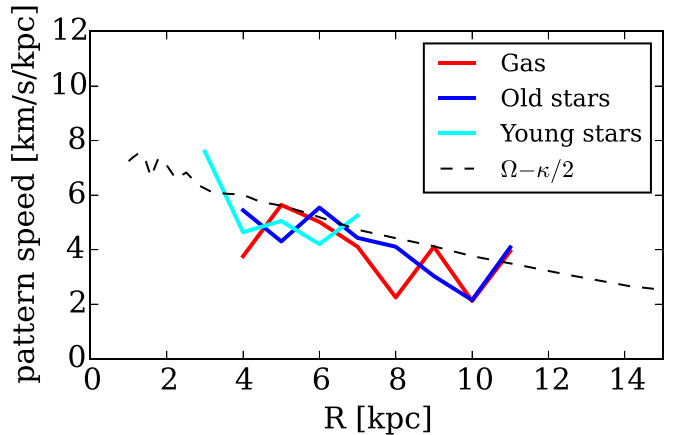


Figure 14. Radial dependence of the pattern speed measured between the time of the best match and 0.15 Gyr before this time.

The lower panel of Figure 13 shows the time evolution of the arm strength. It peaks at approximately the same time as $|A_{m=2}|$ in Figure 12, and later it slowly decreases with time, which means that the spirals are dissolving. At the time of the best match, the highest value of the arm strength is in the young stellar component, which closely corresponds with the fact that the spiral structure is most pronounced in this component.

The last property that we measured for the spiral arms of the simulated M33 is the pattern speed. We used the method discussed, e.g., by Dobbs (2011), which relies on tracking the maximum of the surface density Σ_{\max} in polar coordinates at a given radius between two time epochs. The pattern speed can then be calculated as the difference between the angular positions of the maxima, divided by the time difference. The radial dependence of the mean pattern speed of the two-armed structure at the time of the best match is presented in Figure 14. We find that for both the gaseous and the old stellar arms, the pattern speed decreases radially and tightly follows the inner Lindblad resonance. This indicates that the spiral arms are kinematic density waves, as expected for tidally induced arms (Dobbs & Baba 2014). Estimates of the pattern speed of M33 found in the literature (e.g., $15 \text{ km s}^{-1} \text{ kpc}^{-1}$ by Courtes & Dubout-Crillon 1971 or $28 \text{ km s}^{-1} \text{ kpc}^{-1}$ by Puerari 1993) highly exceed the values obtained from our simulation. This discrepancy probably arises from the fact that those estimates were based on the quasistationary density wave theory, where the pattern speed of the arms is constant. This is not the case in our simulation, and it was only recently reported (Saha & Elmegreen 2016) that a constant pattern speed can, in fact, be obtained in an N -body case.

4.5. The Bar

The observed M33 is known to possess a small bar in the central parts of its disk (Elmegreen et al. 1992; Regan & Vogel 1994; Corbelli & Walterbos 2007; Hernández-López et al. 2009). As can be seen in Figures 6 and 11, our simulated M33 also forms a bar, mostly in the young stellar disk. In order to verify whether the origin of this bar is related to the tidal interaction or due to the secular instability of the disk, we measured the time evolution of the Fourier mode $|A_2| \equiv |A(2, p = 0)|$ in the inner 3 kpc of the face-on surface distribution of all stars for the fiducial simulation and the simulation of M33 in isolation. The upper panel of Figure 15

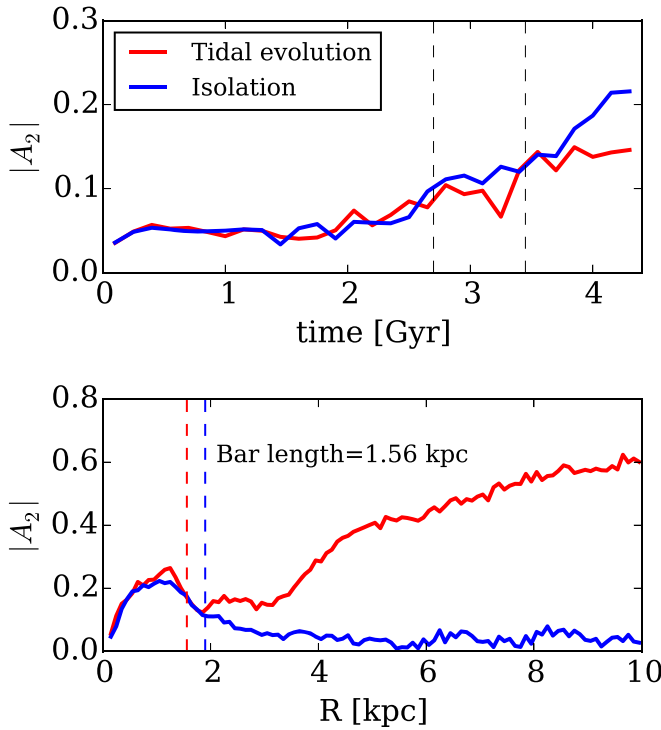


Figure 15. Upper panel: the time evolution of the $|A_2|$ Fourier mode calculated within the radius of 3 kpc for our fiducial simulation and for the case in isolation. The first vertical dashed line indicates the time of the pericenter passage and the second one marks the time of the best match. Lower panel: the radial profiles of $|A_2|$ measured at the time of the best match for the fiducial simulation and at the corresponding time for the isolated case. Dashed lines indicate estimates of the bar length.

shows that the tidal evolution has very little influence on the bar formation and even slightly suppresses it.

The fact that the bar in isolation grows bigger is also confirmed by the measurement of its length in both cases. We estimate the bar length by calculating the radial dependence of $|A_2|$ and finding where it drops below a fixed threshold (here we assume it to be 0.5 of the maximum value of the inner peak). This method yields a length of 1.56 kpc at the time of the best match for the simulation with M31 and 1.9 kpc for the isolated case at the corresponding time (lower panel of Figure 15). While this estimate (1.56 kpc) agrees quite well with one of the measurements in the literature (1.5 kpc by Elmegreen et al. 1992), it is at least two times larger than other measurements (e.g., 0.4 kpc by Regan & Vogel 1994 or 0.7 kpc by Corbelli & Walterbros 2007). The value obtained by Elmegreen et al. (1992) has been suspected of being biased by the influence of the very tight spiral arms surrounding the bar in that region (Hernández-López et al. 2009), and the agreement with it seems to be coincidental.

The bar in our simulation is formed in the young stellar disk, only because this disk is formed from the gas and is very unstable. If we started our simulation later (or earlier) the bar length would be different, since the bar would have had enough time to grow bigger (as in isolation) or would not have had enough time to grow to the present size. In this paper, we aim to investigate the very recent history of M33, although we cannot determine when exactly the processes responsible for bar formation started. Our results only confirm that the influence of tidal interactions on bars can be ambiguous, and

they do not always accelerate bar formation (Pettitt & Wadsley 2018).

4.6. The SFH

Bernard et al. (2012) reprocessed the data from Barker et al. (2011) for two fields in M33 at radii 9.1 and 11.6 kpc and found a peak in the SFH that occurred ~ 2 Gyr ago. The density of the SFR had a value of $0.6 \times 10^{-9} M_\odot \text{ yr}^{-1} \text{ pc}^{-2}$ at that time, which is approximately three times larger than the average values found for earlier times. Bernard et al. (2012) also found similar activity in the SFH of M31 and suggested that the past mutual interaction of both galaxies might have caused those synchronized peaks.

We checked whether M33 in our simulation also exhibits a rapid increase in SFR at similar radii. Figure 16 presents the time evolution of the densities of SFR measured in rings (and one circle) of sizes of 1 kpc. At the beginning of the simulation, the values of the SFR were obviously high in the central regions, where most of the star formation happened. As the star formation slowly quenches, these values decrease and stabilize. At radii 6 to 12 kpc, the SFR rapidly increases again after the pericenter passage (marked as the first vertical dashed line in Figure 16). The values are from 2 to 10 times greater than the average ones before. The values closest to those found by Bernard et al. (2012) occur at distances from 6 to 9 kpc. However, it is difficult to compare the absolute values between simulations and observations, because the SFR was measured in a different way and in different kind of fields (here in rings, in observations in two square fields). The peak of the SFR in the simulation is separated by around 0.75 Gyr from the time of the best match, a period ~ 2.6 times smaller than the one found by Bernard et al. (2012). When comparing these times of the peak, it is worth keeping in mind that deriving the SFH is strongly model dependent. For example, for the same fields, Barker et al. (2011) obtained the increased SFR at ~ 3 and ~ 6 Gyr ago. We conclude that the pericenter passage of ~ 37 kpc can induce an increase in the SFR of the same relative order and at similar radii as observed. We also found that introducing the hot gas halo of M31 does not change these results regarding SFHs at different radii.

4.7. The Extended Gaseous Structure

More than a decade ago, Braun & Thilker (2004) found a faint H I stream that seems to connect M31 and M33. Using test-particle simulations, Bekki (2008) showed that such a bridge-like structure may have been tidally induced by the interaction between the two galaxies. To see whether such a feature would be present in the model of interaction presented here, we used the simulations that included the RPS, since as we showed in Section 4.2, this additional physical process is crucial in reproducing better the outer regions of the cold gas of M33. We found no cold gas component stretching in a bridge-like form between M33 and M31. This finding partially agrees with the results of Wolfe et al. (2016), who showed that the majority of H I between the two galaxies is contained in small discrete clouds rather than in a bridge. In our simulations, we do not have enough resolution to model such objects.

In our fiducial simulation, we found cold gas stretching from M33 in the direction of M31 and also on the other side of M33 (similarly to the stars as seen in Figure 10). This structure formed as a result of tidal stripping; however, as discussed in

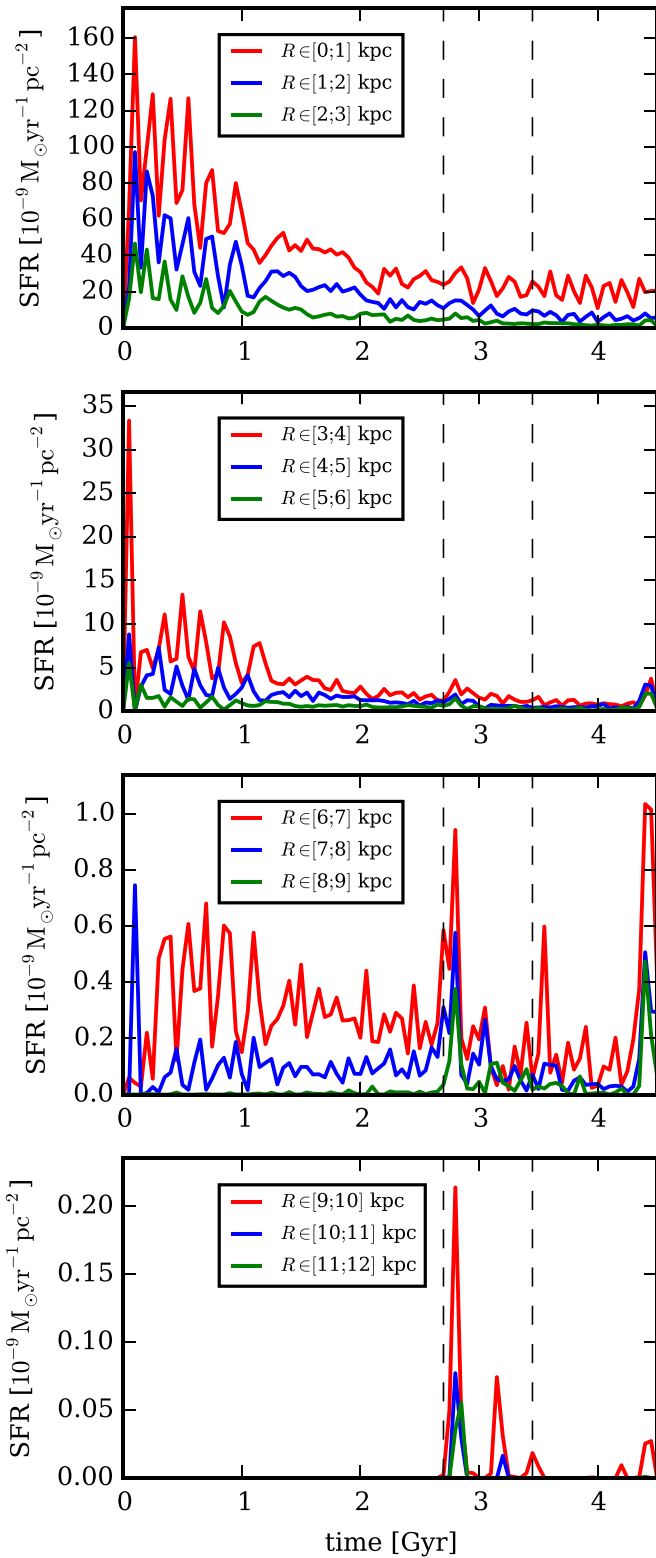


Figure 16. Time evolution of the SFR normalized to the area of the ring (or circle) in which it was measured. The first dashed vertical line indicates the time of the pericenter passage; the second marks the time of the best match.

Section 4.2, we had to include RPS to weaken these features, since their signal was too strong inside 1° from the disk of M33, which is not seen in observations.

Despite not finding an extended structure of neutral hydrogen northwest from M33, in the RPS experiment, we

find low-density gas material southeast from M33 (partially visible in the lower panel of Figure 7). The position of this material corresponds well with the H I clouds recently found by Keenan et al. (2016). The LOS velocities of the material from the simulation and the clouds of Keenan et al. (2016) are consistently oriented toward the observer; however, the observed material is approaching faster than M33 itself, while in our simulations this velocity is lower than the one of M33. We did not investigate the properties of this material in greater detail, since one of the conclusions of Keenan et al. (2016) was that at the moment we cannot rule out the possibility that this gas is in fact some contamination from the Magellanic stream.

5. Discussion

5.1. Accuracy and Uniqueness of the Model

As stated in the introduction, the model presented here is not aimed to precisely reproduce the Triangulum Galaxy and its present relative position and velocity with respect to Andromeda. The main goal of this study was to show that once we adopt the values of the structural parameters that are similar to the ones derived from observations and use them in numerical simulations, the observed morphology of M33, the burst in its SFH, and the relative position and velocity with respect to M31 may be reproduced with reasonable accuracy. The purpose of this paper is to show that the observed parameters allow for the interaction with M31 to sufficiently disturb the disk of M33, and that such scenario utilizes an orbit that is consistent with measurements of distances and velocities of both galaxies.

We noted several times that discrepancies between our model and the observations still persist. The biggest discrepancy seems to be in the relative position between M31 and M33 at the best-match time and projection, specifically in the X -direction, where it lies only within 1.75σ of the adopted error bar. This corresponds to a difference of 41.1 kpc. The errors we adopted here as 1σ originated from the assumption that measurements have Gaussian error distributions, and we can easily transform them into different reference frames. These errors are not the maximal possible errors. The maximal possible errors of the relative positions are the same in all directions and equal to the sum of errors of both distances (assuming that the sky coordinates have exact values), i.e., 63 kpc. This value is greater than the discrepancy of our results. However, the adopted errors that we used seem slightly underestimated when we compare them with a rather large range of observationally derived distances to both galaxies, especially M33. For example, in the NASA/IPAC Extragalactic Database (NED), the measurements of the distance to M33 range from ~ 620 kpc to ~ 960 kpc (with the mean value of 849 kpc and the standard deviation of 212 kpc). This sample may be biased by very old measurements; nevertheless, Gieren et al. (2013) considered a sample of more recent attempts and the range of distances was still quite extended, from ~ 720 kpc to ~ 970 kpc. Comparing this range with our adopted error of 23 kpc suggests that taking such a small error may be recognized as a little too optimistic. Reviewing the results presented in the literature and their discrepancies shows that the astrophysics of the M33–M31 system is a branch of science with a distance accuracy of ~ 50 – 100 kpc, rather than ~ 25 kpc, as it is for the projected position errors.

This huge range of possible values that are only weakly observationally constrained gives modelers a variety of

parameters to explore. The distance to M33 is not the only parameter with such a big allowed range. For example, the mass of M31 may vary from $\sim 7 \times 10^{11} M_{\odot}$ (Evans et al. 2000) up to $\sim 2.5 \times 10^{12} M_{\odot}$ (according to the introduction in Patel et al. 2017a). In general, one could run simulations with different halo models of M33 and M31, gaseous and stellar disks of M33 and M31, the bulges of both galaxies included or not, the gaseous halo of M31, as well as different relative orbits and inclinations of both galaxies, particle resolutions, hydrodynamical solvers, and subgrid models and their parameters. The simplest strategy would be to perform simulations probing a multidimensional grid of parameters; however, such a task would be computationally expensive and the analysis of the simulations would be very difficult, given the abundance of observational properties to reproduce.

While constructing the model described in this paper, we applied a different strategy, given the limited resources that we had. In the first step, we found the initial orbit using an orbit integration scheme. This orbit was later tested and corrected in *N*-body runs. These runs were used as a basis for the following SPH simulations, which were also iteratively corrected after comparing the obtained properties of the galaxy with observations. The model presented here is a result of about 80 such iterations. Some of these intermediate steps reproduced certain observables better than the fiducial model (e.g., the peak in the SFH occurred a longer time ago); however, this was obtained at a cost of less similarity to other observables. Reproducing a particular galaxy is therefore a minimalization issue, and the fiducial model we present here seemed to be a compromise in terms of the similarities with the most important characteristics of M33.

It is certainly possible to obtain a better model. The simulation including the hot gas halo of M31 looks very promising, and exploring this scenario further with a code that resolves the RPS better (Agertz et al. 2007; Hopkins 2015) would be very interesting. Probing better the parameter space of orbits and inclinations in this setup perhaps could also give a better result. Given the huge uncertainty of the proper motions of M31, we do not exclude the possibility that the true velocity vector lies somewhere between the sets of vdM12 and S16.

Most features of M33 that were induced due to the interaction with M31 in our simulation are of tidal origin and therefore depend strongly on the orbit, inclinations, and mass models. The subgrid physics seems not to be very important, and our results are rather robust against different models of star formation, etc. The peak in SFH after the pericenter passage might be the only observable that could have been changed by subgrid physics. We tested our model with a code with different subgrid prescriptions, and a similar effect of the increase in SFR during the pericenter passage was also found. Some extreme model with a very low density threshold and very high feedback could probably alter this result and prevent a strong increase in star-forming activity.

5.2. Comparison with Previous Works

The first model of the interaction between M33 and M31 was presented by Bekki (2008). The test-particle simulations presented there were tailored to reproduce the H I bridge found earlier by Braun & Thilker (2004). In our model, we do not find such a bridge-like structure, as was the case in Bekki (2008). In the fiducial simulations without RPS, we obtained instead tidal arms that were extended up to $\sim 4^{\circ}\text{--}5^{\circ}$ in both directions

(similarly to the stellar tails in Figure 10). These features, however, were dissolved in the run with RPS that reproduced better the outer gaseous structures of M33. This discrepancy with the results of Bekki (2008) comes from many differences between our works; however, the most important is probably the inclusion of hydrodynamics and hot gas halo in our case, since the run without it produced similar features. Our finding of no bridge-like structure is in agreement with recent results (e.g., Wolfe et al. 2013) that question the possibility that H I between M31 and M33 is due to the past interaction between the two galaxies. Apart from the bridge, Bekki (2008) does not discuss other features associated with the interaction scenario, hence it is difficult to further compare with his work.

The second model of the interaction was presented by McConnachie et al. (2009). They performed high-resolution *N*-body simulations in order to reproduce the stellar distortion of the disk, the discovery of which was reported in the very same paper. Similarly to Bekki (2008), they adopted a small ($8 \times 10^{10} M_{\odot}$) halo mass of M33 and a relatively large halo mass of M31 ($2.47 \times 10^{12} M_{\odot}$). This assumption of a small mass ratio of only $\sim 3\%$ between M33 and M31 makes the modeling of the orbit much easier, since such a system can be approximated as a small satellite orbiting a massive spiral. We assumed such masses of both galaxies with the aim to reproduce their rotation curves (C14; Corbelli et al. 2010), and this resulted in the mass ratio of $\sim 26\%$, for which the system has to be treated more like a two-body interaction of similar-sized objects.

Another difference between our work and McConnachie et al. (2009) is that their orbit, just like Bekki's, was not constrained by the measurement of the M31 transverse velocity, which was unknown at that time. Despite these different assumptions, we find that our model agrees with the one presented by McConnachie et al. (2009). The pericenter distance they used was similar (~ 50 kpc), and the warp in their disk looks very similar to ours, especially for the stellar component (Figure 10). The stream-like structure, just as in our case, is made of tidally distorted material that wound up and, in a specific projection, has a different orientation than the disk. After the pericenter passage, their M33 ends up more distant from M31 than ours (the apocenter is ~ 260 kpc in their model and ~ 151 kpc in ours), but this is a result of the smaller mass ratio discussed earlier. Unfortunately, any quantitative results regarding, e.g., the spiral arms or SFH (due to the lack of hydrodynamics in their simulations) were not discussed by McConnachie et al. (2009) so we cannot compare our model with theirs in more detail.

Besides the work in the literature that aimed to reproduce the hypothetical past interaction between M33 and M31, several authors have argued that such a scenario was unlikely using different orbital studies. First, Shaya & Tully (2013) used the numerical action method and backward orbit integration to conclude that M33 and M31 are currently at the closest approach. According to the information in the appendix of their paper, their scheme did not include the effect of dynamical friction. However, as shown in Appendix A of van der Marel et al. (2012a), orbital studies with and without implementation of dynamical friction may vary a lot (i.e., the apocenter may change from 800 kpc to 100 kpc), with the former agreeing much better with the simulations. After finding that M33 is now at its closest approach to M31, Shaya & Tully (2013) suggested that Andromeda XXII (And XXII), the only candidate for a

satellite of M33 (Chapman et al. 2013), could have disturbed the disk of M33. We will discuss this alternative scenario more in Section 5.3.

More recently, Patel et al. (2017b, 2017a) explored the past orbital history of two systems, the MW–Large Magellanic Cloud and M31–M33. In the first paper (Patel et al. 2017b), they applied backward orbit integration to find possible orbits of both systems and compared them to orbits from dark matter only cosmological simulations. In Section 7.1 of their paper, they state that from backward orbit integration of 10,000 initial velocities drawn from 4σ proper-motion error space, they found that less than 1% of orbits had a pericenter smaller than 100 kpc in the last 3 Gyr. As can be seen in Figure 13 of their paper, these 10,000 velocities cover well the area surrounding the velocity that results from adopting the van der Marel et al. (2012b) proper motions, while the area near the results of Salomon et al. (2016) is not probed.

In Section 2 of our paper, we extend these results of Patel et al. (2017b) to also probe the region surrounding estimates of the velocity resulting from adopting the values of Salomon et al. (2016). Our findings agree with the conclusion of Patel et al. (2017b) that once one adopts the transverse velocity of M31 from van der Marel et al. (2012b), the recent and close pericenter passage is not very plausible. This agreement also holds if we take into account the fact that we used different mass models of the galaxies (in particular, M33 is almost twice as massive in our work). The conclusions about the recent pericenter change once the estimates of van der Marel et al. (2012b) are replaced by those of Salomon et al. (2016). Since the publication of the most recent estimates of the M31 transverse velocity, no other measurements were made to support one or the other of the conflicting estimates. Furthermore, cosmological simulations (Carlesi et al. 2016) do not strongly exclude any of these estimates. Moreover, such simulations do not exclude a close pericenter passage, as discussed by Patel et al. (2017b), where the analysis of orbits from the Illustris-Dark (Vogelsberger et al. 2014) simulation showed that orbits with pericenters even lower than 55 kpc are very common ($\sim 30\%$) for similar pairs of halos. The probability of orbits with pericenters smaller than 50 kpc was found to be even higher in a recent study of orbits of similar pairs in cosmological simulations that included baryonic physics (Shao et al. 2018).

In the second paper, Patel et al. (2017a) used a Bayesian inference scheme and the Illustris-Dark simulations to estimate the masses of MW and M31. One of the conclusions of this paper was that after adopting the criteria for the recent interaction scenario, the mass of M31 would be $\sim 10^{12} M_{\odot}$. This value is not far from the estimates of the M31 mass found in the literature; for example, it lies within the error bars of the result of Watkins et al. (2010), $1.4 \pm 0.4 \times 10^{12} M_{\odot}$. We argue that the precision of the estimates of the mass of M31 is not high enough to rule out $\sim 10^{12} M_{\odot}$ and abandon the interaction scenario.

5.3. Alternative Scenarios

Both Shaya & Tully (2013) and Patel et al. (2017b) proposed a passage of And XXII as a new alternative scenario that could disturb the gaseous and stellar disk of M33. Here we try to roughly estimate the impact of the tidal force that such a passage would have had and compare it with the impact in the scenario presented in this paper. Elmegreen et al. (1991)

defined the parameter S that quantifies the strength of the tidal interaction. Their definition makes use of the masses of the perturber and the perturbed galaxy, the pericentric distance, the size of the perturbed galaxy as well as the timescales of the interaction and of the motions of the stars in the perturbed disk. Since constraining the orbit of And XXII around M33 would give too many free parameters, we decided to apply instead a parameter that does not use the timescales and was discussed, e.g., in Oh et al. (2015):

$$P = \left(\frac{M_{\text{ptb}}}{M_g} \right) \left(\frac{R_g}{d} \right)^3. \quad (1)$$

Here, M_{ptb} and M_g denote the masses of the perturber and the perturbed galaxy, R_g is the size of the perturbed galaxy, which we take to be five times the disk scale length, and d is the pericentric distance. For the case of the simulation described in this paper, the tidal parameter takes the value of $P = 0.03$, where we assumed that the mass of the perturber is the mass of M31 enclosed within the pericentric distance. We know from our simulation that the tidal interaction characterized by this number can disturb the disk of M33 and the induced morphology mimics the observed one to a certain degree.

We now want to find out what size of pericenter And XXII would need to have in order to provide the same tidal impact. In order to estimate this, we need the mass of And XXII. Adopting the value of Shaya & Tully (2013), $1.3 \times 10^7 M_{\odot}$, we obtain the pericenter of 1.3 kpc. Tollerud et al. (2012) estimated the mass in And XXII enclosed within the half-light radius to be $\log(M_{1/2}/M_{\odot}) = 6.67 \pm 1.08$. If we take the upper limit of this measurement and assume that the half-light radius encompasses only 10% of the total mass, the estimated pericenter will still be only 4.5 kpc. Such small pericenter values suggest that the low-mass And XXII would have to pass extremely close to M33 in order to have the tidal impact similar to the one induced by M31 in our simulation. We expect that such a close passage would perturb more the inner parts of the disk of M33, which seems to be undisturbed. The warp and the stellar stream occur at much greater radii. We find that the scenario in which And XXII induced the warp in M33 is less likely, due to the small mass of this satellite.

Another possibility is that the more massive satellites of M33 disturbed its outer disk, but they are yet to be discovered. This scenario could perhaps explain the warped gaseous feature, since gas is less massive and hence less bound and easier to distort. A different possible scenario for the gas disk distortion could also be an asymmetric gas accretion. However, these two explanations would not be very convincing in the case of the stellar component. Studying MW analogs, Gómez et al. (2017) found that a satellite should have a mass of at least 1% of the host to induce some sort of vertical distortion in the disk. It would be very surprising if a satellite of M33 of a corresponding brightness existed and has not yet been discovered. Perhaps the distorted stellar and gaseous disks are remnants of a major merger that M33 underwent in the past, but this scenario would raise another question of why the inner disk remained unaffected by such an event. Hopefully, future observations and simulations will shed more light on the peculiar history of M33.

Very recently, van der Marel et al. (2018) utilized *Gaia* DR2 results to estimate the proper motions of both M31 and M33. Based on the agreement of the new result for M31 with their

previous *HST* estimate and on the orbit integration sample from Patel et al. (2017b), they argue that M33 may be on its first infall into M31. We find this interpretation unlikely for the following three reasons. First, the error bars of the van der Marel et al. (2018) estimates are very large, and the resulting 3D relative velocity between M31 and M33, based solely on *Gaia* DR2 measurements, is in 1.75σ agreement with the relative velocity for the best match of our model (Section 4.2), in which the two galaxies recently interacted. Second, the orbit integration sample from Patel et al. (2017b) was selected from the 4σ space around the van der Marel et al. (2012b) measurements and naturally will fall far from the new measurements (in Figure 4 of van der Marel et al. 2018), as that region was not fully probed and therefore the distance between the new results and points with a pericenter might just be an artifact of the probing of the phase space. Finally and most importantly, we do not consider a semi-analytic orbit integration method to be a robust computational tool that can rule out with any confidence one scenario or another for the past history of M33 and M31. Orbits obtained by this method do not reproduce the simulations accurately, since it does not include mass loss originating from tidal stripping and parameters of the dynamical friction have to be fitted to a particular setup.

Moreover, in the close proximity to M31, there are some massive satellite galaxies that would most likely have some influence on the M33–M31 orbit. The mass of M32 was estimated to be $8 \times 10^{10} M_{\odot}$ (Dierickx et al. 2014), which is around 20% of the mass of M33, and M110 has a similar magnitude to M32 (McConnachie 2012). Including these factors in the orbit integration would create a lot of degeneracy, since their proper motions are unknown and finding the true orbit between M33 and M31 would be even more complicated. The simple scenario of the interaction that we discussed here favored more the Salomon et al. (2016) estimates, but perhaps the influence of M32 and M110 would change this conclusion, and other estimates of the transverse velocity of M31 would be in agreement with the M33–M31 interaction scenario.

6. Summary

In this work, we revisited the scenario discussed in P09 and McConnachie et al. (2009), which was proposed to explain the stellar and gaseous disks of M33 which were disturbed by a recent passage close to M31. We used the orbit integration method to verify which of the measurements of the transverse velocity of M31 favors this scenario more. We found that while the estimates of van der Marel et al. (2012b) do not support this common history of the two galaxies, the estimates of Salomon et al. (2016) allow for it. We performed *N*-body/SPH simulations, aiming to reproduce the observed disturbed morphology of M33 and at the same time to be consistent with the 3D relative position and velocity of the galaxies resulting from the estimates of Salomon et al. (2016). The fiducial setup presented here fulfills the orbital conditions and had the pericenter at the distance of 37 kpc, which was close enough to tidally disturb the disk of M33. Mass models of both galaxies in our simulations were constructed to roughly reproduce the observed rotation curves.

We found that the tidal impulse originating from such an interaction is sufficient to excite a two-armed spiral structure similar to the one found to be the dominant spiral component in

the observed M33. Tides also induced distortion in the stellar and gaseous disks at larger radii, with the former having the shape and the extent similar to the observed one. The disturbance of the gaseous disk, however, was found to be similar in the inner parts while in the outer parts, it was dominated by strong tidal/spiral features that are not present in the observed data. We showed by performing an additional run including the hot gas halo of M31 that the RPS is a crucial component in modeling the gaseous warp of M33 in greater detail.

Finally, we also found that the tidal forces in our simulations were sufficient to compress the gas in M33 during the pericenter passage and trigger a burst of star formation at similar radii to those found by Bernard et al. (2012) and hypothesized to be due to the passage near M31, since similar activity was found in its SFH at approximately the same time. The model presented here did not aim to reproduce the observed M33 in great detail, and this was not achieved; rather, its aim is to demonstrate that observationally constrained structural and orbital parameters of the system allow for the interaction to trigger in M33 features similar to the observed ones.

This work was supported in part by the Polish National Science Centre under grant 2013/10/A/ST9/00023. We are grateful to an anonymous referee for useful comments that helped to improve the paper. We thank L. Widrow for providing procedures to generate *N*-body models of galaxies for initial conditions. We are grateful to S. Fouquet for sharing the modified version of the GADGET-2 code and to his collaborators F. Hammer and J. Wang for incorporating the modifications. We thank S. Z. Kam and L. Chemin for sharing the HI data of M33 as well as E. Corbelli, M. Putman, and the editorial board of A&A for granting us the permission to reprint certain figures. Acknowledgments are also due to J.-C. Lambert for his tutorial about the tool for the visualization of the simulations glnemo2 and for making it public. We appreciate insightful discussions with G. Gajda, K. Kowalczyk, I. Ebrova, N. Peschken, and J. S. Gallagher III that contributed to this paper. M.S. is grateful for the hospitality of Laboratoire d’Astrophysique de Marseille and the University of Wisconsin at the time of his visits. E.A. acknowledges financial assistance from the CNES and access to the HPC resources of CINES under the allocation 2017-[A0040407665] made by GENCI. E. D. acknowledges the support and the hospitality of the Center for Computational Astrophysics (CCA) at the Flatiron Institute during the preparation of this work and the Vilas Associate Professor Fellowship at the University of Wisconsin, Madison. This research has made use of the NASA/IPAC Extragalactic Database (NED), which is operated by the Jet Propulsion Laboratory, California Institute of Technology, under contract with the National Aeronautics and Space Administration.

Appendix A Relative Positions and Velocities

Following van der Marel et al. (2012b), we adopted the distance to M33 and its error as $D_{\text{M33}} = 794 \pm 23$ kpc (McConnachie et al. 2004) and for M31, $D_{\text{M31}} = 770 \pm 40$ kpc (van der Marel & Guhathakurta 2008 and references therein). We combined these values with the distance of the Sun from the Galactic center $R_0 = 8.29 \pm 0.16$ kpc (McMillan 2011) to obtain the relative position vector between M33 and

M31 in the so-called Galactocentric rest frame. This Cartesian reference frame (X , Y , Z) is defined as follows: the center lies on the Galactic center, the X -axis points in the direction from the Sun to the Galactic center, the Y -axis points in the direction of the Sun's rotation in the Galaxy, and the Z -axis points toward the Galactic north pole. The resulting relative position vector between M33 and M31 with error bars is

$$\mathbf{X}_{\text{rel}} = (-97.2 \pm 23.5, -121.6 \pm 34.8, -129.8 \pm 19.0) \text{ kpc}. \quad (2)$$

In order to calculate the relative velocity between the two galaxies in the same reference frame, first we used the values of the proper motions of M33 from Brunthaler et al. (2005), the LOS velocity as used in van der Marel et al. (2012b), $v_{\text{LOS},\text{M33}} = -180 \pm 1 \text{ km s}^{-1}$ (van der Marel & Guhathakurta 2008), and applied the correction for the motion of the Sun ($U_{\odot}, V_{\odot} + V_{\text{LSR}}, W_{\odot}$) = $(11.1 \pm 0.7, 255.2 \pm 5.1, 7.25 \pm 0.36) \text{ km s}^{-1}$ (Schönrich et al. 2010; Reid et al. 2014). Then we considered the proper motions and LOS velocity of M31 as given by van der Marel et al. (2012b), corrected for the same solar values. This yields the first option for the relative velocity,

$$\mathbf{V}_{\text{rel,vdM12}} = (-23.2 \pm 34.3, 177.4 \pm 29.2, 93.7 \pm 38.5) \text{ km s}^{-1}. \quad (3)$$

The second possible value of the relative velocity was obtained by replacing the values for M31 with those given by Salomon et al. (2016) and correcting for the same solar values. This yields

$$\mathbf{V}_{\text{rel,S16}} = (-72.0 \pm 64.4, 86.4 \pm 48.0, 10.6 \pm 62.1) \text{ km s}^{-1}. \quad (4)$$

For all calculations done here, we assumed that error bars follow a Gaussian distribution. We have adopted this approximation in order to be able to easily transform error bars from one reference frame to another.

Appendix B Orbit Integration Scheme

In order to quickly find possible orbits of the two galaxies without running computationally costly simulations, we performed semi-analytic orbit integrations, similar to those described in Patel et al. (2017b) and Dierickx & Loeb (2017a, 2017b). We treated both galaxies as two interacting NFW halos (Navarro et al. 1997), and we included the dynamical friction from M31 acting on M33. We thus solved the following equations of motion:

$$\ddot{\mathbf{x}}_{\text{M33}} = -\nabla\psi_{\text{M31}} + \mathbf{f}_{\text{DF}}, \quad \ddot{\mathbf{x}}_{\text{M31}} = -\nabla\psi_{\text{M33}}. \quad (5)$$

Here, \mathbf{x}_{M33} and \mathbf{x}_{M31} denote the positions of the M33 and M31 galaxies. The functions ψ_{M33} and ψ_{M31} are the NFW potentials of M33 and M31, respectively, given by

$$\psi_i = -\frac{GM_i}{r[\ln(1 + c_i) - c_i/(1 + c_i)]} \ln\left(1 + \frac{r}{r_{s,i}}\right), \quad (6)$$

where M_i are the virial masses of the galaxies, c_i are their concentration parameters, and $r_{s,i} = r_{v,i}/c_i$ are the scale radii, i.e., the virial radii $r_{v,i}$ divided by concentrations. For both

galaxies, we adopted halo parameters that were estimated by modeling the observed rotation curves. For M33, we assumed $M_{\text{M33}} = 4.38 \times 10^{11} M_{\odot}$ and $c_{\text{M33}} = 11$ (C14). The halo mass includes the estimate of the mass of baryons in M33, discussed in greater detail in Section 3.1. For M31, we took $M_{\text{M31}} = 2 \times 10^{12} M_{\odot}$ and $c_{\text{M31}} = 28$ to fit the rotation curve given by Corbelli et al. (2010) only with the potential of the halo (see Section 3.1). For the supplementary parameters necessary to compute the NFW profile, we adopted the virial overdensity to be $\Delta_c = 102$ and the critical density $\rho_c^0 = 136 M_{\odot} \text{kpc}^{-3}$.

Finally, \mathbf{f}_{DF} in Equation (5) denotes the acceleration caused by the dynamical friction, approximated in our calculations according to the Chandrasekhar formula (Chandrasekhar 1943):

$$\mathbf{f}_{\text{DF}} = -\frac{4\pi G^2 M_{\text{M33}} \ln \Lambda \rho(r)}{v^2} \left[\text{erf}(X) - \frac{2X}{\sqrt{\pi}} \exp(-X^2) \right] \frac{\mathbf{v}}{v}, \quad (7)$$

where $\rho(r)$ is the density of the M31 halo at a given radius r , \mathbf{v} is the relative velocity vector with its magnitude $|\mathbf{v}| = v$, and $X = v/\sqrt{2\sigma}$, where σ is the 1D velocity dispersion, which we approximated according to the formula derived by Zentner & Bullock (2003). For the Coulomb logarithm $\ln \Lambda$, we adopted the formula presented in Hashimoto et al. (2003) and used by Dierickx & Loeb (2017a, 2017b):

$$\ln \Lambda = \ln\left(\frac{r}{1.4\epsilon}\right), \quad (8)$$

where ϵ is the softening length of the galaxy subject to dynamical friction. We fit this parameter for M33 by comparing the integrated orbits with orbits in preliminary, collisionless, low-resolution simulations. We estimated the value $\epsilon = 28.5 \text{ kpc}$ to be the best match. To integrate Equations (5), we used a symplectic leapfrog integration method as described in Springel et al. (2001).

Appendix C Simulations in Isolation

In order to confirm that the morphological features like the gaseous warp, the stellar stream, and the grand-design spiral arms originate from the tidal interaction with M31 and are not induced by secular processes (e.g., feedback or star formation) in the disk of M33, we evolved this galaxy in isolation for the same time as in the case with the perturber. Figure 17 presents surface density maps for all three components of M33 evolved in isolation at 3.45 Gyr, the time of the best match for the fiducial model. A quick look at these images and the comparison with Figure 6 is enough to confirm that the aforementioned features are indeed tidally induced, since none of the components of the isolated galaxy shows signs of similar distortions. Particles present above and below the gaseous disk in Figure 17 that are distributed in an hourglass-like shape have been ejected there by feedback and contribute a very small fraction of the total gaseous content. They are absent in the images of the fiducial model, most likely because of tidal stripping. The young stellar disk also reveals a small bar which is not a tidal feature as discussed in Section 4.5.

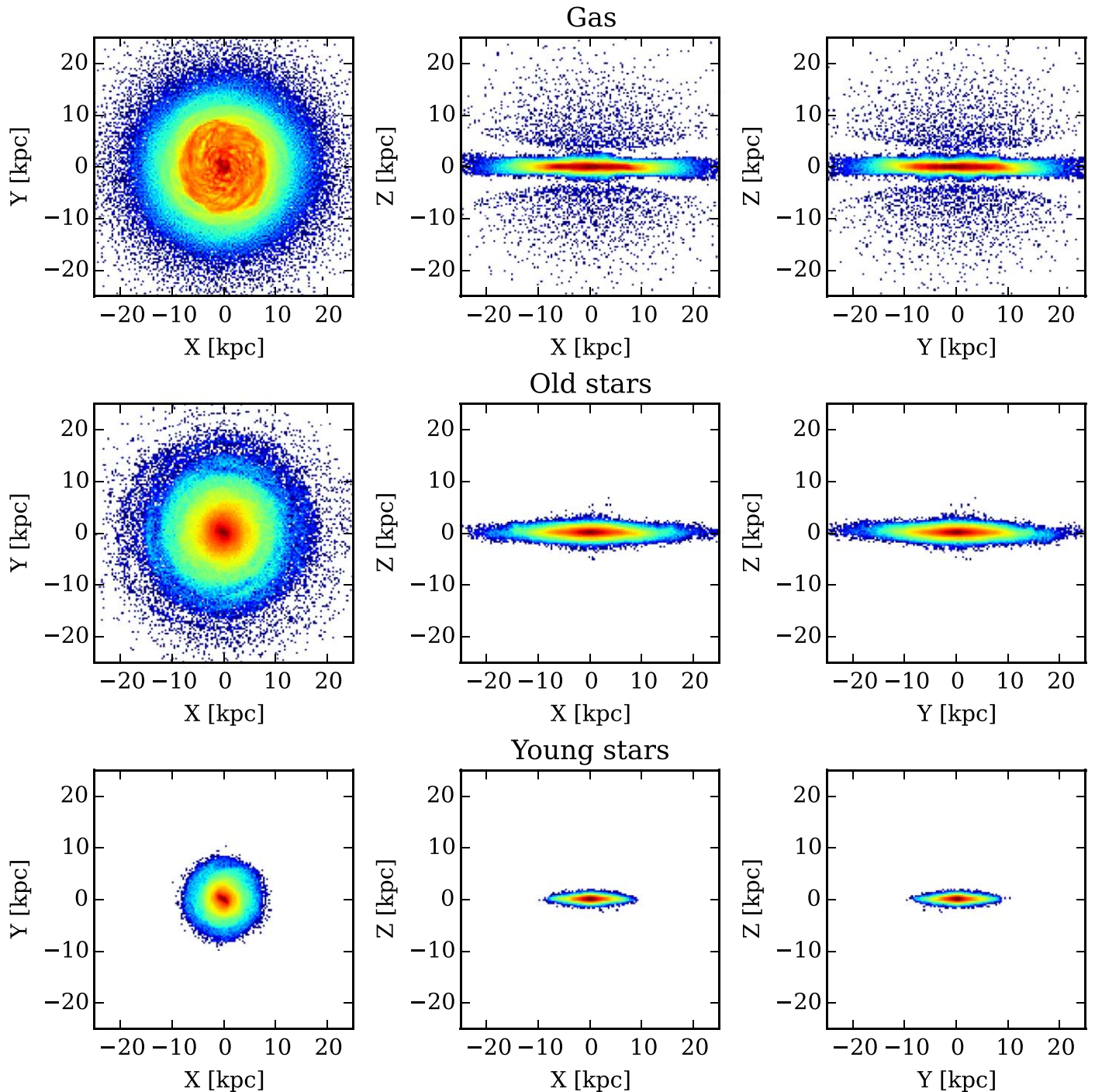


Figure 17. Surface density distributions seen from three different directions for the gas and the old and young stellar particles for the M33 galaxy simulated in isolation at the time corresponding to the time of the best match for the fiducial model.

ORCID iDs

Marcin Semczuk <https://orcid.org/0000-0002-8191-8918>
 Ewa L. Łokas <https://orcid.org/0000-0001-7138-8899>
 E. Athanassoula <https://orcid.org/0000-0001-6079-1332>

References

- Agertz, O., Moore, B., Stadel, J., et al. 2007, *MNRAS*, **380**, 963
- Arthur, J., Pearce, F. R., Gray, M. E., et al. 2017, *MNRAS*, **464**, 2027
- Athanassoula, E. 2013, in Bars and Secular Evolution in Disk Galaxies: Theoretical Input, ed. J. Falcón-Barroso & J. H. Knapen (Cambridge: Cambridge Univ. Press), 305
- Athanassoula, E., Bosma, A., & Papaioannou, S. 1987, *A&A*, **179**, 23
- Athanassoula, E., Machado, R. E. G., & Rodionov, S. A. 2013, *MNRAS*, **429**, 1949
- Barker, M. K., Ferguson, A. M. N., Cole, A. A., et al. 2011, *MNRAS*, **410**, 504
- Bekki, K. 2008, *MNRAS*, **390**, L24
- Bernard, E. J., Ferguson, A. M. N., Barker, M. K., et al. 2012, *MNRAS*, **420**, 2625
- Besla, G., Kallivayalil, N., Hernquist, L., et al. 2012, *MNRAS*, **421**, 2109
- Braun, R., & Thilker, D. A. 2004, *A&A*, **417**, 421
- Brunthaler, A., Reid, M. J., Falcke, H., et al. 2005, *Sci*, **307**, 1440
- Byrd, G., & Valtonen, M. 1990, *ApJ*, **350**, 89
- Carlesi, E., Hoffman, Y., Sorce, J. G., et al. 2016, *MNRAS*, **460**, L5
- Chandrasekhar, S. 1943, *ApJ*, **97**, 255
- Chapman, S. C., Widrow, L., Collins, M. L. M., et al. 2013, *MNRAS*, **430**, 37

- Considere, S., & Athanassoula, E. 1988, *A&AS*, **76**, 365
- Corbelli, E., Lorenzoni, S., Walterbros, R., et al. 2010, *A&A*, **511**, 89
- Corbelli, E., & Schneider, S. E. 1997, *ApJ*, **479**, 244
- Corbelli, E., Thilker, D., Zibetti, S., et al. 2014, *A&A*, **572**, 23
- Corbelli, E., & Walterbros, R. A. M. 2007, *ApJ*, **669**, 315
- Courtes, G., & Dubout-Crillon, R. 1971, *A&A*, **11**, 468
- Cox, T. J., Jonsson, P., Primack, J. R., & Somerville, R. S. 2006, *MNRAS*, **373**, 1013
- D’Onghia, E. 2015, *ApJL*, **808**, L8
- D’Onghia, E., Besla, G., Cox, T. J., & Hernquist, L. 2009, *Natur*, **460**, 605
- D’Onghia, E., & Fox, A. J. 2016, *ARA&A*, **54**, 363
- D’Onghia, E., Madau, P., Vera-Ciro, C., Quillen, A., & Hernquist, L. 2016, *ApJ*, **823**, 4
- D’Onghia, E., Vogelsberger, M., Faucher-Giguere, C.-A., & Hernquist, L. 2010, *ApJ*, **725**, 353
- Dierickx, M., Blecha, L., & Loeb, A. 2014, *ApJL*, **788**, L38
- Dierickx, M., & Loeb, A. 2017a, *ApJ*, **836**, 92
- Dierickx, M., & Loeb, A. 2017b, *ApJ*, **847**, 42
- Dobbs, C., & Baba, J. 2014, *PASA*, **31**, e035
- Dobbs, C. L. 2011, *MSAIS*, **18**, 109
- Dobbs, C. L., Theis, C., Pringle, J. E., & Bate, M. R. 2010, *MNRAS*, **403**, 625
- Elmegreen, B. G., Elmegreen, D. M., & Montenegro, L. 1992, *ApJS*, **79**, 37
- Elmegreen, D. M., Sundin, M., Sundelius, B., & Elmegreen, B. 1991, *A&A*, **244**, 52
- Evans, N. W., Wilkinson, M. I., Guhathakurta, P., Grebel, E. K., & Vogt, S. S. 2000, *ApJL*, **540**, L9
- Fouquet, S., Łokas, E. L., del Pino, A., & Ebrová, I. 2017, *MNRAS*, **464**, 2717
- Gajda, G., Łokas, E. L., & Athanassoula, E. 2017, *ApJ*, **842**, 56
- Gieren, W., Górska, M., Pietrzynski, G., et al. 2013, *ApJ*, **773**, 69
- Gómez, F. A., White, S. D. M., Grand, R. J. J., et al. 2017, *MNRAS*, **465**, 3446
- Guntherd, G., Diaz, R. J., & Aguero, M. P. 2006, *AJ*, **132**, 150
- Hammer, F., Yang, Y. B., Wang, J. L., et al. 2010, *ApJ*, **725**, 542
- Hashimoto, Y., Funato, Y., & Makino, J. 2003, *ApJ*, **582**, 196
- Hernández-López, I., Athanassoula, E., Mujica, R., & Bosma, A. 2009, *RMxAC*, **37**, 160
- Hernquist, L. 1990, *ApJ*, **356**, 359
- Hopkins, P. F. 2015, *MNRAS*, **450**, 53
- Horellou, C., & Combes, F. 2001, *Ap&SS*, **276**, 1141
- Humphreys, R. A., & Sandage, A. 1980, *ApJS*, **44**, 319
- Hunter, C., & Toomre, A. 1969, *ApJ*, **155**, 747
- Kahn, F. D., & Woltjer, L. 1959, *ApJ*, **130**, 705
- Kam, Z. S., Carignan, C., Chemin, L., et al. 2017, *AJ*, in press (arXiv:1706.04248)
- Kam, Z. S., Carignan, C., Chemin, L., Amram, P., & Epinat, B. 2015, *MNRAS*, **449**, 4048
- Katz, N., Weinberg, D. H., & Hernquist, L. 1996, *ApJS*, **105**, 19
- Keenan, O. C., Davies, J. I., Taylor, R., & Minchin, R. F. 2016, *MNRAS*, **456**, 951
- Lehner, N., Howk, J. C., & Wakker, B. P. 2015, *ApJ*, **804**, 79
- Lewis, G. F., Braun, R., McConnachie, A. W., et al. 2013, *ApJ*, **763**, 4
- Lockman, F. J., Free, N. L., & Shields, J. C. 2012, *AJ*, **144**, 52
- Łokas, E. L., Athanassoula, E., Debattista, V. P., et al. 2014, *MNRAS*, **445**, 1339
- Łokas, E. L., Ebrová, I., del Pino, A., et al. 2016, *ApJ*, **826**, 227
- Łokas, E. L., Semczuk, M., Gajda, G., & D’Onghia, E. 2015, *ApJ*, **810**, 100
- Massey, P., Olsen, K. A. G., Hodge, P. W., et al. 2006, *AJ*, **131**, 2478
- McConnachie, A. W. 2012, *AJ*, **144**, 4
- McConnachie, A. W., Ferguson, A. M. N., Irwin, M. J., et al. 2010, *ApJ*, **723**, 1038
- McConnachie, A. W., Irwin, M. J., Ferguson, A. M. N., et al. 2004, *MNRAS*, **350**, 243
- McConnachie, A. W., Irwin, M. J., Ibata, R. A., et al. 2009, *Natur*, **461**, 66
- McMillan, P. J. 2011, *MNRAS*, **414**, 2446
- Miller, M. J., & Bregman, J. N. 2015, *ApJ*, **800**, 14
- Navarro, J. F., Frenk, C. S., & White, S. D. 1997, *ApJ*, **490**, 493
- Newton, K. 1980, *MNRAS*, **190**, 689
- Oh, S. H., Kim, W.-T., & Mok, H. 2015, *ApJ*, **807**, 73
- Pardy, S. A., D’Onghia, E., & Fox, A. J. 2018, arXiv:1802.01600
- Patel, E., Besla, G., & Mandel, K. 2017a, *MNRAS*, **468**, 3428
- Patel, E., Besla, G., & Sohn, S. T. 2017b, *MNRAS*, **464**, 3825
- Pettitt, A. R., Tasker, E. J., & Wadsley, J. W. 2016, *MNRAS*, **458**, 3990
- Pettitt, A. R., & Wadsley, J. W. 2018, *MNRAS*, **474**, 5645
- Puerari, I. 1993, *PASP*, **105**, 1290
- Putman, M. E., Peek, J. E. G., Muratov, A., et al. 2009, *ApJ*, **703**, 1486
- Regan, M. W., & Vogel, S. N. 1994, *ApJ*, **434**, 536
- Reid, M. J., Menten, K. M., Brunthaler, A., et al. 2014, *ApJ*, **783**, 130
- Renaud, F., Athanassoula, E., Amram, P., et al. 2018, *MNRAS*, **473**, 585
- Renaud, F., Bournaud, F., & Duc, P.-A. 2015, *MNRAS*, **446**, 2038
- Rogstad, D. H., Wright, M. C. H., & Lockhart, I. A. 1976, *ApJ*, **204**, 703
- Ruggiero, R., & Lima Neto, G. B. 2017, *MNRAS*, **468**, 4107
- Saha, K., & Elmegreen, B. 2016, *ApJL*, **826**, L21
- Salo, H., & Laurikainen, E. 2000, *MNRAS*, **319**, 393
- Salomon, J.-B., Ibata, R. A., Famaey, B., et al. 2016, *MNRAS*, **456**, 4432
- Sandage, A., & Humphreys, R. M. 1980, *ApJL*, **236**, L1
- Schönrich, R., Binney, J., & Dehnen, W. 2010, *MNRAS*, **403**, 1829
- Sellwood, J. A., & Athanassoula, E. 1986, *MNRAS*, **221**, 195
- Semczuk, M., Łokas, E. L., & del Pino, A. 2017, *ApJ*, **834**, 7
- Shao, S., Cautun, M., Deason, A. J., & Frenk, C. S. 2018, *MNRAS*, **479**, 284
- Shaya, E. J., & Tully, R. B. 2013, *MNRAS*, **436**, 2096
- Sohn, S. T., Anderson, J., & van der Marel, R. P. 2012, *ApJ*, **753**, 7
- Springel, V. 2005, *MNRAS*, **364**, 1105
- Springel, V., Yoshida, N., & White, S. D. M. 2001, *NewA*, **6**, 79
- Teyssier, R., Chapon, D., & Bournaud, F. 2010, *ApJL*, **720**, L149
- Theis, C., & Spinneker, C. 2003, *Ap&SS*, **284**, 495
- Tollerud, E. J., Beaton, R. L., Geha, M. C., et al. 2012, *ApJ*, **752**, 45
- van der Marel, R. P., Besla, G., Cox, T. J., Sohn, S. T., & Anderson, J. 2012a, *ApJ*, **753**, 9
- van der Marel, R. P., Fardal, M., Besla, G., et al. 2012b, *ApJ*, **753**, 8
- van der Marel, R. P., Fardal, M. A., Sohn, S. T., et al. 2018, arXiv:1805.04079
- van der Marel, R. P., & Guhathakurta, P. 2008, *ApJ*, **678**, 187
- Vogelsberger, M., Genel, S., Springel, V., et al. 2014, *MNRAS*, **444**, 1518
- Wang, J. L., Hammer, F., Athanassoula, E., et al. 2012, *A&A*, **538**, A121
- Watkins, L. L., Evans, N. W., & An, J. H. 2010, *MNRAS*, **406**, 264
- Widrow, L. M., & Dubinski, J. 2005, *ApJ*, **631**, 838
- Widrow, L. M., Pym, B., & Dubinski, J. 2008, *ApJ*, **679**, 1239
- Wolfe, S. A., Lockman, F. J., & Pisano, D. J. 2016, *ApJ*, **816**, 81
- Wolfe, S. A., Pisano, D. J., Lockman, F. J., McGaugh, S. S., & Shaya, E. J. 2013, *Natur*, **497**, 224
- Zentner, A. R., & Bullock, J. S. 2003, *ApJ*, **598**, 49

TIDAL STIRRING AND THE ORIGIN OF DWARF SPHEROIDALS IN THE LOCAL GROUP

LUCIO MAYER^{1,4}, FABIO GOVERNATO², MONICA COLPI¹, BEN MOORE³, THOMAS QUINN⁴, JAMES WADSLEY^{4,5}, JOACHIM STADEL⁴ & GEORGE LAKE⁴

¹Dipartimento di Fisica, Università Degli Studi di Milano Bicocca, via Celoria 16, I-20133 Milano, Italy

²Osservatorio Astronomico di Brera, via Bianchi 46, I-23807 Merate (LC) - Italy

³Department of Astronomy, University of Durham, Durham, U.K., DH1 3LE

⁴Department of Astronomy, University of Washington Seattle, USA, WA 98196

⁵Department of Physics and Astronomy, McMaster University, Hamilton, Ontario L8S 4M1 Canada

To appear in ApJL

ABSTRACT

N-body + SPH simulations are used to study the evolution of dwarf irregular galaxies (dIrrs) entering the dark matter halo of the Milky Way or M31 on plunging orbits. We propose a new dynamical mechanism driving the evolution of gas rich, rotationally supported dIrrs, mostly found at the outskirts of the Local Group (LG), into gas free, pressure supported dwarf spheroidals (dSphs) or dwarf ellipticals (dEs), observed to cluster around the two giant spirals. The initial model galaxies are exponential disks embedded in massive dark matter halos and reproduce nearby dIrrs. Repeated tidal shocks at the pericenter of their orbit partially strip their halo and disk and trigger dynamical instabilities that dramatically reshape their stellar component. After only 2-3 orbits low surface brightness (LSB) dIrrs are transformed into dSphs, while high surface brightness (HSB) dIrrs evolve into dEs. This evolutionary mechanism naturally leads to the morphology-density relation observed for LG dwarfs. Dwarfs surrounded by very dense dark matter halos, like the archetypical dIrr GR8, are turned into Draco or Ursa Minor, the faintest and most dark matter dominated among LG dSphs. If disks include a gaseous component, this is both tidally stripped and consumed in periodic bursts of star formation. The resulting star formation histories are in good qualitative agreement with those derived using HST color-magnitude diagrams for local dSphs.

Subject headings: galaxies: Local Group — galaxies: dwarfs — galaxies: evolution — galaxies: kinematics and dynamics — galaxies: interactions — methods: N-Body simulations

1. INTRODUCTION

Dwarf galaxies in the Local Group (LG) clearly obey a morphology-density relation. Close to the Milky Way and M31 we find early-type dwarf galaxies, namely faint ($M_B > -14$) low surface brightness dwarf spheroidals (dSphs) and more luminous ($M_B > -17$), higher surface brightness dwarf ellipticals (dEs). All these galaxies are nearly devoid of gas, contain dark matter and mainly old stars and are supported by velocity dispersion (Ferguson & Binggeli 1994, hereafter FB94; Mateo 1998, hereafter Ma98; Grebel 1999, hereafter Gr99; Van den Bergh 1999). Among them Draco and Ursa Minor have the highest dark matter densities ever measured (Lake 1990). On the outskirts of the LG we find similarly faint ($M_B > -18$) and dark matter dominated dwarf irregular galaxies (dIrrs), that are gas rich, star-forming systems with disk-like kinematics (Ma98, Van den Bergh 1999, Gr99).

Previous attempts to explain the origin of dSphs in the LG have relied on gas dynamical processes to remove the gas in dIrrs. Gas stripping may result either because of the pressure exerted by an external hot gaseous medium in the halo of the Milky Way (“ram pressure”) (Einasto et al. 1974) or because of internal strong supernovae winds (Dekel & Silk 1986). However, ram pressure would require an external gas density that is several orders of magnitude higher than recently inferred for the Milky Way (Murali 2000) and supernovae winds cannot explain the existing morphology-density relation. Moreover, such dissipative mechanisms would remove the gas but would not directly

alter the structure and kinematics of the pre-existing stellar component. However, the light follows an exponential profile in both dSphs and dIrrs (Faber & Lin 1983; Irwin & Hatzidimitriou 1995; Ma98) and a positive correlation between surface brightness and luminosity is shown by both types of dwarfs (FB94), suggesting an evolutionary link between them. Is there a mechanism that can transform dwarf galaxies between morphological classes or must we accept the idea that dSphs are fundamentally different from dIrrs?

Within rich galaxy clusters, fast fly-by encounters with the largest galaxies can transform a disk system into a spheroidal or S0 galaxy in just 3-4 Gyr (Moore et al. 1996, 1998). If the halos of bright galaxies were scaled down versions of galaxy clusters then this “galaxy harassment” would be equally important within them. However, whereas rich clusters contain over thirty large (L_*) perturbing galaxies, the Milky Way and M31 have only a couple of satellites sufficiently massive to harass the other dwarf galaxies (Moore et al. 1999; Klypin et al. 1999) As a result, the rate for effective satellite-satellite fly-by encounters is less than one in every 10 Gyr (the LMC and the SMC being a notable exception).

Thus, we are left only with the repeated action of tidal forces from the primary galaxy as an evolutionary driver. These operate on the orbital timescale, which is of order of 3-4 Gyr in both clusters and galactic halos. However, given the relatively low age of large, virialized clusters, galaxies have typically approached the cluster center only

once by the present time, while dSphs satellites have had sufficient time to complete several close tidal encounters with the Milky Way, as stellar ages imply that the latter was already in place 10 Gyr ago (Van den Bergh 1996).

In this paper we use very high resolution N-Body + SPH simulations performed with the parallel binary treecode GASOLINE (Dikaikos & Stadel 1996; Wadsley et al. 2000) to follow the evolution of small galaxies resembling dIrrs as they move on bound orbits in the tidal field of the massive dark matter halo of the Milky Way.

2. MODELS OF DWARF GALAXIES

The Milky Way halo is modeled as the fixed potential of a truncated isothermal sphere with a total mass $4 \times 10^{12} M_{\odot}$ inside a radius of 400 kpc, consistent with both recent measures based on radial velocities of distant satellites (Wilkinson & Evans 1999) and with generic models of structure formation (Peebles et al. 1989). The core radius is 4 kpc and the resulting circular velocity at the solar radius is 220 km/s.

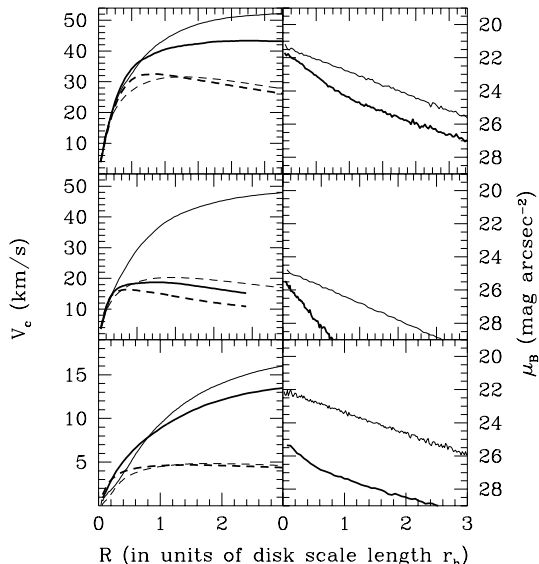


Fig. 1.— Evolution of circular velocity (left) and surface brightness profiles (right) for our model galaxies: thin lines are used for the initial profiles, thick lines for the profiles after 7 Gyr. From top to bottom, models *M2H*, *M2La* and *GR8* are shown. The overall (stars + dark matter) circular velocity profile is always represented by a solid line, while a dashed line describes the contribution of the stellar component alone. For the final surface brightness profile we take into account fading according to the star formation history described in the text. We assume that the last burst occurs 4 Gyr ago for HSBs and LSBs and 7 Gyr ago for GR8, thus resulting in a more pronounced fading for the latter. The different choices correspond to the different epochs of infall inferred from our evolutionary model. The orbits had an apo/peri of 9 and a pericenter of ~ 40 kpc (HSBs and LSBs) and 12 kpc (GR8), with random disk orientations.

Our simulated galaxies are modeled as exponential disks of stars with a Toomre parameter $Q = 2$ embedded in truncated isothermal dark matter halos (see Hernquist 1993). The number of particles in the disk is 50,000 while that in

the halo ranges from 250,000 to 3×10^6 . Such high resolution in the halo reduces considerably numerical heating of the disk due to massive halo particles, as was tested by evolving our models in isolation for 5 Gyr. The scale-lengths and masses of the stellar disk and dark matter halo are chosen so that the satellites follow the observed B band Tully-Fisher relation (Hoffman et al. 1996; Zwaan et al. 1997) and have realistic rotation curves (de Blok & McGaugh 1997; Cote et al. 1997), as shown in Figure 1. The determination of general scaling properties of galaxies becomes more uncertain at the very faint end. Current structure formation models predict that the mass M and scale radius R of halos (and of their embedded disks) vary with redshift as $\sim (1+z)^{-3/2}$ for a fixed value of the circular velocity V_c , with $V_c \sim R \sim M^{1/3}$ (Mo et al. 1998).

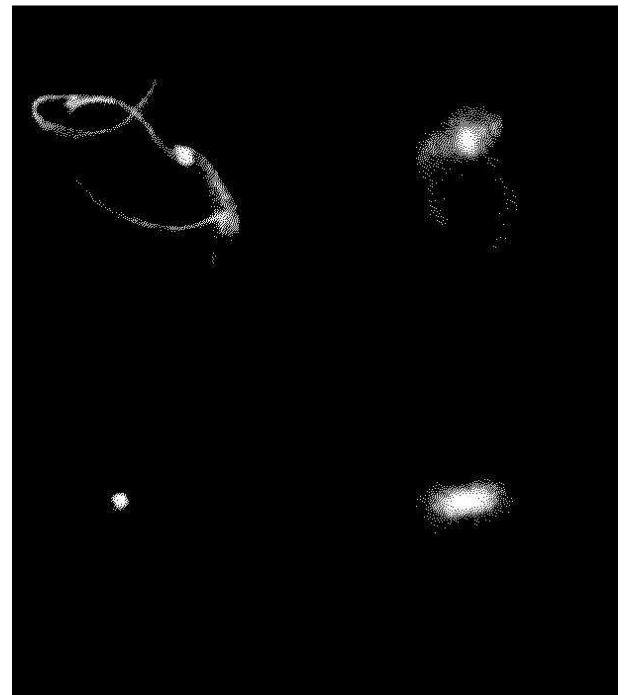


Fig. 2.— The final stellar configurations of our model galaxies. Left panels show the stellar streams of the LSB (upper) and HSB (lower) satellites viewed face on (the orbit has apo/peri=4). The boxes are 500 kpc on a side, with brighter colors showing regions with higher density. Right panels show close up views of the remnants seen edge-on in frames of 50 kpc on a side.

The scaling with redshift reflects the fact that low mass halos form at early epochs and have higher characteristic densities because the average density of the Universe was higher. Galaxies with total masses $< 10^9 M_{\odot}$ should typically form at $z \geq 2$ (Lacey & Cole 1993) and should live in halos with a central dark matter density $\sim 0.3 M_{\odot}\text{pc}^{-3}$, comparable to what inferred for GR8, an extremely faint LG dIrr (Carignan et al. 1990). The model with the smallest mass (“GR8”) was built following these prescriptions.

The models cover the entire luminosity function of irregulars in the LG (Ma98) with stellar masses of $1.2 \times 10^6 M_{\odot}$ ($M_B = -11.2$, “GR8”), $9 \times 10^8 M_{\odot}$ ($M_B = -16.23$, “M2”)

and 2.5×10^9 ($M_B = -18$, “M1”). At fixed disk mass (either M1 or M2) we also vary the disk scale length, obtaining high surface brightness (HSBs, $\mu_B = 21.5$ mag arcsec $^{-2}$, M1H and M2H) or low surface brightness satellites (LSBs, $\mu_B = 24.5$ or 23.5 mag arcsec $^{-2}$, M1La, M2La, M2Lb) for a total of six different models (we always assume $M/L_B = 2$ for the stellar disk and set the halo core radius equal to the disk scale length; see de Blok & McGaugh 1997). The GR8 model was obtained by rescaling model M1La for $z = 2$. The disk scale-length r_h is only 76 pc for GR8, while those of the other models are, respectively, 1.3 or 2 kpc (HSBs) and 1.5, 3.2 or 4.8 kpc (LSBs). The total mass-to-light ratios at $3r_h$ (close to the peak of the rotation curves) are, respectively, 6 (HSBs), 12 (LSBs) and 32(GR8).

3. EVOLUTION OF DWARF GALAXIES

As the Milky Way halo is modeled as an external potential, dynamical friction is neglected, which is a good approximation for satellites ~ 100 times less massive than the primary halo (Colpi et al. 1999). Satellites start at the virial radius of the primary (their apocenter) as if they were infalling for the first time, moving on orbits whose ratio between apocenter and pericenter ranges from 4 to 10, in agreement with simulations of galaxy and cluster formation (Ghigna 1998). Orbital periods are typically of the order of 3 – 4 Gyr, but are as short as 1 – 2 Gyr in the run with GR8, because this model was evolved in a Milky Way potential scaled down in size and mass as expected at $z = 2$. The inclination and spin of the disk relative to the orbital plane are randomly selected. In total 40 different runs were performed.

3.1. Dynamical Evolution

As the dwarfs approach pericenter (typically of 40–70 kpc) LSBs lose most of their dark matter halo and stars, due to their low density halos and large disks, and become weakly bar unstable. HSBs suffer modest stripping and their more self-gravitating disks develop a strong bar. The GR8 model is barely stripped owing to its very dense halo and its small disk radius. Minimal stripping keeps its disk more self gravitating compared to the structurally similar LSB and thus a fairly strong bar can develop after the second pericenter passage. Mass stripping for the various models is reflected in the evolution of their circular velocity profiles (Figure 1).

After completion of 2–3 orbits in 7 Gyr, our “tidally stirred” dwarf galaxies bear a striking resemblance to the real dSphs (right panel in Figure 2): direct tidal heating coupled with the buckling of the bar due to bending instabilities (Raha et al. 1991) transmute the small disks into spheroids supported by velocity dispersion instead of rotation (Figure 3). The GR8-like dwarf, falling into the Milky Way halo around redshift 2, suffers several (5) strong tidal shocks by the present time and is thus transformed despite being extremely compact.

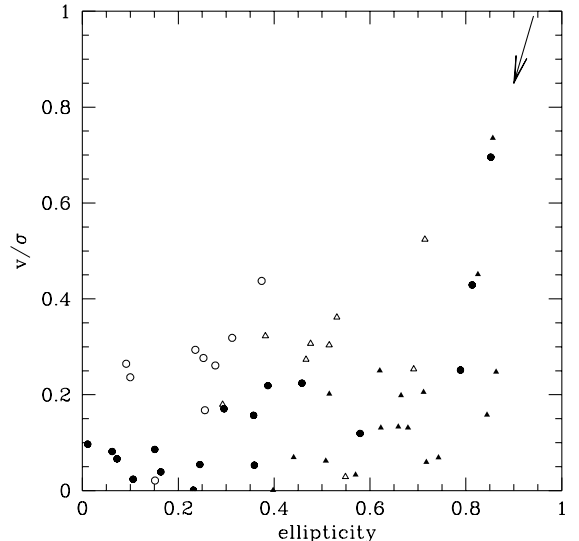


Fig. 3.— The final v/σ normalized to the initial value is plotted against the final ellipticity for 26 different runs. For each final state we show the measurements for a line-of-sight aligned with the major axis of the remnant (circles) and with the intermediate axis of the remnant (triangles). Minor axis projections are not shown because rotation along the other two axes is negligible. Filled symbols are for LSBs, open symbols are for HSBs. The arrow starts at the coordinates of the initial states of all the satellites and shows the direction of evolution. The ellipticity is either $1 - c/b$ or $1 - c/a$ (with a, b and c being, respectively, the major, intermediate and minor axis of the remnants) depending on the projection.

On average the final v/σ (i.e. the ratio of the rotational to random velocity) inside the half mass radius R_e drops mean values ≤ 0.5 and σ varies in the range $7 - 35$ km s $^{-1}$, as observed for dSphs and dEs in the LG (Ma98). The largest of these values are typical of HSB remnants and are comparable to the velocity dispersion measured for the dEs associated to M31 (Ma98; Kormendy 1987). Only when the satellite is initially in retrograde rotation with respect to its orbital motion we measure a final v/σ still close to 1. The surface brightness profiles remain close to exponential (Figure 1), although with a smaller scale-length (typically by a factor of ~ 2). The remnants of HSBs exhibit a more pronounced steepening of the profile inside R_e because stars more efficiently lose angular momentum due to the strong bar instability. A From this set of more than 40 runs a clear trend emerges: *LSBs evolve into objects resembling dSphs while HSBs transmute into dEs*.

3.2. Gasdynamics and star formation history

Dwarf irregular galaxies have in general extended gaseous disks with an average total HI-to-stellar mass ratio larger than one (Hoffman et al. 1996): however, within the optical radius ($\sim 3 r_h$), the neutral hydrogen fraction often drops to only 50% of the stellar mass (Jobin & Carignan 1990; Cote et al. 1990). In some of our model galaxies we include a gaseous disk of 20,000 particles which only extends out to the radius of the stellar disk (material lying outside this radius is entirely stripped according to the col-

lisionless runs) and whose mass is 30% of the total baryonic mass (the gas density drops to zero at a radius $R < 0.5r_h$ to mimic the “holes” found in many dIrrs). The dynamics of gas are implemented using an SPH scheme and radiative cooling for a primordial mixture of hydrogen and helium (Wadsley et al. 2000). The initial temperature of the gas is set at 5000 K.

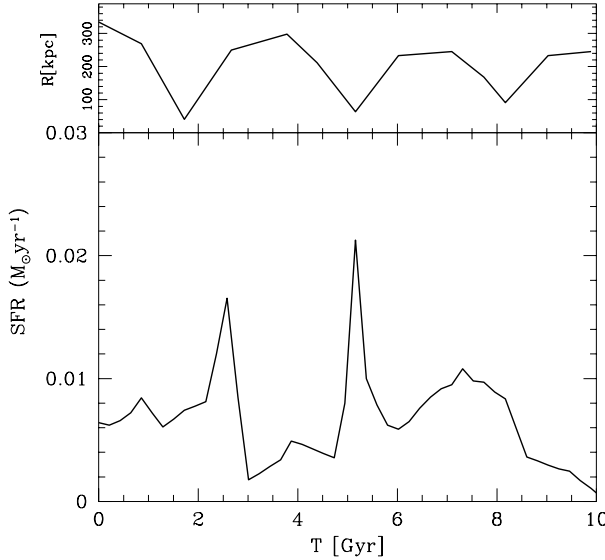


Fig. 4.— Star formation history for an LSB dwarf We assume that the dwarf enters the Milky Way halo 10 Gyr ago ($t=0$ is the present time). The evolution of the radial orbital oscillation is also shown in the small panel on top.

We place an LSB satellite (model M2La) on a 9:1 orbit: $\sim 50\%$ of the gas is stripped after two pericenter passages and is never reaccreted, while the rest is torqued by the weak bar and gradually flows to the center: the surface density profile of the gas bound to the system steepens remarkably at each pericenter passage due to tidal compression and torques. We then use the Kennicutt’s law (Kennicutt 1998) to determine the star formation rate from the gas surface density. We also take into account the reduction of the gas mass as it is converted into stars. The resulting star formation history has two main peaks roughly separated by the orbital time of the dwarf (~ 3.5 Gyr) (Figure 4), as recently found for Leo I and Carina (Hernandez et al. 2000). After 10 Gyr the star formation is suppressed because of gas consumption. The stronger bar instability in an HSB (model M2H) placed on the same orbit funnels more than 80% of the gas to the center at the first pericentric passage, giving rise to a starburst ten times stronger than the bursts in the LSB and using up all the gas in ~ 2 Gyr. As the strength of the bar instability seems to determine the type of star formation history, including gas in the GR8 model would lead to a result qualitatively similar to that of the HSB. Interestingly, in the LG both the dEs and the extreme dSphs like Draco and Ursa Minor formed the bulk of their stellar population during a single early episode (Ma98; Gr99).

Finally we convolve the star formation history with the passive luminosity evolution of the stellar component resulting from population synthesis models (Bruzual & Charlot 1993) for low-metallicity systems (1/4 of the so-

lar value). The multiple bursts are modeled as decreasing exponential laws with amplitude and time constants constrained by the numerical results. The resulting total B band luminosities and stellar mass-to-light ratios of the final remnants are in good agreement with those of observed dSphs.

4. DISCUSSION

Figure 5 summarizes the main observable properties of the simulated satellites projecting them on the Fundamental Plane (FB94). The remnants of LSB satellites resemble dSphs like Fornax or Sagittarius ($-14 < M_B < -11$), while HSBs transform in the bright dEs ($M_B > -17$), having a final central surface brightness higher than that of observed dIrrs with the same luminosities and therefore matching another observational constraint (FB94; Ma98). The total (including dark matter) final mass-to-light ratios are in the range 6 – 20. Remarkably, our model can reproduce the properties of even the most extreme dSphs, Draco and Ursa Minor. In fact, as the dark matter halo of GR8 is barely affected by tides (Figure 1), the remnant ($M_B = -7.5$) has a final mass-to-light ratio still ~ 50 and the central dark matter density is still around $0.3 M_\odot \text{ pc}^{-3}$, matching the structural parameters inferred for Draco and Ursa Minor (Ma98).

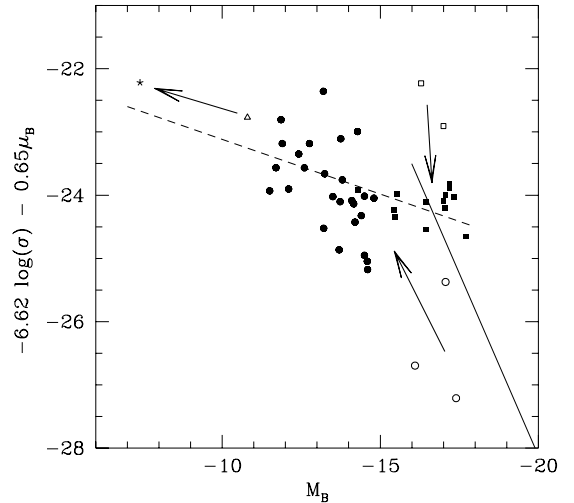


Fig. 5.— Fundamental Plane (FP) for all the remnants as in Ferguson & Bingeli (1994) (bottom). In the FP plot, μ and σ are, respectively, the average surface brightness and velocity dispersion measured inside R_e and M_B is measured at the Holmberg radius. The dashed line is a fit to the distribution of local dSphs, while the solid line refers to elliptical galaxies within the Virgo cluster (Dressler et al. 1987). Open and filled symbols represent, respectively, the initial and final state of HSBs (squares) and LSBs (circles). The initial and final state of the GR8 model are indicated by the open triangle and “star”.

“Tidal stirring” naturally leads to the spatial segregation of dIrrs versus dSph as its effectiveness depends strongly on the distance from the primary. How important is our assumption of a massive and extended dark

matter halo surrounding the Milky Way ? When we adopt a “minimal” dark halo truncated at 50 kpc (with mass $5 \times 10^{11} M_{\odot}$; Little & Tremaine 1987), tides are too weak and the final remnants are still rotationally flattened ($v/\sigma > 1$). Instead, within a halo as massive and extended as implied by theories of galaxy formation (Peebles 1989) , our dIrrs models transform into dSphs even on orbits with apocenters larger than 200 kpc, explaining the origin of even the farthest dSphs as Leo I and Leo II.

Though rather speculative at this stage, it is tempting to relate HSB satellites observed during the strong bursting phase to the population of blue compact dwarfs identified by Guzmán et al. (1997) at intermediate redshift. Redshift surveys will establish if bursting dwarfs have nearby massive companions.

Extended tidal streams of stars originate from our simulated dwarfs (Fig. 2) with a maximum surface brightness

of just 30 mag arcsec $^{-2}$ (B band). Spectroscopic evidence for stellar streams from the dSph Carina has been recently claimed (Majewski et al. 2000). Future astrometric missions, like SIM and GAIA (Gilmore et al. 1998; Helmi et al. 1999) should reveal such faint features and will also carry out high-quality measurements of proper motions for many satellites of the Milky Way, thus providing a test for the orbital configurations used in this model.

Our model successfully explains the origin of dSphs once all observational constraints are taken into account: they evolved from dIrrs that entered the halo of the Milky Way or M31 several Gyr ago moving on plunging orbits and suffered stirring by the tidal field of the large spirals.

The authors thank G.Bothun for stimulating discussions. Simulations were carried out at the CINECA (Bologna) and ARSC (Fairbanks) supercomputing centers.

REFERENCES

- Bruzual G., & Charlot S. 1993, ApJ, 405, 538
 Carignan, C., Beaulieu, S., & Freeman, K.C. 1990, AJ, 99, 178
 Colpi, M., Mayer, L., & Governato, F. 1999, ApJ, 525, 720
 Cote, S., Freeman, K.C., & Carignan C. 1997, ASP conference series, Vol. 117, p.52
 de Blok, W.J.G., & McGaugh, S. S., 1997, MNRAS, 290, 533
 Dekel, A., & Silk, J. 1986, ApJ, 303, 39
 Dikaiakos, M., & Stadel, J. 1996, Conf. Proc. of the International Conference on Supercomputing (New York: Assoc. for Computing Machinery)
 Einasto, J., Saar, E., Kaasik, A., & Chernin, A. D. 1974, Nature, 252, 111-1
 Faber, S.M., & Lin, D.N.C. 1983, 266, ApJL, 266
 Ferguson, H.C., & Binggeli, B. 1994, AAR, 6, 6
 Ghigna, S., Moore, B., Governato, F., Lake, G., Quinn, T., Stadel, J. 1998, MNRAS, 300, 146
 Gilmore, G.F. et al. 1998, Proc. SPIE, 3350, 541
 Grebel, E.K. 1999 IAU Symp. 192, Cape Town, in press, eds. White-lock, P. & Cannon (Gr99)
 Guzmán, R. et al. 1997, ApJ, 489, 559
 Helmi, A., White, S.D.M., de Zeeuw, P., & Zhao, H. 1999, Nature, 402, 53
 Hernandez, X., Gilmore, G., & Valls-Gabaud, David. 2000, to appear in MNRAS [astro-ph/0001337]
 Hernquist, L. 1993, ApJS, 86, 289
 Hoffman, G.L., Salpeter, E.E., Farhat, B., Roos, T., Williams, H. & Helou, G., 1996, ApJ, 105, 269
 Irwin, M., & Hatzdimitriou, D. 1995, MNRAS, 277, 1354
 Jobin, M., & Carignan, C. 1990, AJ, 100, 648
 Kennicutt, R.C.Jr. 1998, ApJ, 498, 541
 Klypin, A., Kravtsov, A.V., Valenzuela, O., & Prada, F. 1999, ApJ, 522, 8
 Kormendy, J. 1985, ApJ, 295, 73
 Lacey, C., & Cole, S. 1993, MNRAS, 262, 627
 Lake, G., 1990, MNRAS, 244, 701
 Little, B., & Tremaine, S. 1987, ApJ, 320, 493
 Majewski, S.R., Ostheimer, J.C., Patterson, R.J., Kunkel, W.E., Johnston, K.V., & Geisler, D. 2000, AJ, 119, 760
 Mateo, M. 1998, ARAA, 36, 435 (Ma98)
 Mo, H.J., Mao, S., & White, S.D.M. 1998, MNRAS, 296, 847
 Moore, B., Katz, N., Lake, G., Dressler, A., & Oemler, A.Jr. 1996, Nature, 379, 613
 Moore, B., Lake, G., & Katz, N. 1998, ApJ, 495, 139
 Moore, B., Ghigna, S., Governato, F., Lake, G., Quinn, T., Stadel, J., & Tozzi, P. 1999, ApJL, 524, L19-L22
 Murali, C. 2000, ApJL, 529, L81
 Peebles, P.J.E., Melott, A.L., Holmes, M.R., & Jiang, L.R. 1989, ApJ, 345, 1989
 Raha, N., Sellwood, J.A., James, R.A., & Kahn, F.D. 1991, Nature, 352, 411
 Van den Bergh, S. 1996, PASP, 108, 986
 Van den Bergh, S. 1999, AAR, 9, 273
 Wadsley, J., Quinn, T., & Stadel, J. in preparation
 Wilkinson, M.I., & Evans, N.W. 1999, MNRAS, 310, 645
 Zwaan, M. A., van der Hulst, J.M., de Blok, W.J.G., & McGaugh, S. S. 1995, MNRAS, 273, L35

Lopsided galaxies in a cosmological context: a new galaxy–halo connection

Silvio Varela-Lavin^{ID, 1,2*} Facundo A. Gómez^{ID, 1,2*} Patricia B. Tissera^{ID, 3,4} Gurtina Besla^{ID, 5}, Nicolás Garavito-Camargo^{ID, 6} Federico Marinacci^{ID, 7} and Chervin F. P. Laporte^{ID, 8,9,10}

¹Departamento de Física y Astronomía, Universidad de La Serena, Av. Juan Cisternas 1200 Norte, La Serena, Chile

²Instituto de Investigación Multidisciplinar en Ciencia y Tecnología, Universidad de La Serena, Raúl Bitrán 1305, La Serena, Chile

³Instituto de Astrofísica, Pontificia Universidad Católica de Chile, Av. Vicuña Mackenna 4860, Santiago, Chile

⁴Centro de Astro-Ingeniería, Pontificia Universidad Católica de Chile, Av. Vicuña Mackenna 4860, Santiago, Chile

⁵Steward Observatory, University of Arizona, 933 North Cherry Avenue, Tucson, AZ 85721, USA

⁶Center for Computational Astrophysics, Flatiron Institute, 162 Fifth Avenue, New York, NY 10010, USA

⁷Department of Physics and Astronomy ‘Augusto Righi’, University of Bologna via Gobetti 93/2, I-40129 Bologna, Italy

⁸Departament de Física Quàntica i Astrofísica (FQA), Universitat de Barcelona (UB), c. Martí i Franquès, 1, E-08028 Barcelona, Spain

⁹Institut de Ciències del Cosmos (ICCUB), Universitat de Barcelona (UB), c. Martí i Franquès, 1, E-08028 Barcelona, Spain

¹⁰Institut d’Estudis Espacials de Catalunya (IEEC), c. Gran Capità, 2–4, E-08034 Barcelona, Spain

Accepted 2023 May 26. Received 2023 May 24; in original form 2022 November 22

ABSTRACT

Disc galaxies commonly show asymmetric features in their morphology, such as warps and lopsidedness. These features can provide key information regarding the recent evolution of a given disc galaxy. In the nearby Universe, up to ~ 30 per cent of late-type galaxies display a global non-axisymmetric lopsided mass distribution. However, the origin of this perturbation is not well understood. In this work, we study the origin of lopsided perturbations in simulated disc galaxies extracted from the TNG50 simulation of the IllustrisTNG project. We statistically explore different excitation mechanisms for this perturbation, such as direct satellite tidal interactions and distortions of the underlying dark matter distributions. We also characterize the main physical conditions that lead to lopsided perturbations. 50 per cent of our sample galaxy have lopsided modes $m = 1$ greater than ~ 0.12 . We find a strong correlation between internal galaxy properties, such as central stellar surface density and disc radial extension with the strength of lopsided modes. The majority of lopsided galaxies have lower central surface densities and more extended discs than symmetric galaxies. As a result, such lopsided galaxies are less self-gravitationally cohesive, and their outer disc region is more susceptible to different types of external perturbations. However, we do not find strong evidence that tidal interactions with satellite galaxies are the main driving agent of lopsided modes. Lopsided galaxies tend to live in asymmetric dark matter haloes with high spin, indicating strong galaxy–halo connections in late-type lopsided galaxies.

Key words: galaxies: evolution – galaxies: formation – galaxies: haloes – galaxies: interactions – galaxies: spiral – galaxies: structure.

1 INTRODUCTION

In the nearby Universe, spiral galaxies, such as our own, show different morphological asymmetries such as warps, lopsidedness and polar rings, among others. Lopsided perturbations in disc galaxies are one of the most common. It is described as a morphological distortion in which a side of the disc is more elongated than the other. Such global non-axisymmetric perturbation is typically quantified through a Fourier decomposition of the mass or light distribution, focusing on the $m = 1$ mode, A_1 (Rix & Zaritsky 1995; Quillen et al. 2011). Rix & Zaritsky (1995) showed that, for lopsided galaxies, the amplitude of A_1 increases with radius in the outer galaxy regions. Clear examples of lopsided galaxies include M101 or NGC1637.

One of the first studies reporting this perturbation was presented by Baldwin, Lynden-Bell & Sancisi (1980), who analysed the spatial distribution of H I gas in the outer regions of a sample of galaxies.

Lopsidedness has been studied in the stellar (Rix & Zaritsky 1995) and H I gas distributions (Richter & Sancisi 1994; Haynes et al. 1998) of galaxies, as well as on their large-scale kinematics (Schoenmakers, Franx & de Zeeuw 1997; Swaters et al. 1999; Khademi et al. 2021), and compared against numerical models (Ghosh et al. 2022; Łokas 2022). In the nearby Universe, 30 per cent of late-type galaxies show high values of A_1 (Zaritsky & Rix 1997; Bournaud et al. 2005). On the other hand, for early-type galaxies the frequency with which this perturbation arises is close to 20 per cent (Rudnick & Rix 1998). This higher frequency of lopsidedness in late-type galaxies was confirmed by Conselice, Bershady & Jangren (2000), who analysed a sample of 113 galaxies both early- and late-type. Lopsidedness in this sample was quantified using the 180° rotational asymmetry measure, A_{180} . They found a strong relation between morphology and lopsidedness, showing that early-type galaxies (elliptical and lenticular) tend to systematically have lower values of A_{180} .

A more recent study from Reichard et al. (2008, hereafter R08) measured the asymmetries in galaxies through A_1 using their surface brightness (SB) distribution in three different bands. Their sample

* E-mail: silvio.varela@userena.cl (SL); fagomez@userena.cl (FG)

consisted of more than 25 000 galaxies from Sloan Digital Sky Survey (SDSS). They showed that the occurrence and strength of lopsidedness has a strong dependence with galaxy structural properties. Disc galaxies with higher A_1 tend to have low stellar mass, concentration, and high central stellar density. The latter is the parameter that most clearly correlates with the lopsidedness. As in Rix & Zaritsky (1995), R08 show that the amplitude of the $m = 1$ mode is negligible in the very inner regions of galactic discs due to its strong self-gravitating nature. However, a systematic increase of the A_1 parameter with galactocentric radius is observed in the outer galactic regions of lopsided galaxies. In addition, R08 find that the lopsided light distributions are primarily caused by lopsided distributions in the stellar mass.

As discussed by Jog & Combes (2009), lopsidedness can have very significant effects on the evolution of galaxies. In particular, for disc galaxies it can induce the redistribution of stellar mass due to angular momentum transport and the modulation of hosts star formation histories. In addition, the internal torques induced by such $m = 1$ modes can result in the loss of angular momentum by the host gaseous disc, thus affecting the growth of the central supermassive black hole. As a result, lopsided perturbations could allow us to place important constrains on the recent interaction history of galaxies.

Several studies that have tried to characterize the main mechanisms driving lopsided perturbations. Possible proposed mechanism are minor mergers (Walker, Mihos & Hernquist 1996; Zaritsky & Rix 1997; Ghosh et al. 2022) and tidal interactions due to close encounters between galaxies of similar mass (Kornreich, Lovelace & Haynes 2002). Indeed, low-density galaxies and, in particular, the outskirts of galactic disc, are likely to be more susceptible to tidal stress. However, a study of 149 galaxies observed in the near-infrared (near-IR) from the OSUBGS sample (Eskridge et al. 2002) by Bournaud et al. (2005) found that the amplitude of the $m = 1$ mode is uncorrelated with the presence of companions. Instead, they suggested that asymmetric gas accretion is an important driver of lopsidedness. Similarly, Łokas (2022) used a sample of simulated galaxies extracted from the TNG100 simulation of the IllustrisTNG project (Nelson et al. 2019a) to study the origin of these perturbations. They concluded that the most frequent mechanism for the formation of lopsided discs is asymmetric star formation, probably related to gas accretion. However, they also observed that the distortions in the gas and stars were not strongly correlated.

Another plausible mechanism driving lopsided discs relates to perturbations in the density field of the underlying galactic dark matter (DM) halo. These asymmetries in a DM halo could be produced by a resonant interaction between the DM halo particles and an orbiting satellite. The resulting asymmetry of the DM overdensity field, or wake, can be thought of as a superposition of different modes excited by such resonant interaction. The wake's associated torque, exerted on the embedded disc, could lead to the formation of strong morphological disturbances such as lopsidedness and warps, among others. Indeed, Weinberg (1998) showed that such perturbations can induce the formation of vertical patterns, such as warps and corrugation patterns. These results were later confirmed using fully cosmological hydrodynamical simulations (Gómez et al. 2016) as well as carefully tailored simulations to study the response of the Milky Way (MW) halo to a recently accreted Large Magellanic Cloud satellite (Laporte et al. 2018a; Garavito-Camargo et al. 2019). Furthermore, as discussed by Jog (1999), these DM halo asymmetries can also induce the formation of lopsided perturbations, and sustain them for long periods of time. Using the Millennium simulation (Springel et al. 2005), Gao & White (2006) characterized asymmetries in DM haloes within a mass range of

$\sim 10^{12}\text{--}10^{15} \text{ M}_\odot$. The asymmetries were quantified based on shifts between the overall DM halo centre of mass (CoM) and its centre of density (cusp). Shifts between the system's CoM and cusp can be though as the dipolar component of a wake (Weinberg 1998; Garavito-Camargo et al. 2021), and typically have the strongest amplitude of all modes. They showed that such asymmetries were not uncommon and that the frequency with which they arose depended on the host mass. While 20 per cent of cluster haloes have CoM separated from their cusp by distances larger than 20 per cent of the virial radius, only 7 per cent of the MW mass haloes show such large asymmetries.

Despite all these studies, several questions remain to be answered regarding lopsided galaxies, including the main driver and longevity of such perturbation. Additionally, we do not yet understand whether lopsidedness can be linked to fundamental properties of the structure and evolution of the host galaxy and its halo. In this work, we analyse a large sample of late-type galaxies, extracted from the Illustris TNG50 project (Pillepich et al. 2019; Nelson et al. 2019a) to shed light on these issues. This highly resolved fully cosmological hydrodynamical simulation includes, in a self-consistent manner, the different physical processes that have been proposed as the main drivers of morphological perturbations. In particular, we focus on MW mass-like haloes, whose stellar disc can be resolved with the available mass resolution. In Section 2, we discuss the details of the numerical simulation, as well as the selection criteria for our galaxy sample. The methods to characterize the properties of the stellar discs, and to quantify the presence of a lopsided mode on their density distribution, are introduced in Section 3. In Section 4, we present our results. Our conclusion and discussion are summarized in Section 5.

2 SIMULATIONS

In this section, we introduce the numerical simulations considered in this work, which are taken from the Illustris-The Next Generation project (IllustrisTNG hereafter; Marinacci et al. 2018; Naiman et al. 2018; Nelson et al. 2018, 2019a; Pillepich et al. 2018; Springel et al. 2018). We also describe the criteria applied to select galaxies from the corresponding large cosmological boxes.

2.1 The IllustrisTNG project

The IllustrisTNG project is a set of gravo-magnetohydrodynamics cosmological simulation, run with the moving-mesh code AREPO (Springel 2010). It comprises three large simulation volumes: TNG50, TNG100, and TNG300, enclosing volumes of $\sim 50^3$, 100^3 , and 300^3 cMpc , respectively. All these TNG runs follow the standard Lambda cold dark matter model, with parameters based on the Planck Collaboration XIII (2016) results: $\Omega_m = 0.3089$, $\Omega_\Lambda = 0.6911$, $\Omega_b = 0.0486$, $h = 0.6774$, $\sigma_8 = 0.8159$, $n_s = 0.9667$, with Newtonian self-gravity solved in an expanding Universe. The IllustrisTNG¹ is the successor of the Illustris project (Genel et al. 2014; Vogelsberger et al. 2014a, b; Nelson et al. 2015), containing updated models for the physical processes that are relevant for galaxy formation and evolution (Weinberger et al. 2017; Pillepich et al. 2018), such as radiative cooling, stochastic star formation in dense interstellar stellar medium, and an updated set of sub-grid physics models for stellar evolution, black hole growth, stellar and active galactic nucleus (AGN) feedback.

¹<https://www.tng-project.org>

Table 1. Main parameters of the TNG50 simulation: the comoving volume and the box side-length (first and second rows), the number of initial gas cells and DM particles (second to fourth rows), the mean baryonic and DM particle mass resolution (fourth to sixth rows), the minimum allowed adaptive gravitational softening length for gas cells (comoving Plummer equivalent) (seventh row) and the redshift zero softening of the collisionless components (eighth row).

Run name	TNG50	
Volume	(cMpc ³)	51.7 ³
L_{box}	(cMpc h ⁻¹)	35
N_{GAS}	–	2160 ³
N_{DM}	–	2160 ³
m_{baryon}	(M _⊙)	8.5×10^4
m_{DM}	(M _⊙)	4.5×10^5
$\epsilon_{\text{gas,min}}$	(pc)	74
ϵ_{DM}	(pc)	288

In this work, we focus on the model TNG50-1 (Pillepich et al. 2019; Nelson et al. 2019b) and its DM-only counterpart. TNG50-1 (hereafter TNG50) is the highest resolution run within the TNG project. Its high resolution allows us to better analyse the azimuthal distribution of stellar mass in the outskirts of MW-like galaxies. In Table 1, we list the main parameters of this simulation.

The TNG50 data base provides a catalogue of magnitudes in eight bands (SDSS g , r , i , z ; Buser U , B , V ; and Palomar K) for each stellar particle. To estimate them, each stellar particle is assumed to represent a single stellar population of a given age and metallicity, consistent with a Chabrier IMF (Chabrier 2003). Their spectral energy distributions are obtained from the Bruzual & Charlot (2003) populations synthesis models (e.g. Tissera, Lambas & Abadi 1997). We note that possible effects by dust obscuration have not been considered.

2.2 Selection criteria

In this work, we seek to characterize the properties and main physical mechanism that give rise to disc galaxies displaying a non-axisymmetric global mass distribution of type $m = 1$, better known as lopsided galaxies (Jog & Combes 2009).

We built our sample focusing on host late-type galaxies embedded in DM haloes with a M_{200} between $10^{11.5}$ and $10^{12.5}$ M_⊙, where M_{200} is defined as the total mass of the halo enclosed in a sphere whose mean density is 200 times the critical density of the Universe at $z = 0$. We considered only central galaxies, so we do not consider satellites within our sample. To properly quantify lopsidedness in the galaxies outskirts, we selected well-resolved galaxies with more than 10 000 stellar particles, identified and assigned to each host by the SUBFIND algorithm (Springel et al. 2001). Finally, we selected disc-dominated galaxies by requiring the disc-to-total mass ratio (D/T) to be greater than 0.5. This last parameter was extracted from a catalogue provided by Genel et al. (2015), and represents the fractional stellar mass within $10 \times R_{50}$ ² with a circularity parameter $|\epsilon| > 0.7$. That last parameter is defined as $\epsilon = J_z/J(E)$, where J_z is the angular momentum component perpendicular to the disc plane of a stellar particle with orbital energy E , and $J(E)$ is the (estimated) maximum possible angular momentum for the given E in a circular orbit (Tissera, White & Scannapieco

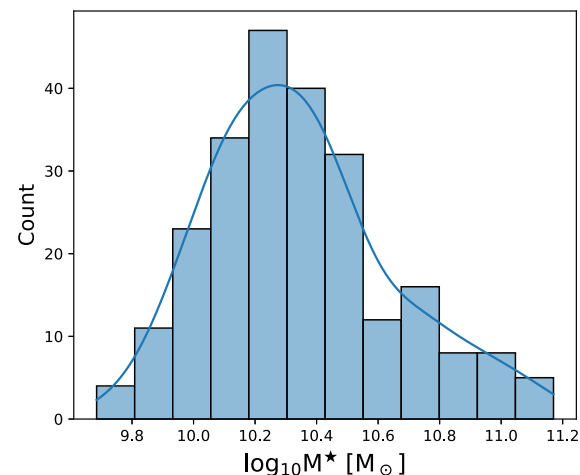


Figure 1. Stellar mass distribution of our selected sample (see Section 2.2). The solid line depicts a KDE of this distribution.

2012). That last selection about D/T place a strong limit on the mass contribution of the spheroidal components to the simulated galaxies.

After applying the selection criteria, the final sample comprises 240 late-type galaxies at $z = 0$. In Fig. 1, we show the total stellar mass distribution of the selected sample. The stellar mass distribution of our TNG50 sample ranges from $10^{9.5}$ to $10^{11.2}$ M_⊙. The mean stellar mass of our galaxy sample is $\sim 10^{10.3}$ M_⊙. In Section 4.5, we expand our sample to compare with previous results from the literature. Only for this purpose, we select central haloes with M_{200} ranging from 10^{11} to 10^{13} M_⊙.

3 METHODS

3.1 Characteristic scales

To measure asymmetries in the mass and light distribution of the disc component of our simulated galaxy suite, it is important to define the different radial scales within which the analysis will be performed. In our work, these characteristic scales are estimated by using the projected stellar mass and light on to the rotational plane of the disc. First, we generate radial SB profiles in the V photometric band. The SB profiles are created through the binning of the luminosity distribution of the stellar particles in radial annuli of 0.5 kpc of width. For better accuracy, we have smoothed the SB profile with a polynomial fit. This smoothed profile is used to define the position outermost edge of the disc, $R_{26.5}$, as the radius where the SB profile falls to a magnitude of 26.5 mag arcsec⁻². $R_{26.5}$ is also known as optical radius, and here it is used as a proxy of the size of galaxies. The $R_{26.5}$ in our TNG50 sample are within the range [9.5, 46.75] kpc with a median of 22.53 kpc. In Fig. 2, we show examples of four lopsided and four symmetric disc galaxies in our sample (top and bottom panels, respectively). In this figure, we also illustrate the sizes of the galaxies as measured by $R_{26.5}$ (white dashed circles), illustrating how well this parameter traces the size of disc galaxies with different characteristics.

From now on, we consider all star particles located within a sphere of radius $R_{26.5}$, to estimate the parameters in this sub-section. We define the stellar half-mass radius, R_{50}^* , as the position that enclosed the 50 per cent of stellar mass, M_{50}^* , of the corresponding disc. Similarly, we define R_{90}^* as the position that enclosed 90 per cent

²The stellar half-mass radius, R_{50} , is defined as the radius that encloses 50 per cent of the total stellar mass of a subhalo.

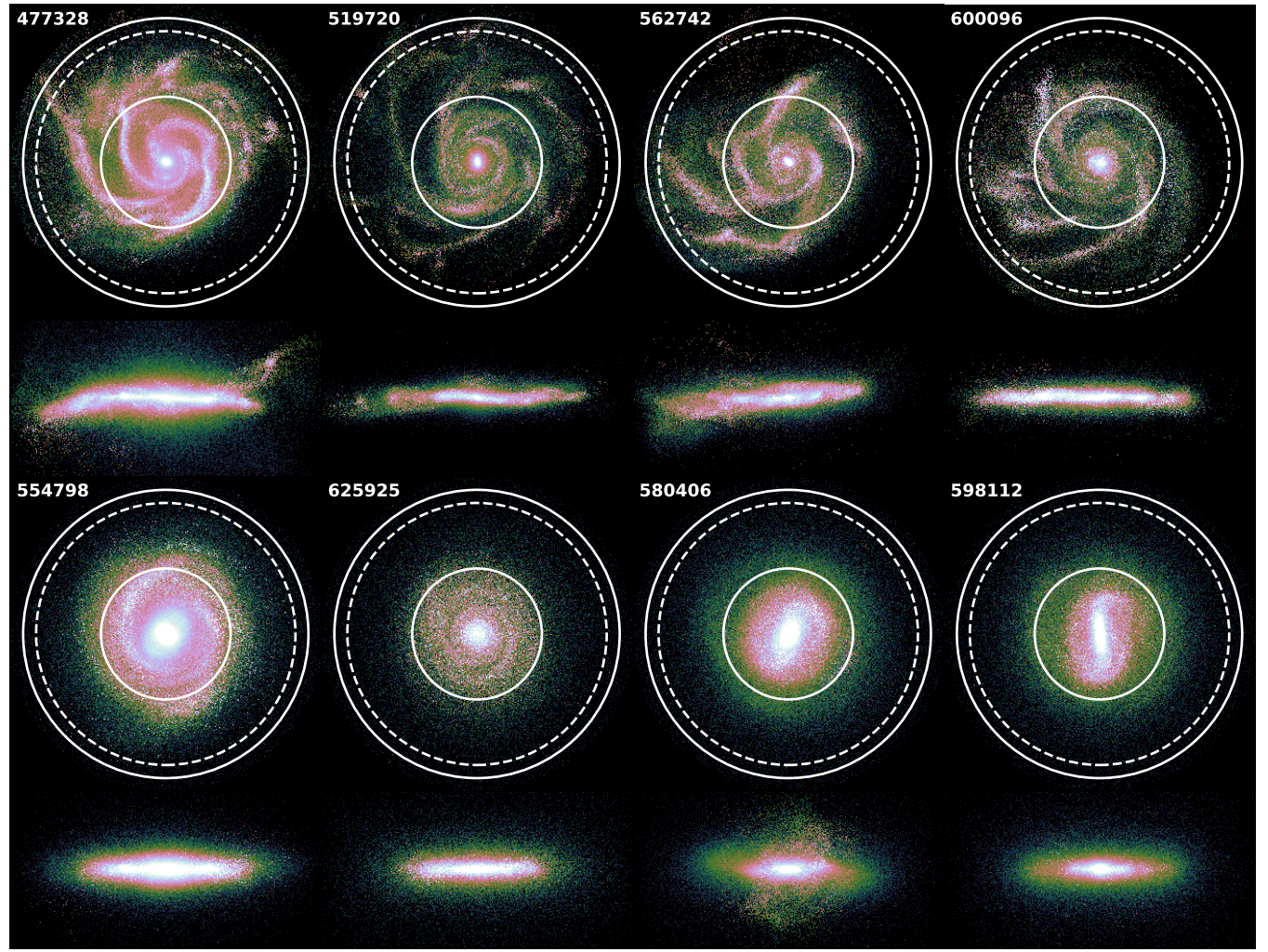


Figure 2. Face-on and edge-on projected stellar density for eight galaxies from our TNG50 sample at $z = 0$. The images at the top correspond to the most lopsided galaxies while those at the bottom to the most symmetrical ones. The dashed circles indicate $R_{26.5}$. The solid circles represent the lower and upper radial limit considered to compute A_1 , which are between $0.5R_{26.5}$ and $1.1R_{26.5}$, respectively. More details in Section 3.2.

of the disc stellar mass, M_{50}^* . We find that R_{50}^* varies between 2.02 and 13.69 kpc with a median of 6.57 kpc, while R_{90}^* varies within 5.91 and 36.26 kpc, with a median of 15.81 kpc. These parameters allow the estimation of the stellar concentration defined as $C_* = R_{90}^*/R_{50}^*$, and central stellar density, $\mu_* = M_{50}^*/\pi R_{50}^{*2}$.

3.2 Quantification of $m = 1$ asymmetries

In order to quantify the asymmetry in the mass and light distributions of the disc stellar component of our galaxies, we adopt the Fourier mode approach (Rix & Zaritsky 1995; Zaritsky & Rix 1997; Quillen et al. 2011; van Eymeren et al. 2011; Grand et al. 2016). In particular, we focus our analysis on lopsided perturbations, which can be characterized as a displacement of the centre of stellar mass with respect to its centre of density. Such asymmetric perturbations can be quantified through the amplitude of the $m = 1$ Fourier mode.

Within a given thin radial annulus, R_j , the complex coefficients of the m Fourier mode can be estimated from a discrete distribution as

$$C_m(R_j) = \sum_i^N M_i^* e^{-im\phi_i}, \quad (1)$$

where M_i^* and θ_i are the mass and azimuthal coordinate of the i th stellar particle that belongs to the j th radial annulus in a given galaxy. The angle ϕ_i is defined as $\phi_i = \text{atan2}(y_i, x_i)$, where x_i and y_i are the Cartesian coordinates of the i th stellar particle for galaxies oriented in a face-on configuration.³ Then, we define the amplitude of m th Fourier mode as

$$B_m(R_j) = \sqrt{a_m(R_j)^2 + b_m(R_j)^2}, \quad (2)$$

where a_m and b_m are the real and imaginary part of C_m (equation 1). The amplitude $B_1(R_j)$ corresponds to the strength of the $m = 1$ mode within a given j th radial annulus. Finally, since each radial annulus has a different total stellar mass, we express $B_1(R_j)$ relative to the corresponding $m = 0$ mode,

$$A_1(R_j) = \frac{B_1(R_j)}{B_0(R_j)}, \quad (3)$$

³ $\text{atan2}(0)$ is a function of two parameters that returns the phase angle of the position of a i th star particle in the respective quadrant, thus phase angles have values within the range $-\pi$ to π .

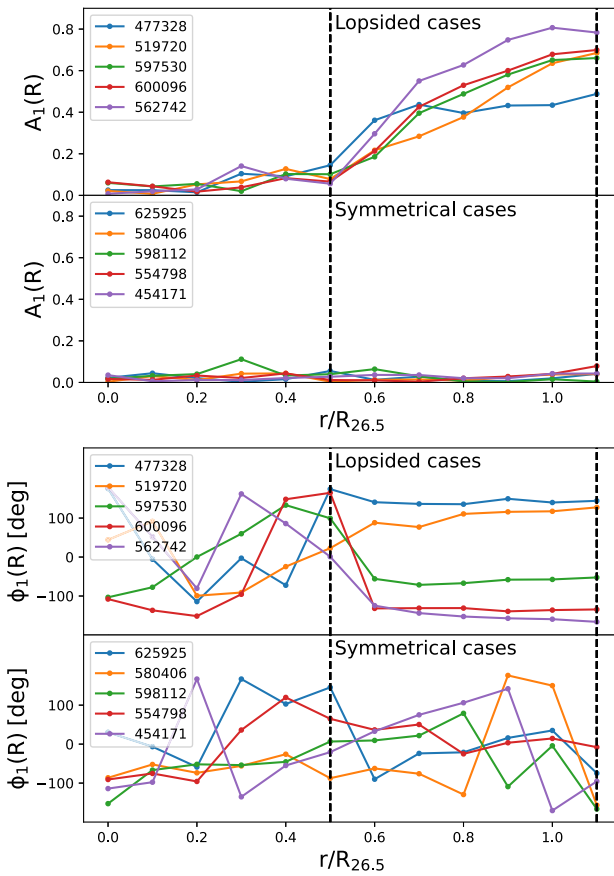


Figure 3. Top panel: Radial distribution of the amplitude $m = 1$ Fourier mode ($A_1(R)$), for five galaxies lopsided of A_1 (top sub-panel) and five symmetric galaxies (bottom sub-panel). The black dashed lines indicate the lower and upper radial limits considered to compute a global mass-weighted mean of $m = 1$ Fourier amplitudes, A_1 for each galaxy. Note that lopsided cases show an increase of $A_1(R)$ when increasing radius, and for symmetrical cases $A_1(R)$ approaches zero in the whole galaxy (see Section 3.2). Bottom panel: Radial distribution of phase angle of the $m = 1$ component, $\phi_1(R)$. Similar to the top panel, we show five lopsided and symmetrical disc examples. The lopsided galaxies show a nearly constant phase angle in their outer disc, in agreement with previous studies (Li et al. 2011; Zaritsky et al. 2013).

where B_0 is given by equation (2) for $m = 0$, and it is equal to the total mass in the given j th radial annulus. Thus, equation (3) corresponds to the mass-weighted amplitude of the $m = 1$ Fourier mode as a function of radius.

In Fig. 3, we show the radial A_1 profile (top panel) obtained from five of our most lopsided (top sub-panel) and five of our most symmetrical models (bottom sub-panel). We note that all galaxies, independently of whether they are lopsided or not, show very small A_1 values within $R \sim 0.5 R_{26.5}$. However, for lopsided galaxies, A_1 starts to rapidly increase after this galactocentric distance. The radial distribution of $A_1(R)$ in our model is similar to that found in Rix & Zaritsky (1995), who used near-IR observations from a sample of 18 galaxies to characterize the properties of lopsided galaxies. Rudnick & Rix (1998) and Bournaud et al. (2005) also found that the amplitude of the lopsided perturbations increases steadily ($A_1 > 0.1$) within the outer disc regions (radial range of $\approx 1.5\text{--}2.5$ exponential disc scale lengths). Jog (2000) suggested that the self-gravitational potential of the galaxy exerts a resistance to some external gravitational

perturbation. However, the resilience exerted by self-gravity is more significant at smaller radii, and indeed the values of $A_1(R)$ are low in the inner disc. For lopsided galaxies, the gravitational pull by self-gravity is weaker at larger radii, so $A_1(R)$ grows. Otherwise, the symmetric cases could be gravitationally more cohesive, and consequently the radial distribution of $A_1(R)$ keeps lower values in the whole disc. In Section 4.3, we explore this in detail.

In the bottom panel of Fig. 3, we show the radial phase angle of the $m = 1$ component, $\phi_1(R)$. Note the nearly constant value of $\phi_1(R)$ in the outer disc for lopsided examples, region where the corresponding asymmetry becomes significant. This feature is typical in lopsided galaxies (Zaritsky & Rix 1997; van Eymeren et al. 2011; Ghosh et al. 2022). The radial variation of $\phi_1(R)$ is a useful tool for understanding the nature of the lopsidedness and how long it takes to wind around the galaxy (Baldwin et al. 1980). Previous results (Saha, Combes & Jog 2007; Ghosh et al. 2022) suggest that, in lopsided galaxies, the outer galaxy region does not wind up as quickly as their inner region, suggesting a weak self-gravity in these galaxies.

Since the outer region of galactic discs is more prone to developing lopsidedness, we estimate, for each galaxy, a unique global mass-weighted mean of the $m = 1$ Fourier mode, hereafter A_1 . This allows us to compare the level of lopsidedness among galaxies in our sample. The global A_1 is computed by taking the mean of the $A_1(R)$ in outer galaxy regions. We consider eight radial annular regions, of width $0.075R_{26.5}$, located within the interval $0.5R_{26.5}$ to $1.1R_{26.5}$. This region is highlighted by the dashed lines in Fig. 3 and the solid circles shown in Fig. 2).

3.3 Estimating the asymmetries in DM haloes and stellar component

In this work, we are interested in characterizing the origin and evolution of lopsided perturbations. A possible mechanism triggering such perturbation is the response of the galactic disc to a distorted DM halo. As discussed in Section 1, these halo distortions arise as a result of interactions between the host DM particles and an external agent (Jog 1997, 1999; Gao & White 2006; Gómez et al. 2016; Laporte et al. 2018b). To quantify such distortions in the DM halo of our numerical models, we focus on offsets of the halo CoM with respect to its density cusp. Typically, the dipolar response of the DM halo density field is the strongest. Thus, it can be used to identify perturbed DM distributions.

Here, we follow the analysis performed by Gao & White (2006). First, we identify the DM halo density cusp, r_{cusp} , based on the position of the most bound particle of the central halo, given by SUBFIND. We then computed the DM halo CoM, r_{DM} , considering all DM particles located within the inner three and five times $R_{26.5}$. We note that, as shown by Gómez et al. (2016), perturbations in the DM halo at further galactocentric distances are not efficient at disturbing the embedded galactic disc. None the less, to compare with Gao & White (2006) we also compute r_{DM} considering all DM particles assigned to the main host halo by SUBFIND (R_{200}). Finally, we compute the offset of r_{DM} with respect to r_{cusp} as

$$\Delta r_{\text{DM}}^i = |r_{\text{cusp}} - r_{\text{DM}}^i|, \quad (4)$$

where the supra index $i = 3R_{26.5}, 5R_{26.5}$, and R_{200} indicates the spatial region within which r_{DM} is calculated.

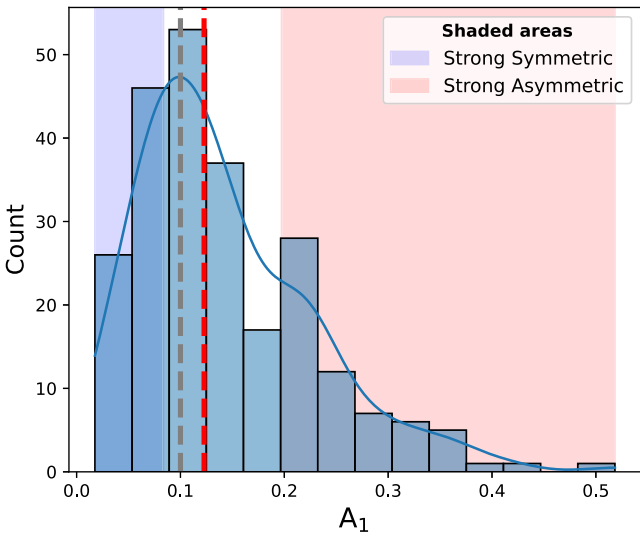


Figure 4. Distribution of the sample of global (mean) A_1 parameter computed for each simulated galaxy in our sample at $z = 0$. The solid blue line shows the A_1 distribution built using KDE method. The dashed red line is the median of A_1 distribution, $\hat{A}_1 \approx 0.12$, which is used to differentiate between symmetric and asymmetric galaxies, the grey dashed line corresponds to 0.1 threshold, typically used to define lopsided galaxies, note that $\hat{A}_1 > 0.1$, this means that a little more than half of our sample has $A_1 > 0.1$ values. The blue and red shaded areas indicate the first and fourth quartiles of the distribution, used to define the sub-sample of strong symmetric and asymmetric groups, respectively.

4 RESULTS

4.1 General disc morphological properties

In this section, we analyse the main morphological characteristics of the 240 stellar discs, selected according to the criteria defined in Section 2. In Fig. 4, we show the distribution of the global A_1 parameter, which correspond to the average $A_1(R)$ values computed within the radial range $[0.5–1.1R_{26.5}]$ (see Section 3.2). We note that the distribution is similar to the one reported by R08 (see their fig. 10), obtained using a sample 25 155 galaxies from the SDSS. It is worth noting that, even though the stellar mass range of our sample (Fig. 1) is similar to that in R08 ($10^8–10^{11} M_\odot$, see fig. 8 in R08), the latter includes a population of early-type galaxies, which are missing from our sample. None the less, the R08 sample is dominated by late-type objects, allowing us to compare our results with the data. The characteristic galaxy A_1 values in R08 were obtained by averaging over the radial range between R_{50} and R_{90} . The outer radius limit is imposed due to limitation with the observational data (see section 2.2 of R08 for more details). We have computed our distribution considering smaller outer limits, finding no significant variation in our results. Similar results were obtained by previous works such as Rix & Zaritsky (1995) and Bournaud et al. (2005).

The red dashed line in Fig. 4 indicates the median of the A_1 distribution, which takes a value of $\hat{A}_1 \approx 0.12$. This \hat{A}_1 is used from now on to differentiate galaxies between symmetric ($A_1 < \hat{A}_1$) and asymmetric or lopsided cases ($A_1 > \hat{A}_1$). We note that this value is only slightly larger than the 0.1 threshold, typically used to define lopsided discs (Zaritsky & Rix 1997; Bournaud et al. 2005; Jog & Combes 2009). We further subdivide our sample into strongly symmetric and asymmetric cases by selecting galaxies located in the first and fourth quartiles of the A_1 distribution, respectively. The strong cases are highlighted in Fig. 4 with shaded areas.

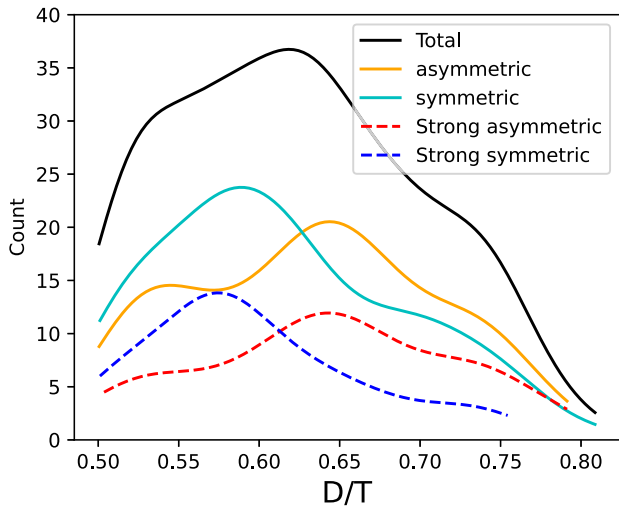


Figure 5. Distribution of disc-to-total mass ratio, D/T , for the total sample (black line), only asymmetrical galaxies (orange line), and only symmetrical galaxies (cyan). The red and blue dashed lines correspond to strong asymmetric and symmetric sub-samples, respectively. The distribution was obtained using a KDE method. Asymmetrical galaxies tend to be more disc dominated than their symmetrical counterpart. The medians for each group are 0.61 and 0.64, respectively. A similar trend is observed for the strong sub-samples.

We now explore whether there are correlations between the D/T (see Section 2.2) of our simulated galaxies and the symmetry of their azimuthal mass distribution. We recall that the parameter D/T allows the quantification of the disc mass contribution to the galaxy's total stellar mass. The black solid line in Fig. 5 shows the D/T density distribution obtain using the kernel density estimation (KDE)⁴ of the D/T values obtained from our full sample. Note that our selection criteria imposes a lower D/T limit of 0.50. The distribution has a median value of ≈ 0.62 , indicating a significant presence of strongly disc-dominated galaxies in our sample. Interestingly, asymmetric galaxies tend to be more disc dominated than their symmetric counterparts, with medians of 0.64 and 0.61, respectively. The blue and red dashed lines show the same distribution, now for the strong asymmetric and symmetric samples. The difference in the median D/T values is slightly more pronounced than in the previous sub-samples, with values of 0.64 and 0.58 for the asymmetric and symmetric sub-samples, respectively. This suggests that the presence of more significant central pressure-supported component could be playing a role on limiting the strength of lopsided perturbations. This is further explored in Section 4.3.

4.2 Structural properties of lopsided galaxies

As discussed in the previous section, our sample of disc-dominated galaxies show different degrees of lopsided asymmetry, as quantified by the value of their A_1 parameter. In this section, R_{50}^* , stellar mass concentration, C_* , and central stellar surface density, μ_* , present significant differences between the asymmetric and symmetric sub-samples.

To highlight the main differences between the asymmetric discs and their symmetrical counterparts, we focus on the strongly sym-

⁴We implement KDE using the GAUSSIAN_KDE function from the SCIPY library. More details can be found at <https://scipy.org>

metric and strongly asymmetric galaxy samples defined in Fig. 4. The top left panel of Fig. 6 shows the distribution of R_{50}^* and μ_* . The distributions are represented with a two-dimensional KDE. The top and the right sub-panels show the marginalized 1D distribution for R_{50}^* and μ_* , respectively. Interestingly, both strong types show different distributions in this plane. We find that asymmetric galaxies tend to have larger R_{50}^* than their symmetric counterparts. In addition, they tend to show lower values of μ_* at given R_{50}^* . These differences are highlighted on the 1D KDE, with median values of R_{50}^* and μ_* for the symmetric and asymmetric sub-samples of (4.62, 7.22) kpc and $(10^{8.39}, 10^{7.75}) M_\odot \text{ kpc}^{-2}$, respectively.

Following R08, in the middle and bottom panels we show 2D KDE of our simulated galaxy sample in μ_* versus total stellar mass, M^* , and in M^* versus stellar concentration, C_* , respectively. R08 show that, among these structural parameters, the strongest correlation with A_1 is obtained for μ_* . Indeed, our results are in good agreement with these observations. Note that the most pronounced difference between the distributions of these strong types is obtained for μ_* . The marginalized C_* distribution (bottom panel) shows that both types of galaxies present nearly indistinguishable distribution of stellar concentration. Interestingly, within the stellar mass range considered in this work, we find that symmetric galaxies tend to be slightly more massive than lopsided galaxies. In addition, the lopsided sub-sample shows a narrower distribution in M^* . To quantify these results, we estimate Pearson correlation coefficient between the previously defined parameters. In Table 2, we show both the correlation coefficients obtained using only the strong samples and also using all lopsided and symmetrical galaxies (fourth column). As previously indicated, the strongest (anti)correlation is obtained between A_1 and μ_* . This significant anticorrelation is obtained for both the strong and the complete samples.

4.3 The role of the central mass distribution

As discussed in the previous section, our sample of galactic models shows a significant correlation between A_1 and the central stellar density, μ_* . Galaxies with lower μ_* typically show higher values of A_1 . Additionally, we also find that lopsided galaxies tend to show larger values of R_{50}^* . This suggests that galaxies with lower density and more extended central regions could be more prone to develop lopsided perturbations.

Indeed, discs with denser inner regions are likely to be more gravitationally cohesive. To explore whether the disc self-gravity plays a significant role in the onset and amplitude of lopsided perturbations, we show, in Fig. 7, the distribution of $M_{50}/R_{26.5}^3$ versus μ_* for all galaxies in the strong symmetric and asymmetric samples. Here, M_{50} represents the total mass of all particles enclosed in a sphere of radius R_{50}^* , and includes contributions from the stellar, the gas, and the DM components. We note that the quantity $M_{50}/R_{26.5}^3$ represents a proxy of the tidal force exerted by the inner galaxy region ($R < R_{50}^*$) on material located a distances equal to the disc optical radius, $R_{26.5}$. As before, we focus on the strong symmetric and asymmetric types. From this figure, we observe that these two subgroups represent very distinct populations in $M_{50}/R_{26.5}^3$ versus μ_* space. Present-day asymmetric galaxies exert a much lower tidal field on their outer disc regions, where lopsided perturbations show the strongest amplitudes. This is clearly shown on the 1D KDE histogram displayed in the top panel. Indeed, the (anti)correlation between A_1 and $M_{50}/R_{26.5}^3$ is the strongest among the structural parameters explored in this work. This is quantified in Table 2, which also highlights that this anticorrelation is even greater than the one found between A_1 and μ_* . We emphasize that the anticorrelation is not limited to the

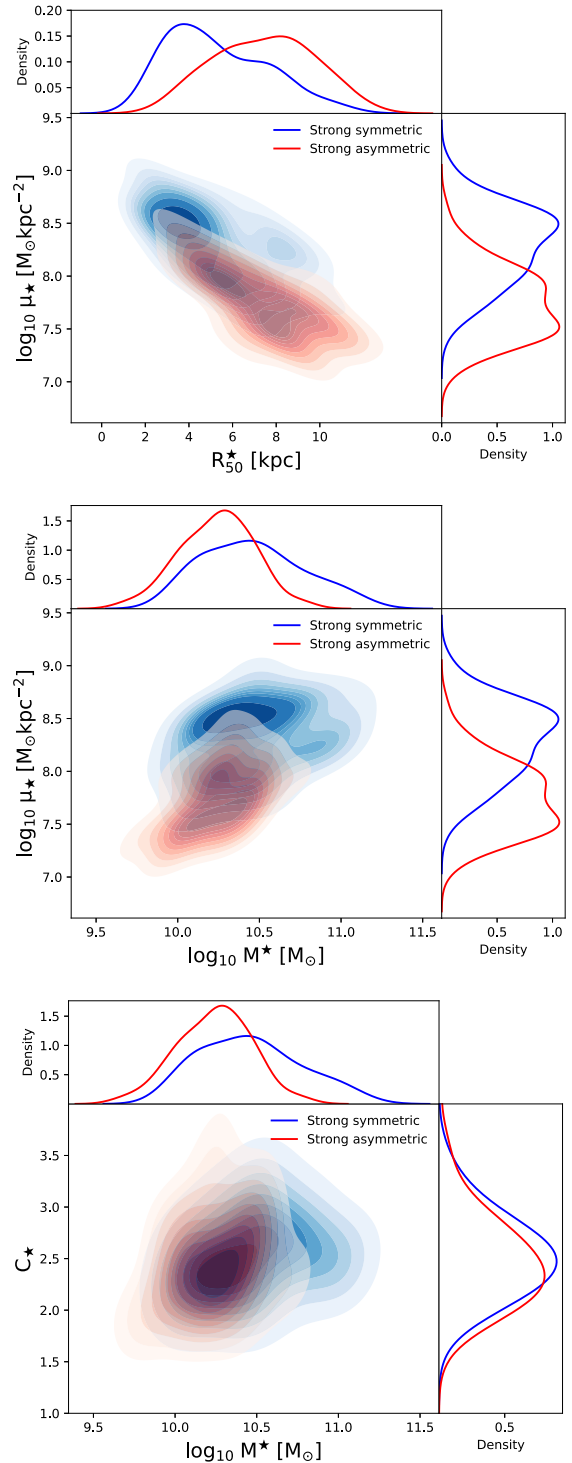


Figure 6. Top panel: Central stellar density, μ_* , as a function of stellar half-mass radius, R_{50}^* , for the strong symmetric and asymmetric sub-samples that are defined in Fig. 4. Middle panel: μ_* as a function by the total stellar mass, M_{90}^* . Bottom panel: Stellar mass concentration, C_* , as a function M_{90}^* . These panels were built using KDE bivariate distribution for the central sub-panel, and simple KDE distribution for edge sub-panels. The strong sub-sample was separated between strong symmetric (blue region) and strong asymmetric (red region). Note that strong asymmetric galaxies tend to have their central regions more extended and slightly less massive than symmetric galaxies. Furthermore, a clear difference between both sub-samples are in their central stellar density, where in asymmetric galaxies tend to be lower ones.

Table 2. Correlations coefficients for relations between the analysed parameters discussed in Sections 3.3 and 4.3.

P1	P2	Correlation coefficient	
		Strong sample	All sample
$\log_{10} A_1$	$\log_{10} \mu_*$	−0.68	−0.54
$\log_{10} A_1$	R_{50}^*	0.53	0.37
$\log_{10} A_1$	C_*	−0.03	−0.01
$\log_{10} A_1$	$\log_{10} M_{50}/R_{26.5}^3$	−0.72	−0.60
$\log_{10} \mu_*$	$\log_{10} M_{50}/R_{26.5}^3$	0.60	0.52

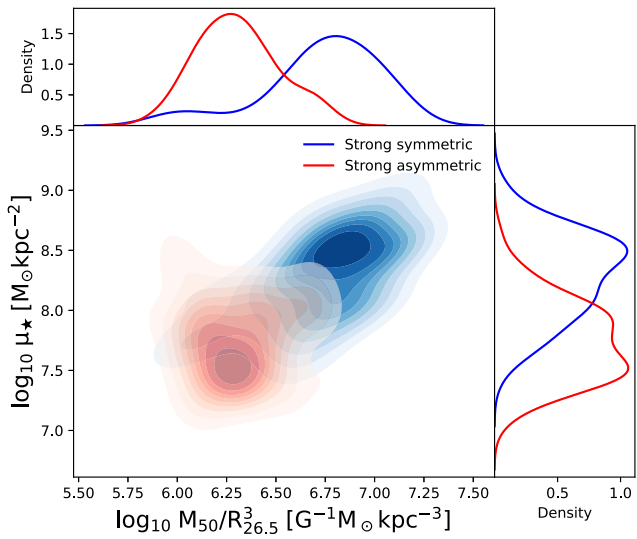


Figure 7. Distribution of the proxy of the tidal force exerted by the inner disc on its outskirts, $M_{50}/R_{26.5}^3$, versus central stellar density, μ_* , for all galaxies in the strong symmetric and asymmetric samples. The top and right-hand panels show the corresponding one-dimensional distribution. All distributions were obtained using a KDE method. A clear correlation between μ_* and $M_{50}/R_{26.5}^3$ is seen. Strong asymmetric galaxies tend to have a lower values of $M_{50}/R_{26.5}^3$, suggesting that weakly gravitationally cohesive galaxies are susceptible to lopsided distortions in their stellar distribution.

strong subtypes, and that it remains large even if we consider the all galaxies in the sample, as can be seen from the rightmost column of Table 2.

Several previous studies have explored different scenarios for the origin of lopsided modes based on environmental interactions, such as fly-bys, minor and major mergers, perturbed underlying DM density field, and misaligned accretion of cold gas, among others (Weinberg 1994; Walker et al. 1996; Jog 1997, 1999; Zaritsky & Rix 1997; Levine & Sparke 1998; Noordermeer, Sparke & Levine 2001; Kornreich et al. 2002; Bournaud et al. 2005; Gómez et al. 2016; Garavito-Camargo et al. 2019). Our results instead hint towards a population of galaxies susceptible to develop lopsidedness, and not to a particular external perturbation source. In other words, galaxies with weakly cohesive inner regions could develop a lopsided mode when faced with any sort of external perturbation. Indeed, as we show later in Section 4.5, the strong present-day connection between the strength of the lopsided modes and of the inner tidal force field is independent of the past interaction history of our simulated galaxies with their environment.

4.4 Evolution of lopsided galaxies

Around 30 per cent of late-type galaxies in the nearby Universe show lopsided perturbations (Rix & Zaritsky 1995; Jog & Combes 2009). This could indicate that either lopsided perturbations are long lived, or that a significant fraction of galaxies are prone to develop such perturbations even in absence of significant external interactions, as suggested in the previous section. Here, we explore the time evolution of the main structural parameters that differentiate symmetric and lopsided galaxies, as well as the time evolution of the amplitude of the lopsided mode.

4.4.1 Time evolution of structural parameters

As previously discussed, lopsided galaxies tend to show lower values of μ_* as well as larger R_{50}^* at the present-day. In Fig. 8, we explore how these structural parameters evolved over time. As before we focus on the strong types to better highlight the differences between perturbed and unperturbed galaxies. The top panel shows the time evolution of the central stellar surface density, μ_* , over the last 6 Gyr. The blue and red solid lines depict the median μ_* obtained after stacking the strong asymmetric and symmetric sub-samples, respectively. The shaded areas are determined by the 25th and 75th percentiles of both distributions. It is interesting to note that, at the present-day, the difference in μ_* is very significant, and that this difference increased over the last 6 Gyr. In particular, we notice a significant decay of μ_* over time for the strong lopsided cases, while for the symmetric counterparts μ_* remain nearly constant. To understand what is behind this decay, we show in the middle panel of Fig. 8 the time evolution of the stellar mass enclosed within the stellar half-mass radius, M_{50}^* . We notice that, on average, lopsided galaxies tend to enclose less stellar mass within R_{50}^* . However, the difference in M_{50}^* between symmetric and asymmetric galaxies remains nearly constant over the last 6 Gyr. This is in contrast for the time evolution of R_{50}^* , shown in the bottom panel. Note that 6 Gyr ago, both sub-samples had, on average, very similar values of R_{50}^* . However, lopsided galaxies experienced a significant growth of R_{50}^* while, for symmetric galaxies, it remained nearly constant, specially over the last 3 Gyr.

The previous analysis shows that what drives the decay of μ_* for lopsided galaxies is mainly the growth of the stellar disc size. Using the Auriga simulations, Grand et al. (2017) investigated the mechanisms that set present-day disc sizes, and found that they are mainly related to the angular momentum of halo material. In their models, the largest discs are produced by quiescent mergers that inspiral into the galaxy and deposit high angular momentum material into the pre-existing disc. This process simultaneously increases the spin of DM and gas in the halo. On the other hand, early violent mergers and strong AGN feedback strongly limit the final disc size by destroying pre-existing discs and by suppressing gas accretion on to the outer disc, respectively. Interestingly, they find that the most important factor that leads to compact discs, however, is simply a low angular momentum for the halo. To explore whether the halo spin, λ (see equation 12, Grand et al. 2017) plays a role on the development of lopsided galaxies by partially setting the size of the disc and thus their radial mass distribution, in Fig. 9 we show the distribution of λ versus $M_{50}/R_{26.5}^3$ for galaxies in our sample. The colour coding indicates the strength of the A_1 mode. Interestingly, we find that galaxies with high λ typically show smaller values of $M_{50}/R_{26.5}^3$ and high values of A_1 . On the other hand, galaxies with low λ values are dominated by strongly self-gravitating discs and, thus, low A_1 values. Interestingly, using the EAGLE and Fenix simulations, Cataldi et al. (2021) reported that haloes with less concentration

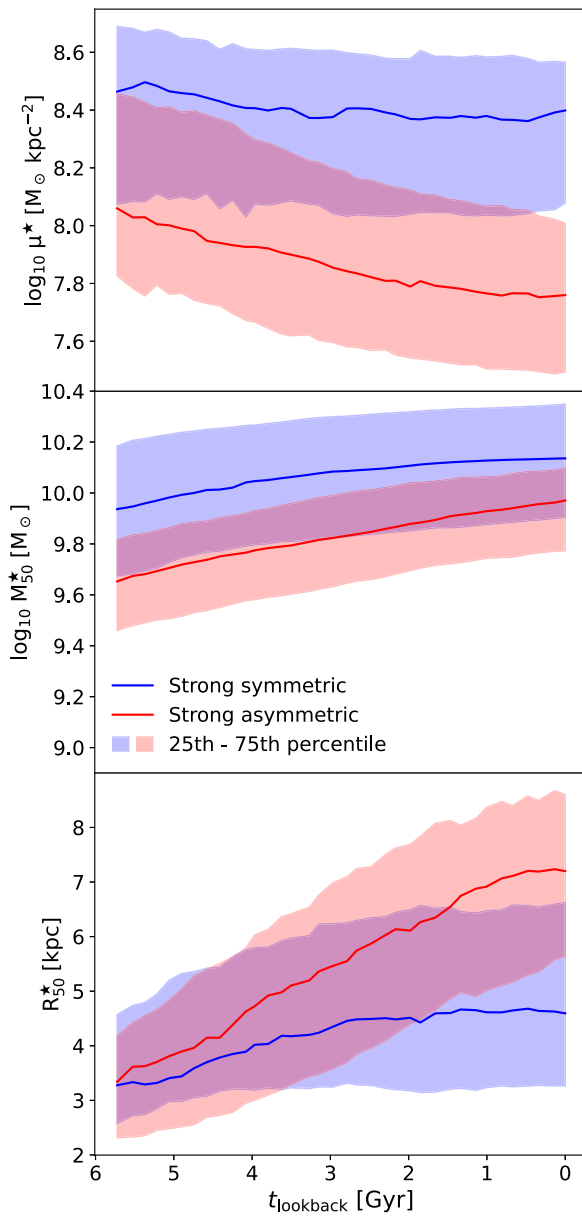


Figure 8. Time evolution of the central stellar density, the stellar half-mass, and stellar half-mass radius (from top to bottom). Quantities are shown as a function of lookback time. The solid blue and red lines show the median of the distributions obtained from the strong symmetric and asymmetric sub-samples, respectively. The shaded areas indicate the 25th and 75th percentiles of the corresponding distributions. The central stellar density evolution of the strong asymmetric sub-sample tend to have a sharp decrease in time compared to strong symmetric sub-sample. This is a consequence of the rapid growth of R_{50}^* over time.

tend to host extended galaxies. These results highlight an interesting morphology–halo connection for late-type galaxies.

4.4.2 Frequency of A_1

As previously discussed, Fig. 4 shows that, at the present-day, a 62 per cent of our simulated galactic discs are significantly lopsided ($A_1 > 0.1$). This suggest that this type of perturbations are either long lived (e.g. Jog & Combes 2009) or short lived, but repeatedly re-excited by subsequent perturbations (see e.g. Ghosh et al. 2022). We

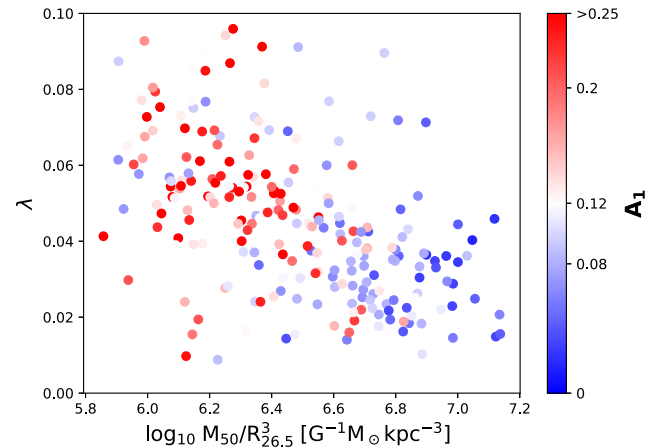


Figure 9. Distribution of halo spin parameter, λ , versus proxy of the tidal force exerted by the inner disc on its outskirts, $M_{50}/R_{26.5}^3$. The dots are coloured according to the present-day value of A_1 , which the palette of colours was centred around $\bar{A}_1 \sim 0.12$, while 0.08 and 0.2 values correspond to the 25th and 75th percentiles of A_1 distribution, used to define strong sub-sample. Note that asymmetrical galaxies tend to have higher halo spin than their symmetrical counterpart.

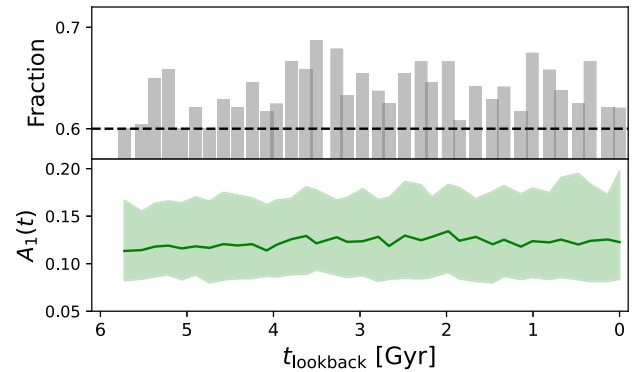


Figure 10. Top panel: Fraction of galaxies that show $A_1 > 0.1$ during the last 6 Gyr. Bottom panel: Distribution of A_1 in the sample in function of time. The green line corresponds to the median of A_1 and the green region covers the 25th to 75th percentile of the A_1 distribution. We see that the medians of A_1 are around 0.125 during the last 6 Gyr. Our sample show that the fraction of galaxies with high lopsidedness are between 60 and 70 per cent in that range of time.

explore this by following the time evolution of our simulated galaxies, and quantifying the fraction of time they present a significant lopsided perturbation over the last 6 Gyr. In practice, we proceed as follows. We identify our galactic models in the 36 snapshots available during the last 6 Gyr of evolution and compute, on each of them, the A_1 parameter. This parameter is calculated by fixing the value of $R_{26.5}$ at its present-day value. We have tested that our results do not significantly vary if we take into account the evolution of the optical radius. In Fig. 10, we explore the distribution of A_1 in our sample over the past 6 Gyr (bottom panel). The median of A_1 (green line) is around 0.125 during this period. The green region cover the 25th to 75th percentiles of the A_1 distribution of our sample, which does not exceed 0.2 for the 75th percentile and does not fall below 0.075 for the 25th percentile. In the top panel, we show the fraction of galaxies that display a high amplitude of $m = 1$ component ($A_1 > 0.1$), showing that around 60–70 per cent of the galaxies in our sample exhibit

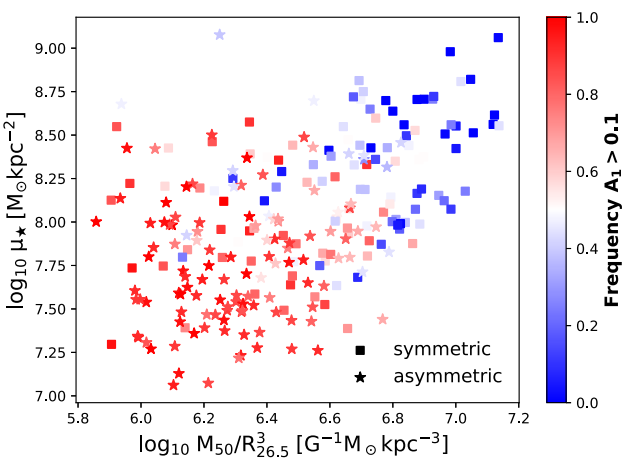


Figure 11. Distribution of the central stellar density versus $M_{50}/R_{26.5}^3$, which is a proxy of the tidal force exerted by the inner disc on its outskirts. Galaxies are separated between symmetric (square) and asymmetric (star), using A_1 at $z = 0$. The symbols are colour coded according to the fraction of time they experienced of significant lopsided perturbation ($A_1 > 0.1$) during the last 6 Gyr of evolution. Galaxies with lower $M_{50}/R_{26.5}^3$ tend to show lopsided distortions for longer periods. Interestingly, there are symmetric cases at the present-day that have spent long periods as lopsided (red squares). This galaxies typically show low $M_{50}/R_{26.5}^3$. Conversely, it is less common to see present-day lopsided galaxies with small $A_1 > 0.1$ frequency.

high lopsidedness during this time range. This suggests that lopsided perturbation is a very frequent phenomenon for disc galaxies.

Fig. 11 shows the distribution of galaxies in μ_* versus $M_{50}/R_{26.5}^3$ space, colour coded according to the fraction of time each simulated galaxies experienced $A_1 > 0.1$ within the last 6 Gyr. Present-day lopsided galaxies, defined as in Section 4.1, are shown with star symbols, whereas their symmetrical counterparts with square symbols. In general, we find that symmetric galaxies (high μ_* and $M_{50}/R_{26.5}^3$ values) show low A_1 values throughout the latest 6 Gyr of evolution. In other words, strongly gravitationally cohesive galaxies have remained symmetric over most of the corresponding period of time (blue colours). On the other hand, we find that lopsided galaxies (typically weakly gravitationally cohesive) have remained lopsided ($A_1 > 0.1$) over a significant fraction of the latest 6 Gyr (red colours). There are, however, several examples of galaxies that have been lopsided over most of this period, but at the present-day have a symmetric configuration (see red squares). Note as well that it is less common to find present-day lopsided galaxies with low frequency of A_1 .

Our results suggest that lopsided perturbations are typically long lived, rather than short lived but repeatedly re-excited. We further explore this in the following section, where we follow the time evolution of a number of representative galaxy models.

4.5 Main driving agents

As discussed in Section 1, several different mechanisms have been proposed as main driving agents for this type of morphological perturbation. The mechanisms range from direct tidal perturbations from relatively massive satellites, torques associated with perturbed underlying DM haloes, and the non-axisymmetric accretion of cold gas, among others. In this section, we explore whether there is a dominant mechanism driving lopsidedness in our simulated galaxies.

4.5.1 Individual examples

Before analysing the whole sample of galaxy models in a statistical manner, we first analyse in detail a couple of typical examples of present-day symmetric and lopsided galaxies.

We first focus on two examples of typical present-day symmetric galaxies. The top panels of Fig. 12 show that, as discussed in Section 4.4.1, symmetric galaxies typically do not experience a substantial growth in size over the last 6 Gyr of evolution. Both discs show nearly constant R_{50}^* and R_{90}^* values over this period of time. In the second panel (top to bottom), we show the time evolution of μ_* . As expected, both galaxies show μ_* values larger than the $z = 0$ median (red dashed line, $\hat{\mu}_* = 10^{7.98}$). In addition, μ_* show nearly constant values over this period of time. The large central surface density and small size render strong cohesiveness and thus resilience to perturbations. Indeed, as shown in the third panel, their A_1 value remains mainly below the \hat{A}_1 threshold, indicating that these galaxies have remained symmetric over most of this period. We note, however, that the evolution of A_1 shows moderate increments over short span of times. For example, for galaxy S1, A_1 rises over \hat{A}_1 at a lookback time, $t_{lb} \sim 5$ Gyr. To explore the origin of this short-lived lopsided mode, we quantify in the fourth and fifth panels the interaction of this galactic disc with its environment. We first look at the time evolution of the offset of the halo CoM with respect to its density cusp, Δr_{DM}^i (fourth panel). Interestingly, Δr_{DM}^i peaks during the same period. This is noticeable when considering DM particles up to a distance of $5R_{26.5}$. Note as well that this offset of the DM halo CoM is short lived and directly related to a strong tidal interaction with a massive satellite galaxy. This is shown in the bottom panel, where we show the time evolution of tidal field exerted on the host by its 10 most massive satellites as a function of time, i.e. $|a_{sat}| = GM_{sat}/R_{sat}^3$. Here, M_{sat} and R_{sat} are the total mass of the satellite and the distance between the satellite and its host galaxy. We notice that the galactic disc strongly interacts with a massive satellite ($M_{sat} \sim 10^{10} M_\odot$) at $t_{lb} \sim 5$ Gyr. This strong interaction is behind the brief distortion of the host outer DM halo, and the temporary onset of a mild A_1 perturbation. For this large μ_* simulated galaxy, and in agreement with Ghosh et al. (2022), the perturbation rapidly dissipates and the amplitude of the disc $m = 1$ mode remains below \hat{A}_1 for the rest of the period, even though a second significant interaction takes place later on ($t_{lb} \sim 2.5$ Gyr).

In the right-hand panels of Fig. 12, we analyse a second example, S2, of a present-day symmetric galaxy. As before, the galaxy shows small and nearly constant scale lengths over the whole the last 6 Gyr of evolution. It shows as well a nearly constant μ_* value, but with a value larger than in the previous example, S1. The A_1 parameter typically remains below \hat{A}_1 , except for short periods where it slightly raises over this threshold. When inspecting interactions with its environment, we observe that S2 experienced two very strong interactions with a satellite galaxy of $M_{tot} \approx 10^{10.5} M_\odot$. These interactions take place at $t_{lb} \approx 5.5$ and 1.5 Gyr (fifth panel), and both resulted in significant perturbations of the host DM halo (fourth panel). Yet, due to the large μ_* , no associated response is observed in the evolution of the A_1 parameter.

In Fig. 13, we now explore two examples of strongly lopsided galaxies, L1 and L2. The top panels show that, contrary to the symmetric cases, these galaxies experienced a consistent growth in size over the latest 6 Gyr, which resulted in a decrement of their μ_* . As a result, the central surface density of these simulated galaxies is significantly lower (second panels) than in the symmetric examples. The third panels show that, in both cases, A_1 has mainly

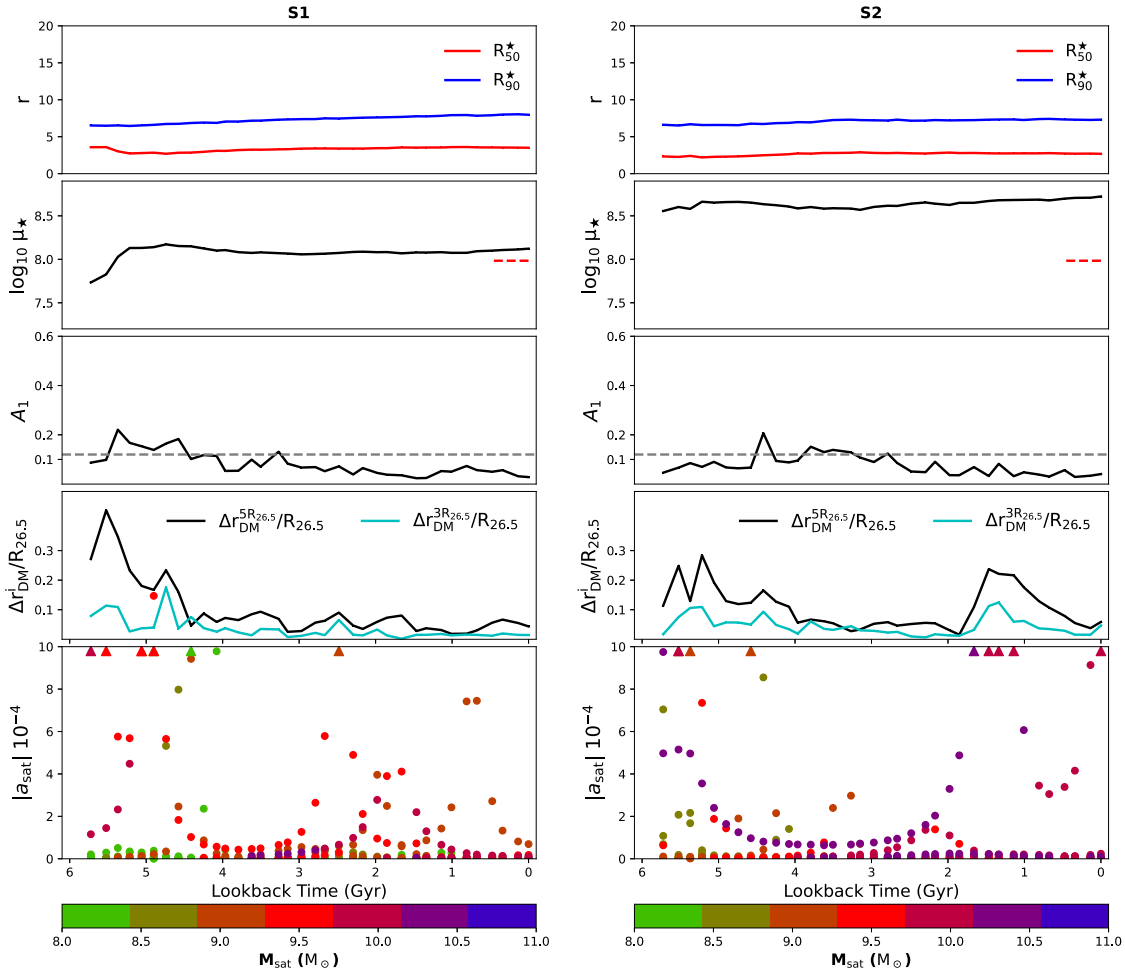


Figure 12. Examples of two typical present-day symmetric galaxies, S1 and S2. *From top to bottom:* First panel: Time evolution of the scale length parameters, R_{50}^* and R_{90}^* , during the last 6 Gyr of evolution. Second panel: Evolution of the central surface density, μ_* . The red dashed line on the right-hand side of each panel shows the corresponding present-day median of μ_* . Third panel: A_1 as a function of time. The black dashed line corresponds to the \hat{A}_1 threshold, extracted from the full sample distribution at $z = 0$. Fourth panel: Time evolution of the offset between the DM halo CoM and its density cusp, Δr_{DM}^i . We show the evolution of Δr_{DM}^i calculated within two spatial regions, $3R_{26.5}$ and $5R_{26.5}$ (see Section 3.3). Fifth panel: Time evolution of tidal field exerted on the host galaxy by its 10 most massive satellites. Triangles indicate tidal field values that are above the Y-axis limit. Symbols are colour coded as a function of the total mass of the corresponding satellite.

remained above our threshold, \hat{A}_1 , indicating long-lived lopsided modes. In particular, for L1 (left-hand panels), we find that the galaxy experienced a relatively strong tidal interaction with a satellite of $M_{\text{sat}} \sim 10^{10.5} M_\odot$ at $t_{\text{lb}} \approx 5$ Gyr. Due to the low values of μ_* , and contrary to the S1 case, this interaction excited a strong lopsided mode as well as a shift of the DM CoM with respect to its density cusp. The lopsided perturbation slightly wanes over time, but it always remains over \hat{A}_1 . At $t_{\text{lb}} \approx 2$ Gyr, the disc experienced a second significant tidal interaction ($M_{\text{sat}} \sim 10^{10} M_\odot$) that enhances the lopsided perturbation, raising the value of $A_1 \approx 0.35$ until the present-day. On the other hand, even though L2 (right-hand panels) shows a value of $A_1 > \hat{A}_1$ over most of the last 6 Gyr, it did not experience any significant interaction with massive satellites ($M_{\text{sat}} > 10^{10} M_\odot$). Interestingly, the CoM of outer DM halo shows a significant shift with respect to its cusp during this period, with values $\Delta r_{\text{DM}}^{5R_{26.5}}$ as large as 20 percent of $R_{26.5}$. Such perturbed DM halo could be behind the long-lived lopsided perturbation in this galactic disc (see e.g. Jog & Combes 2009). We will explore in detail this particular kind of models in a follow-up study.

4.5.2 Statistical characterization of the impact of interactions

In the previous section, we discussed two examples of stellar discs that interacted with their nearby environment and developed very strong lopsided perturbations. On the other hand, we also discussed examples of galaxies that strongly interacted with their environments but did not develop significant lopsided modes on their discs. The main difference between these two sets of objects is their central surface density, μ_* , which set the gravitational cohesiveness of the disc outskirts. In this section, we explore what are the main agents driving lopsided perturbations in low μ_* galaxies.

We start by quantifying significant tidal interaction with satellite galaxies within the last 6 Gyr of evolution. As in Section 4.5.1, for each galaxy in our sample, we compute $|a_{\text{sat}}|$ as function of lookback time. Based on Figs 12 and 13, and the results shown in Gómez et al. (2017), we first quantify the fraction of time galactic discs were exposed to $|a_{\text{sat}}| > 10$ from satellites with mass ratios $M_{\text{sat}}/M_{\text{host}} > 0.005$. Lower values of $|a_{\text{sat}}|$ do not yield to global perturbations in the discs. For a MW mass host, the chosen threshold in the mass ratio allows interaction with satellites of $M_{\text{sat}} \geq 10^{9.5}$

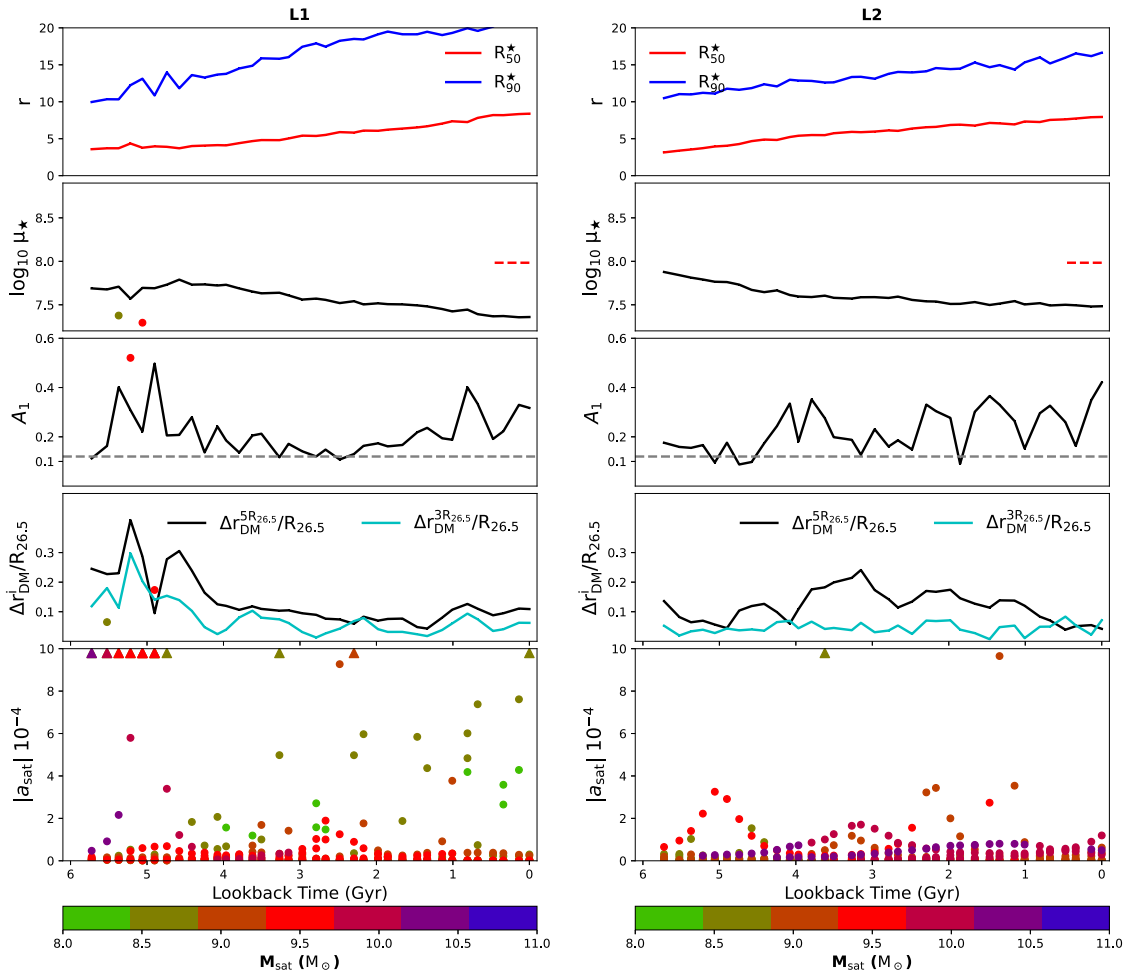


Figure 13. As in Fig. 12, for two typical present-day lopsided galaxies, L1 and L2.

M_\odot . Lower mass satellite are unlikely to induce significant global vertical perturbations (Gómez et al. 2017). Fig. 14 shows our sample of galactic discs in satellite interaction frequency versus $M_{50}/R_{26.5}^3$ space. Points are colour coded by the fraction of time each disc presents a significant lopsided perturbation (see Section 4.4.2). As before, we notice that galaxies with lower frequencies of $A_1 > 0.1$ (light colours) tend to have lower values of $M_{50}/R_{26.5}^3$. Interestingly, we find no significant correlation between the fraction of time galactic discs display lopsided perturbations and the fraction of time they experienced significant satellite tidal interactions. In particular, a significant number of simulated disc galaxies (35 per cent of the full sample) did not experience significant interactions during the last 6 Gyr, but nevertheless, have a long-lasting lopsided perturbation over most of that period. This supports our conclusion that direct tidal interaction with satellite galaxies is just one plausible channel for inducing lopsided perturbation, and not the main driving agent. Our results are in agreement with those presented by Bournaud et al. (2005), who show with a sample of 149 observed galaxies that the $m = 1$ amplitude is uncorrelated with the presence of companions.

In addition to direct tidal torques exerted by satellites, galactic discs can respond to the gravitational interaction with a distorted DM halo (Gómez et al. 2015; Laporte et al. 2018a; Garavito-Camargo et al. 2019). One of the first attempts to statistically study asymmetries in the inner regions of dark haloes, and their possible relation to the accretion of external material on to these regions,

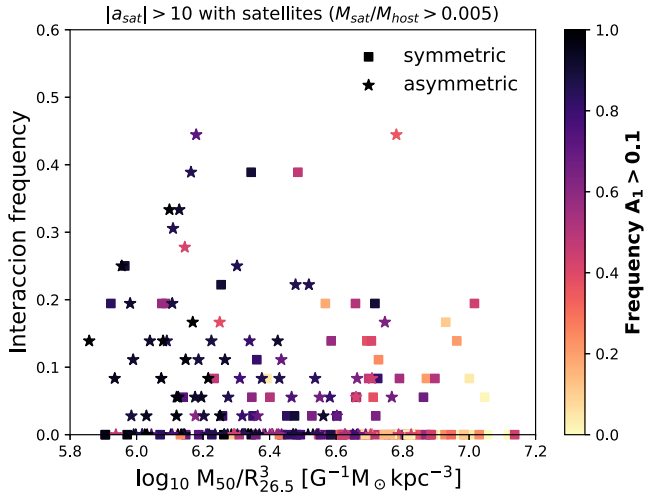


Figure 14. Fraction of time a given host has strongly interacted with satellites of $M_{sat} \geq 10^{9.5} M_\odot$ during the last 6 Gyr of evolution in function of self-gravity proxy. The colour coding indicates the fraction of time galaxies presented a strong lopsided perturbation ($A_1 > 0.1$). The different symbols indicate whether galaxies are symmetric or asymmetric at the present-day. Note that no significant correlation is found between the fraction of time galactic discs display lopsided perturbations and the fraction of time they experienced significant satellite tidal interactions.

Table 3. Number of haloes for each M_{200} range between the two homologous runs; baryonic + DM simulation and only DM.

	TNG50-1	
	Baryon + DM	DM-only
$10^{11} - 5 \times 10^{11} M_\odot$	1251	1352
$5 \times 10^{11} - 10^{12} M_\odot$	190	185
$10^{12} - 5 \times 10^{12} M_\odot$	168	172

was provided by Gao & White (2006, hereafter GW06). Based on the large statistic provided by the Millennium Simulation (Springel et al. 2005), they studied asymmetries in the density distribution of DM haloes, selected with masses ranging from MW mass to cluster mass hosts. They showed that such asymmetries are not uncommon, and that the frequency with which they arise depends on host mass. While 20 per cent of cluster haloes have density centres that are separated from barycentre by more than 20 per cent of the virial radius, only 7 per cent of MW haloes have such large asymmetries.

Following GW06, we examine the distribution of the offsets of central DM haloes extracted from the TNG50-1 simulation and its DM-only simulation counterpart. Our goal is to test whether we recover the results presented in GW06, based purely on DM-only models, and test whether the addition of baryons has an effect on this statistics. Since our work is centred around late-type galaxies, we focus on three sets of models selected by halo mass, M_{200} . The less massive set contains haloes with M_{200} between 10^{11} and $5 \times 10^{11} M_\odot$; the intermediate set between 5×10^{11} and $10^{12} M_\odot$, and the more massive between 10^{12} and $5 \times 10^{12} M_\odot$. In Table 3, we show the results of this selection for each simulation.

For each simulated galaxy, we compute $\Delta r_{\text{DM}}^{R_{200}}$ (see equation 4) at the present-day considering DM particles within R_{200} . In the top panel of Fig. 15, we show the $\Delta r_{\text{DM}}^{R_{200}}$ cumulative distribution function (CDF) for the three halo subsets. The solid and dashed lines show the results obtained from the full hydrodynamical simulation and the DM-only, respectively. To facilitate the comparison between these different haloes, each Δr_{DM} has been normalized by the corresponding R_{200} . Our results based on the DM-only simulations are in good agreement with GW06. We find that more massive haloes tend to have larger asymmetries. Indeed, while ~ 8 per cent of haloes with $10^{12} < M_{200} < 5 \times 10^{12} M_\odot$ show $\Delta r_{\text{DM}}^{R_{200}} > 20$ per cent, for haloes with $10^{11} < M_{200} < 5 \times 10^{11} M_\odot$ only ~ 1.5 per cent show such large asymmetries. Comparison with the results obtained with the full-physics models shows that these trends are not significantly affected by the addition of baryons. The shaded areas highlight the differences between the DM-only and the hydrodynamical simulations. Note that only the larger mass halo subset shows a slightly larger fraction of haloes with $\Delta r_{\text{DM}}^{R_{200}} \gtrsim 0.15$ in the hydrodynamical simulation. However, this difference mainly arises from the low number statistics associated with mass bin.⁵ The similarities between both simulations are better highlighted in the bottom panel of Fig. 15, where we show the difference between both CDFs.

As previously discussed in GW06, these DM halo asymmetries could be related to visible asymmetric phenomena in galaxies, among them lopsidedness. To explore this, we show the Δr_{DM}^l CDF, now considering only galaxies selected by the criteria defined in Section 2.2. For this analysis, we focus on perturbations within the inner DM halo, $3 \times R_{26.5}$ (Fig. 16), since this is the region that can exert significant torque on the embedded discs (e.g. Gómez

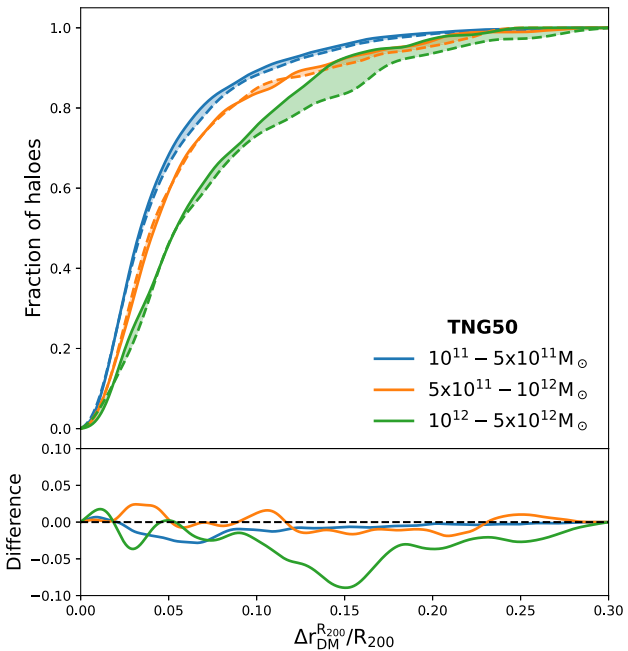


Figure 15. Top panel: Cumulative distribution function of offset between the halo CoM and their density cusp, Δr_{DM} . The colour coded lines show the results obtained from different halo mass ranges. For this calculation, DM particles within each halo's R_{200} are considered. Solid and dashed lines show the results obtained from the full hydrodynamical and the DM-only simulations, respectively. Bottom panel: Differences between CDF obtain from the full hydrodynamical and the DM-only simulations.

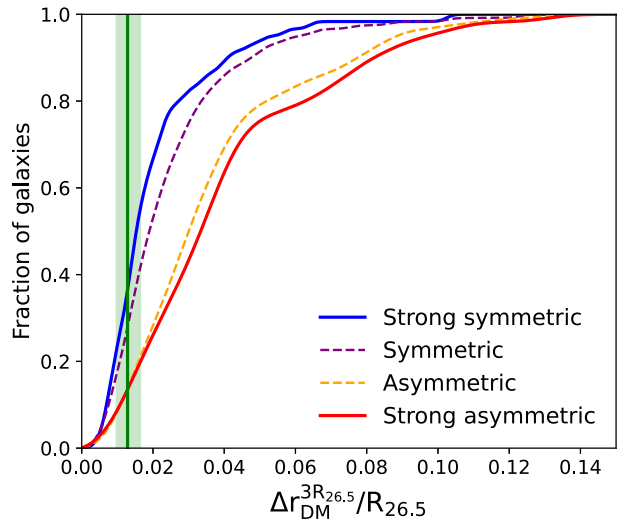


Figure 16. Cumulative distribution function of the offset between the halo CoM and their density cusp, $\Delta r_{\text{DM}}^{3R_{26.5}}$. For this calculation, DM particles within each galaxy ($3 \times R_{26.5}$) are considered. The dashed purple (solid blue) and orange (red) lines show the results obtain from the (strong) symmetric and asymmetric sub-samples, respectively. The vertical green line indicates the median of the distribution obtained after normalizing the gravitational softening, ϵ_{DM} , by the $R_{26.5}$ of each galaxy. The shaded green area encloses the 25th and 75th percentile of the corresponding distribution.

⁵We have confirmed that this difference is due to low number statistics by repeating the analysis on the larger volume simulations TNG100-1.

et al. 2016). We first explore the subset of galaxies that are strongly symmetric and strongly lopsided. The corresponding CDFs are shown in solid red and blue lines, respectively. The vertical green line indicates the mean of the gravitational softening length, ϵ_{DM} (see Table 1), obtained after normalizing ϵ_{DM} by the $R_{26.5}$ of each galaxy. The shaded region covers 25th and 75th percentiles of this distribution. The figure clearly shows that symmetric galaxies tend to have small $\Delta r_{\text{DM}}^{3R_{26.5}}$, indicating very similar spatial location for the DM CoM of the centre of density. Only 5 per cent of the symmetric galaxies show values of $\Delta r_{\text{DM}}^{3R_{26.5}} > 0.05$. The CDF for the asymmetric galaxies shows a different behaviour. It is clear that asymmetric galaxies tend to show significantly large $\Delta r_{\text{DM}}^{3R_{26.5}}$ than their symmetric counterparts. Indeed, ≈ 30 per cent of the disc galaxies show $\Delta r_{\text{DM}}^{3R_{26.5}} > 0.05$. Yet, as discussed in Section 4.5.1, we find a large number of lopsided galaxies show very small $\Delta r_{\text{DM}}^{3R_{26.5}}$, indicating that this is not necessarily the main driver behind their perturbations.

5 CONCLUSIONS AND DISCUSSION

In this paper, we have studied disc galaxies that display a global $m = 1$ non-axisymmetric perturbation in their stellar mass distribution, more commonly known as a lopsided perturbation. We focused the analysis on a sample of MW mass-like galaxies from the fully cosmological hydrodynamical simulation, TNG50 from IllustrisTNG project. Our sample was built selecting central subhaloes with M_{200} within the range $10^{11.5} - 10^{12.5} \text{ M}_\odot$. To consider well-resolved disc-dominated galaxies, we imposed a threshold in the D/T ratio of 0.5, and only selected galaxies with more than 10^4 stellar particles within a subhalo. From this criteria, 240 late-type galaxies with total stellar mass between $10^{9.5}$ and $10^{11.2} \text{ M}_\odot$ were selected. Lopsidedness in the discs were quantified by computing the amplitude of the $m = 1$ Fourier mode of the stellar density distribution, A_1 . Based on this parameter, we classified our galaxies as symmetrical and asymmetrical (i.e. lopsided) cases.

We find that in our simulated galaxy sample the main characteristics of such lopsided perturbations are in good agreement with observations. In lopsided galaxies, the radial profile of the $m = 1$ mode amplitude, $A_1(R)$, increases with radius in the outer disc regions, while in the inner parts it remains flat and close to zero. The radius at which the transition takes place is $\approx 0.5R_{26.5}$, in agreement with previous observational works (e.g. Rix & Zaritsky 1995; Bournaud et al. 2005). Furthermore, lopsided galaxies exhibit a nearly constant or mildly varying radial distribution of phase angles, indicating a slow winding of the phase angle in the outer disc (Saha et al. 2007; Ghosh et al. 2022). Based on this, we computed for each simulated galaxy a characteristic A_1 value, which corresponds to the average of $A_1(R)$ between $0.5R_{26.5} < R < 1.1R_{26.5}$. We find that the distribution of this characteristic A_1 parameter is also in good agreement with observations, that measured in large observational samples the A_1 distribution, considering similar galactic regions (Bournaud et al. 2005; Reichard et al. 2008). To highlight differences between lopsided and symmetrical galaxies, we focus on the analysis on the first and fourth quartiles of the A_1 distribution. We call these subsets strong symmetric and strong asymmetric galaxies, respectively.

When analysing the present-day structural parameters of our sample, we find that lopsided galaxies tend to be more disc dominated than their symmetrical counterparts. This trend suggests that the presence of centrally pressure-supported component plays an important role on setting the lopsidedness strength. This is in agreement with previous works, which found that the fraction of lopsided galaxies

increases with galaxy Hubble type, being late-type galaxies the population with the highest fraction (Rix & Zaritsky 1995; Conselice et al. 2000; Bournaud et al. 2005). Following R08, we also characterized our sample through the following present-day structural parameters: stellar half-mass radius, R_{50}^* , total stellar mass, M^* , central surface density, μ_* , and stellar concentration, C_* . Focusing on the strong subsamples, we find that both lopsided and symmetric galaxies show very similar C_* distributions. We also find that strongly lopsided galaxies tend to have more extended central regions and to be slightly less massive than their symmetrical counterpart. However, the most strong (anti)correlation we find is between μ_* and A_1 . Indeed, the strong sub-samples show very different distributions of μ_* , with lopsided disc systematically showing lower μ_* values. These results are consistent with the observational findings from R08, suggesting that galaxies with lower central density could be more susceptible to different types of interaction and, thus, more prone to the excitation of a lopsided modes. Based on these results, we show that what regulates whether a galaxy develops strong lopsided modes is the self-gravitating nature of the inner galactic regions. Discs with denser inner regions are more gravitationally cohesive and thus, less prone to develop lopsided perturbations in their external regions. Hence, our results hint towards a population of galaxies susceptible to lopsided perturbations, and not to a particular external driving source.

We have explored the time evolution of the main structural parameters that differentiate symmetric and lopsided galaxies, as well as the time evolution of the amplitude of the lopsided modes. We focus on their behaviour during the last 6 Gyr of evolution. We observed that the percentage of galaxies in our sample with $A_1 > 0.1$ are between 60 and 70 during this range of time. Interestingly, we find that, while for symmetric galaxies μ_* remains nearly constant through time, a significant decay of μ_* is observed in lopsided galaxies. The main reason for this is the faster growth of the half-mass radius, R_{50}^* , displayed by lopsided galaxies with respect to their symmetric counterparts. While both galaxies experienced similar growth rates of their M_{50}^* , lopsided galaxies grow faster in size thus reducing their inner self-gravitational cohesion. Following Grand et al. (2016), we analysed whether the halo spin, λ , is behind this faster growth rate of R_{50}^* in lopsided objects. Interestingly, we find that galaxies with higher present-day λ are typically less cohesive and show higher values of A_1 . On the other hand, galaxies with low λ values are dominated by strongly self-gravitating discs and, thus, low A_1 values. Our results highlight an interesting morphology–halo connection for late-type galaxies.

We have also analysed the main agents driving these perturbations. In agreement with previous studies, we have shown that satellite interactions can excite lopsided modes (Weinberg 1995; Zaritsky & Rix 1997; Bournaud et al. 2005). However, we find that up to ~ 35 per cent of the sample galaxy shows significant lopsided perturbations but, during the last 6 Gyr of evolution, did not experience interactions with any satellite of mass ratio $M_{\text{sat}}/M_{\text{host}} > 0.005$. Interestingly those galaxies present low values of μ_* . This supports the conclusion that direct tidal interaction with satellite is a possible channel for inducing lopsided perturbation, but not the main driving agent. Our results are in agreement with those presented by Bournaud et al. (2005), who show with a sample of 149 observed galaxies that the $m = 1$ amplitude is uncorrelated with the presence of companions.

Several studies have shown that galactic discs can also respond to tidal torques exerted by global perturbations of the host DM halo density distribution (Weinberg 1998; Gómez et al. 2016; Laporte et al. 2018a, b; Hunt et al. 2021; Grand et al. 2022). To examine whether this mechanism is an important driving agent of lopsided perturbations in our simulations, we quantified the distribution of

offsets between the CoM DM halo and the density cusp, r_{cusp} , of our haloes, $\Delta r_{\text{DM}}^{\text{R}_{200}}$. Previous studies based on the DM-only Millennium simulations (Gao & White 2006) found that significant distortions in the DM haloes are not uncommon, and that the frequency with which they arise depends on host mass. Our analysis, based on simulations that incorporate a self-consistent treatment for the evolution of baryons, yielded very similar results. While ~ 8 per cent of haloes with $10^{12} < M_{200} < 5 \times 10^{12} \text{ M}_\odot$ show $\Delta r_{\text{DM}}^{\text{R}_{200}} > 20$ per cent, only ~ 1.5 per cent of haloes with $10^{11} < M_{200} < 5 \times 10^{11} \text{ M}_\odot$ show such large asymmetries. Given this result, we studied whether haloes with large offsets typically host lopsided galactic discs. Interestingly, we find that symmetric galaxies tend to have smaller distortions in their inner DM haloes (within $3 \times R_{26.5}$) than their lopsided counterparts. While only 5 per cent of the symmetric galaxies show values of $\Delta r_{\text{DM}}^{\text{R}_{26.5}} > 0.05$, ≈ 30 per cent of the lopsided galaxies do so. This results place torques from DM halo overdensity wake as another important mechanism behind the excitation of lopsided modes in galaxies with low central surface densities. In a follow-up study, we will quantify such torques by decomposing the density and potential distributions using basis function expansions (Cunningham et al. 2020; Garavito-Camargo et al. 2021; Johnson et al. 2023; Lilleengen et al. 2023). Furthermore, we found that lopsided galaxies tend to live in high spin DM haloes. Using the same simulation suite, Grand et al. (2017) showed that the present-day size of a stellar disc is strongly related to the spin of its halo. High spin haloes tend to host extended galaxies with lower central surface densities, thus prone to develop lopsided perturbations. This result, together with the lopsided response of discs to overdensity wakes, indicates a new direction for understanding the halo–galaxy connection in lopsided galaxies.

In this work, we have shown that lopsidedness is a very frequent phenomenon in the history of galaxies. The discs of these galaxies are extended with low central surface densities. Their self-gravity makes them cohesively weak, and therefore easily susceptible to any type of interaction such as tidal torques exerted by distorted DM haloes and minor mergers. Such galaxies tend to reside in high spin and often highly asymmetric DM haloes, revealing a connection between the haloes and lopsided discs.

ACKNOWLEDGEMENTS

SV-L acknowledges financial support from Agencia Nacional de Investigacion y Desarrollo (ANID)/‘Beca de Doctorado Nacional’/21221776. FAG and SV-L acknowledge financial support from CONICYT through the project FONDECYT Regular No. 1211370. FAG and SV-L acknowledge funding from the Max Planck Society through a Partner Group grant. PBT acknowledges partial support from Fondecyt 1200703/2020 (ANID), Nucleus Millennium ERIS ANID NCN2021-017. FAG, PBT, and SV-L acknowledge support from ANID BASAL project FB210003. CFPL acknowledges funding from the European Research Council (ERC) under the European Union’s Horizon 2020 research and innovation programme (grant agreement no. 852839).

DATA AVAILABILITY

The data used in this work are accessible via the IllustrisTNG public data base.⁶

REFERENCES

- Baldwin J. E., Lynden-Bell D., Sancisi R., 1980, *MNRAS*, 193, 313
- Bournaud F., Combes F., Jog C. J., Puerari I., 2005, *A&A*, 438, 507
- Bruzual G., Charlot S., 2003, *MNRAS*, 344, 1000
- Cataldi P., Pedrosa S. E., Tissera P. B., Artale M. C., 2021, *MNRAS*, 501, 5679
- Chabrier G., 2003, *PASP*, 115, 763
- Conselice C. J., Bershady M. A., Jangren A., 2000, *ApJ*, 529, 886
- Cunningham E. C. et al., 2020, *ApJ*, 898, 4
- Eskridge P. B. et al., 2002, *ApJS*, 143, 73
- Gao L., White S. D. M., 2006, *MNRAS*, 373, 65 (GW06)
- Garavito-Camargo N., Besla G., Laporte C. F. P., Johnston K. V., Gómez F. A., Watkins L. L., 2019, *ApJ*, 884, 51
- Garavito-Camargo N., Besla G., Laporte C. F. P., Price-Whelan A. M., Cunningham E. C., Johnston K. V., Weinberg M., Gómez F. A., 2021, *ApJ*, 919, 109
- Genel S. et al., 2014, *MNRAS*, 445, 175
- Genel S., Fall S. M., Hernquist L., Vogelsberger M., Snyder G. F., Rodriguez-Gomez V., Sijacki D., Springel V., 2015, *ApJ*, 804, L40
- Ghosh S., Saha K., Jog C. J., Combes F., Di Matteo P., 2022, *MNRAS*, 511, 5878
- Gómez F. A., Besla G., Carpintero D. D., Villalobos Á., O’Shea B. W., Bell E. F., 2015, *ApJ*, 802, 128
- Gómez F. A., White S. D. M., Marinacci F., Slater C. T., Grand R. J. J., Springel V., Pakmor R., 2016, *MNRAS*, 456, 2779
- Gómez F. A., White S. D. M., Grand R. J. J., Marinacci F., Springel V., Pakmor R., 2017, *MNRAS*, 465, 3446
- Grand R. J. J., Springel V., Gómez F. A., Marinacci F., Pakmor R., Campbell D. J. R., Jenkins A., 2016, *MNRAS*, 459, 199
- Grand R. J. J. et al., 2017, *MNRAS*, 467, 179
- Grand R. J. J., Pakmor R., Fragkoudi F., Gómez F. A., Trick W., Simpson C. M., van de Voort F., Bieri R., 2022, preprint ([arXiv:2211.08437](https://arxiv.org/abs/2211.08437))
- Haynes M. P., Hogg D. E., Maddalena R. J., Roberts M. S., van Zee L., 1998, *AJ*, 115, 62
- Hunt J. A. S., Steleia I. A., Johnston K. V., Gandhi S. S., Laporte C. F. P., Bédorf J., 2021, *MNRAS*, 508, 1459
- Jog C. J., 1997, *ApJ*, 488, 642
- Jog C. J., 1999, *ApJ*, 522, 661
- Jog C. J., 2000, *ApJ*, 542, 216
- Jog C. J., Combes F., 2009, *Phys. Rep.*, 471, 75
- Johnson A. C., Petersen M. S., Johnston K. V., Weinberg M. D., 2023, *MNRAS*, 521, 1757
- Khademi M., Yang Y., Hammer F., Nasiri S., 2021, *A&A*, 654, A7
- Kornreich D. A., Lovelace R. V. E., Haynes M. P., 2002, *ApJ*, 580, 705
- Laporte C. F. P., Gómez F. A., Besla G., Johnston K. V., Garavito-Camargo N., 2018a, *MNRAS*, 473, 1218
- Laporte C. F. P., Johnston K. V., Gómez F. A., Garavito-Camargo N., Besla G., 2018b, *MNRAS*, 481, 286
- Levine S. E., Sparke L. S., 1998, *ApJ*, 496, L13
- Li Z.-Y., Ho L. C., Barth A. J., Peng C. Y., 2011, *ApJS*, 197, 22
- Lilleengen S. et al., 2023, *MNRAS*, 518, 774
- Lokas E. L., 2022, *A&A*, 662, A53
- Marinacci F. et al., 2018, *MNRAS*, 480, 5113
- Naiman J. P. et al., 2018, *MNRAS*, 477, 1206
- Nelson D. et al., 2015, *Astron. Comput.*, 13, 12
- Nelson D. et al., 2018, *MNRAS*, 475, 624
- Nelson D. et al., 2019a, *Comput. Astrophys. Cosmol.*, 6, 2
- Nelson D. et al., 2019b, *MNRAS*, 490, 3234
- Noordermeer E., Sparke L. S., Levine S. E., 2001, *MNRAS*, 328, 1064
- Pillepich A. et al., 2018, *MNRAS*, 473, 4077
- Pillepich A. et al., 2019, *MNRAS*, 490, 3196
- Planck Collaboration XIII, 2016, *A&A*, 594, A13
- Quillen A. C., Dougherty J., Bagley M. B., Minchev I., Comparetta J., 2011, *MNRAS*, 417, 762
- Reichard T. A., Heckman T. M., Rudnick G., Brinchmann J., Kauffmann G., 2008, *ApJ*, 677, 186 (R08)
- Richter O. G., Sancisi R., 1994, *A&A*, 290, L9

⁶<https://www.tng-project.org/data>

- Rix H.-W., Zaritsky D., 1995, *ApJ*, 447, 82
 Rudnick G., Rix H.-W., 1998, *AJ*, 116, 1163
 Saha K., Combes F., Jog C. J., 2007, *MNRAS*, 382, 419
 Schoenmakers R. H. M., Franx M., de Zeeuw P. T., 1997, *MNRAS*, 292, 349
 Springel V., 2010, *MNRAS*, 401, 791
 Springel V., White S. D. M., Tormen G., Kauffmann G., 2001, *MNRAS*, 328, 726
 Springel V. et al., 2005, *Nature*, 435, 629
 Springel V. et al., 2018, *MNRAS*, 475, 676
 Swaters R. A., Schoenmakers R. H. M., Sancisi R., van Albada T. S., 1999, *MNRAS*, 304, 330
 Tissera P. B., Lambas D. G., Abadi M. G., 1997, *MNRAS*, 286, 384
 Tissera P. B., White S. D. M., Scappapietra C., 2012, *MNRAS*, 420, 255
 van Eymeren J., Jütte E., Jog C. J., Stein Y., Dettmar R. J., 2011, *A&A*, 530, A30
 Vogelsberger M. et al., 2014a, *MNRAS*, 444, 1518
 Vogelsberger M. et al., 2014b, *Nature*, 509, 177
 Walker I. R., Mihos J. C., Hernquist L., 1996, *ApJ*, 460, 121
 Weinberg M. D., 1994, *ApJ*, 421, 481
 Weinberg M. D., 1995, *ApJ*, 455, L31
 Weinberg M. D., 1998, *MNRAS*, 299, 499
 Weinberger R. et al., 2017, *MNRAS*, 465, 3291
 Zaritsky D., Rix H.-W., 1997, *ApJ*, 477, 118
 Zaritsky D. et al., 2013, *ApJ*, 772, 135

This paper has been typeset from a TeX/LaTeX file prepared by the author.